Design of Inflammation-modulatory Biomaterials for Soft Tissue Regeneration

YOSUKE MIZUNO

February 2021

Design of Inflammation-modulatory Biomaterials for Soft Tissue Regeneration

YOSUKE MIZUNO
Doctoral Program in Materials Science and Engineering

Submitted to the Graduate School of

Pure and Applied Sciences

in Partial Fulfillment of the Requirements

for the Degree of Doctor of Philosophy in Engineering

at the

University of Tsukuba

Abstract

Pro-inflammatory and anti-inflammatory responses during wound healing processes involves angiogenesis and inflammation resolution to promote tissue regeneration. Angiogenesis plays important role in not only wound healing but regenerative medicine. In addition to the need for anti-inflammation to promote wound healing, the treatment of burns and rheumatoid arthritis requires the elimination of excessive inflammation through anti-inflammatory treatment. Angiogenesis treatment is mainly induced by the delivery of exogenous angiogenic growth factors; however, those low stability under physiological conditions limits its range of applications. To overcome those challenges, saturated fatty acids, which comprise lipopolysaccharide and induce angiogenesis, were employed to develop the growth factor-free angiogenic materials in the form of self-assembled hydrogels, microparticles and fiber sheets. Those materials induced angiogenic responses by stimulation of the endogenous growth factor secretion. Burn injury and rheumatoid arthritis require the elimination of excess inflammatory responses to remove pain and promote regeneration. Unsaturated fatty acids were employed to develop an anti-inflammatory/antioxidant hydrogel. The hydrogel exerted not only anti-inflammatory effects on activated cells but negligible cytotoxicity on the mitochondrial activity compared to the severe toxicity caused by non-conjugated fatty acids. Those inflammation-modulatory biomaterials have potential applications for soft tissue regenerations by means of stimulation or resolution of inflammatory responses.

Table of Contents

List of Tables

CHAPTER 2

CHAPTER 3

CHAPTER 4

List of Figures

CHAPTER 1

CHAPTER 2

CHAPTER 3

CHAPTER 4

CHAPTER 5

Acknowledgements

First and foremost, I must express my greatest gratitude to Dr. Tetsushi Taguchi. He has always supported me for my professional and personal growth throughout my doctoral work. Without his guidance and support, this research would not have progressed this far. He always gave me advice whenever I ran into a trouble spot or had a question about my research or writing. Moreover, he taught me not only the way of proceeding research but presentation skills and writing a paper and proposal. His kind guidance and support lead me to publish multiple papers and achieve JSPS DC1. I could not have asked for a better mentor, teacher and motivator.

I would like to thank Dr. Akihiro Nishiguchi for his very informative advices. His kind guidance of cell experiments and evaluation techniques was greatly helpful to expand the evaluations and discussions of biochemical responses to our materials. Besides, he taught me the importance of grasping data from a wide range of perspectives. His advice changed the viewpoint of experimental theme and lead to publish a paper.

I would like to express my gratitude to my thesis committee: Dr. Chen Guoping, Dr. Kohsaku Kawakami and Dr. Seiya Tsujimura. Their invaluable feedback and genuine interest to my work is greatly appreciated. Their multilateral feedback and the critical questions drove my PhD to a successful completion. I also want to thank researchers, engineers and advisors in NIMS, Mr. Kenichi Omori, Dr. Mitsuhiro Ebara, Dr. Masanobu Naito, Dr. Naoki Kawazoe, Dr. Sachiko Hiromoto, Dr. Takashi Minowa, Dr. Xianglan Li, Dr. Shinya Hattori, Dr. Yoko Shirai and Dr. Koichiro Uto, for providing positive and diverse perspectives as well as technical assistances.

This thesis would not have succeeded without the colleagues and staffs of polymeric biomaterials group over years. First, to Dr. Keiko Yoshizawa, Dr. Ryo Mizuta, Dr. Xi Chen, Mr. Hiroaki Ichimaru and Mr. Shima Ito, thank you for your friendship and assistance in many ways. I would like to appreciate staffs of our group including Mrs. Mayumi Katano, Mrs. Takumi Iwano, Mrs. S. Watanabe, Mrs. Yukari Kurihara, Mrs. Mieko Ishikawa, Mrs. Yuka Nakagawa, Mrs. Chihiro Mizuno, Mrs. Saori Matuura, Mrs. Yuki Naito and Ms. Hiromi Hirade for their technical and administrative supports.

Finally, I must be grateful to my family for the last 6 years, but long before and for long after. Their financial and emotional support have encouraged me and enabled me to live in comfort. I couldn’t imagine completing my Ph.D without them.

CHAPTER 1: GENERAL INTRODUCTION

1.1. Inflammation and Wound Healing

Inflammation plays an important role in the part of the wound healing process. Pro-inflammatory response was immediately initiated upon an injury or a bacterial infection followed by production of damage associated molecular patterns and various kind of pro-inflammatory cytokines [1]. In response to those signals, immune cells are stimulated to further secrete pro-inflammatory cytokines including tumor necrosis factor (TNF)-α, interleukin-1 (IL-1), IL-6, and IL-12, which promote the fibroblast proliferation and the synthesis of collagen and collagenase **(Figure 1-1)** [2–4]. Upon the inflammatory responses, resting macrophages are activated into "M1" (pro-inflammatory) and "M2" (anti-inflammatory/reparative) macrophages [2,5]. M1 macrophages secret pro-inflammatory cytokines, whereas, M2 macrophages produce growth factors such as platelet-derived growth factor, transforming growth factor (TGF)-β, and vascular endothelial growth factor (VEGF), which promote the formation of granulation tissue [6]. Although the gene expression of M1 and M2 macrophages are initially increased upon the injury, M2 macrophages predominantly exits with a delay to ameliorate the inflammatory responses to complete the tissue remodeling **(Figure 1-1)** [7,8]. M2 macrophages secrete anti-inflammatory mediators such as IL-10, TGF-β1, and IL-1 receptor antagonist (IL-1RA) to downregulate the expression of pro-inflammatory cytokines (**Figure 1-1**) [1,2].

Upon the formation of granulation tissue at the wound site, microvascular network is formed throughout the tissue by various growth factors such as VEGF and basic fibroblast growth factor (bFGF), and

platelet-derived growth factor (PDGF) [4,9]. The formed vascular network provides oxygen and nutrients supply to regenerating cells, promoting cellular metabolism, proliferation, and collagen synthesis to complete wound healing [10,11]. The contaminated gram-negative bacteria in wound site promote faster wound closure compared with non-contaminated wound by inducing inflammatory response and growth factor secretion followed by angiogenesis [12].

Angiogenesis itself is not only a process of wound healing but contribute to supply oxygen and nutrients for implanted cells in terms of regenerative medicine. On the other hand, the resolution of activated inflammatory response upon an acute injury by anti-inflammatory mediators promotes fast wound healing. In present study, we focused on the angiogenesis induced by pro-inflammatory response and fast wound healing by anti-inflammatory response for the biomaterial-based soft tissue regeneration.

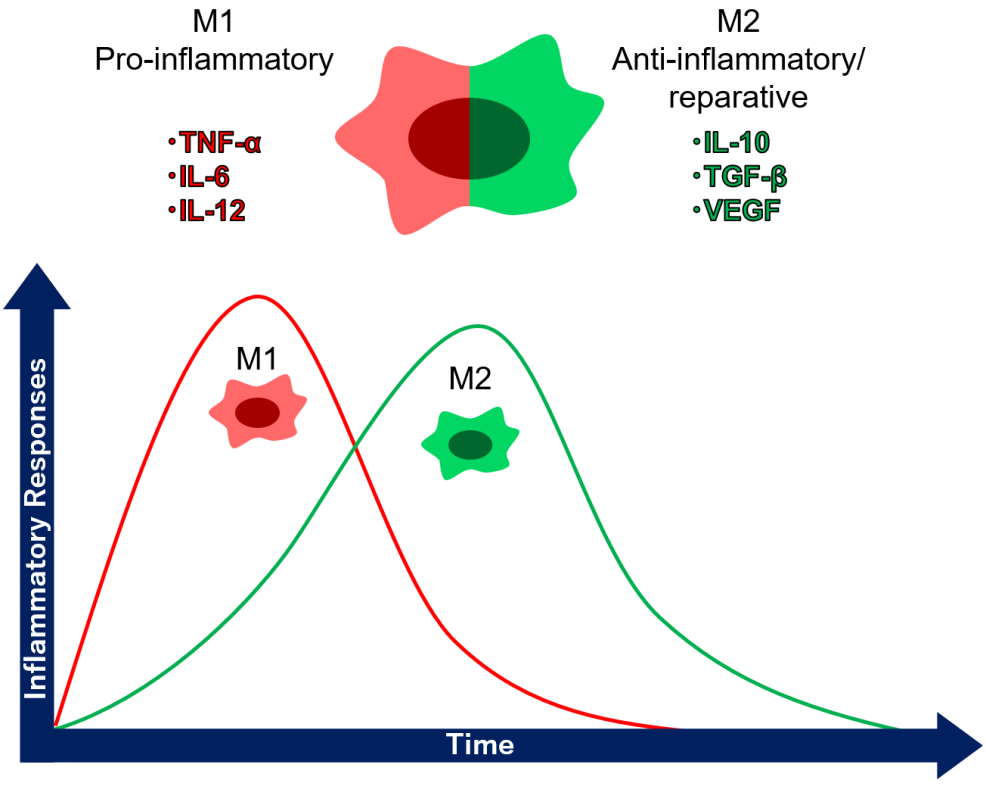

Figure 1-1. Time course of M1/M2 phenotypes during wound healing. (Inspired by ref. 8)
Macrophages polarize into M1/M2 phenotypes upon injury.

1.2. Biomaterials for Angiogenesis

1.2.1. Cell transplantation and Angiogenesis

Regenerative medicine is one of the fruits of advanced biomedical, biological, and clinical progressions to regenerate damaged or dysfunctional tissues. Clinical technique of regenerative medicine is mainly based on the transplantation of not only functional allogenic cells but autologous stem cells, which differentiate into various type of cells or tissues. A number of animal experiments and clinical trials of cellular transplantation have been reported so far.

Pancreatic islet cells are transplanted from the pancreas of a deceased or living donor into patients with type I diabetes [13–15]. The implanted islet cells serve as a substitute of dysfunctional pancreas to secrete insulin in response to the increase in glucose [15]. Myocardial infarction (MI), which eventually leads to heart failure, is another disease that cell transplantation is potentially effective to treat [16]. Stem cells such as bone-marrow-derived stem cells [17–19], embryonic stem cells [20], and endogenous cardiac stem cells [21,22] are mainly employed for implantation in the infarcted heart [16]. Those cells differentiate into not only cardiomyocytes but endothelial cells and smooth muscle cells after implantation in the ischemic region of heart to improve the function of heart [16]. However, those experiments have only achieved moderate success due to the low retention

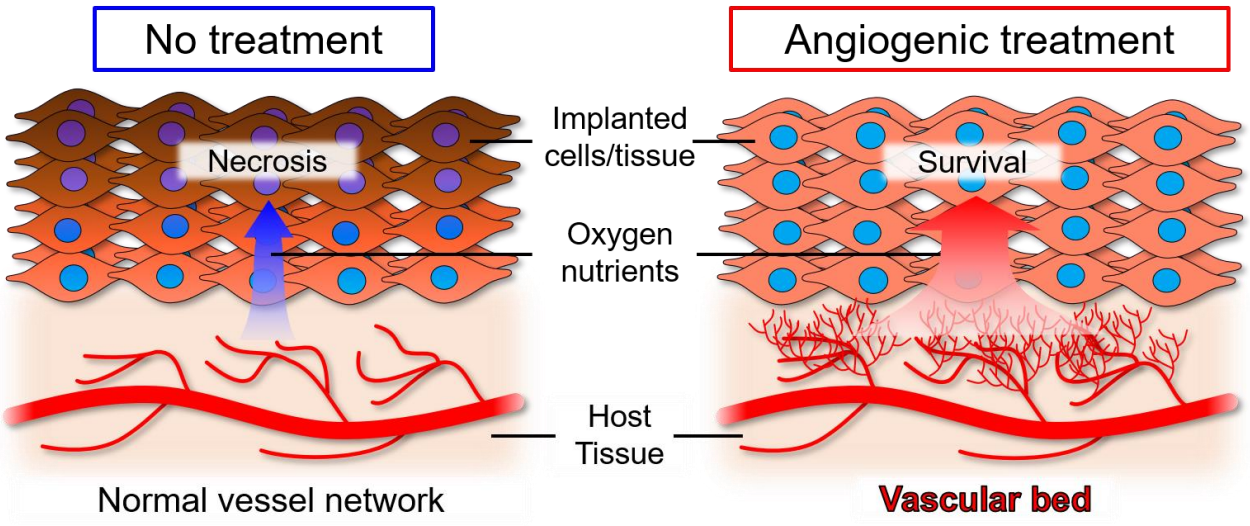

Figure 1-2. Angiogenic treatments for improved implanted cell/tissue survival.

and viability of transplanted cells [23–28].

To address those problems, a vascular bed is generated at the transplant site prior to cell transplantation (**Figure 1-2**) [29–33]. The generated vascular bed supply oxygen and nutrients from host body to implanted cells to improve survival, proliferation, and differentiation. Angiogenesis, the formation of new blood vessels, is mainly induced by the delivery of various growth factors such as VEGF and bFGF [34]. VEGF and bFGF binds to their receptor on endothelial cells to promote proliferation, cell adhesion, lumen formation, and pericyte recruitment [35–38]. Moreover, bFGF stimulates not only endothelial cells but smooth muscle cells, stromal cells, and pericytes to upregulate the expression of growth factors including VEGF, hepatocyte growth factor, and PDGF [39–42]. From a perspective of biomaterials science, a number of materials incorporated with various growth factors have been reported to induce angiogenesis and improve survival of transplanted cells. The poly(lactide-co-glycolide) (PLG) microsphere incorporated with VEGF and hepatocytes demonstrated over a 2-week angiogenesis and significantly greater survival rate in mice subcutaneous [43]. The poly(vinyl alcohol) hydrogel loaded with bFGF induced a vascular bed in diabetic rat subcutaneous followed by transplantation of islet, resulting in improved survival rate of transplanted cells and stabilized blood glucose level [44].

1.2.2. Treatment of Ischemia

Ischemia, a vascular decrease that involves a reduction in local blood flow, is a major complication of MI, stroke, and peripheral artery disease. Decreased blood flow limits the supply of oxygen and nutrients to the surrounding tissues, resulting in necrosis and severe dysfunction. A number of angiogenic biomaterials have been reported as a treatment for ischemia. A collagen hydrogel modified with matrix metalloproteinase cleavable peptides and bFGF degraded in response to MMP upregulation after MI and induced angiogenesis and recovery of heart function of MI rat with ameliorating adverse remodeling [45]. A dual-function angiogenic

biomaterial composed of heparin nanoparticle conjugated with VEGF and hyaluronic acid (HA) hydrogel promoted not only angiogenesis but axonal growth along the neovascular in stoke cavity of mice [46]. Peripheral arterial disease (PAD) caused by diabetes, smoking, and hypercholesterolemia can lead to decreased blood flow to peripheral blood vessels such as hands and feet [47]. Critical limb ischemia (CLI), the most severe form of PAD, involves tissue necrosis, ulcers, and gangrene, and may result in limb amputation [48,49]. Sustained release of bFGF from gelatin microsphere enhanced recovery of blood flow and healing of ulcers of CLI patients [50]. Angiogenesis is also induced by angiogenic gene delivery [34]. The delivery of plasmid DNA encoding VEGF induced site specific transfection of the VEGF gene and formation of collateral vessels in the ischemic leg of patient [51].

1.2.3. Challenges of Angiogenic Materials

Various angiogenic biomaterials, with and without cells, listed above demonstrated angiogenesis for cell transplantation and treatment of ischemic diseases. However, loaded exogenous growth factors have difficulties in stability under physiological conditions, which limits practical applications [52]. bFGF lose its activity after 24 h of incubation at 37 °C [53]. Moreover, half-life of VEGF and bFGF is only 50 and 9.6 min under physiological condition [54,55]. Those adverse effects are attributed to the aggregation of those growth factors, which considered to inhibit the binding to those receptors [53]. Regarding the angiogenic gene delivery, viral vectors, which deliver angiogenic genes to target tissue, have challenges such as strong immune response and insertion mutation [56]. Recent studies have reported various angiogenic biomaterials without growth factors. Feng et al. reported that konjac glucomannan/ heparin hydrogel stimulate macrophage to secret endogenous growth factors and entrap the secreted growth factors to induce angiogenesis [57]. Chen et al. demonstrated that hydroxyapatite bioceramics with nano/micro hierarchical structure promoted macrophage polarization,

angiogenesis and osteogenic differentiation [58]. Moreover, Hong et al. reported that an imidazole-poly(organophosphazenes) hydrogel promoted the remodeling of damaged spinal cord of mice [59]. Imidazole group in the hydrogel binds to histamine receptors of macrophages to induce macrophage polarization and MMP secretions [59]. Those immune activating materials offers another potential strategy of therapeutic angiogenesis for clinical applications.

1.3. Anti-inflammatory Biomaterials

1.3.1. Wound Treatment after Burn Injury

Although inflammatory responses upon the injury is necessary process to complete wound healing as discussed above, excess inflammatory response leads to delayed healing and sustained pain [60–62]. Burn injury, which is mainly caused by heat, involves tissue destruction due to the protein denaturation and cell death [63,64]. The severity of burn depends on its depth; first, second and third [63]. First degree burns are characterized by only epidermal damage and cause limited degree and duration of pain. Second degree burns reach intermediate depth of dermis. Although only superficial burn of dermis does not require a surgery, deeper burn with destruction of pain receptors and nerves require excision of damaged tissues (debridement). Third degree burns are characterized by damage of full thickness of dermis, which is typically no pain due to the complete destruction of the nerves. Third degree also require debridement of damaged tissue. Deeper burn injury involves not only production of inflammatory cytokines but generation of reactive oxygen species (ROS), which have specific role in normal physiological conditions [65,66]. O_2 is reduced to superoxide anion ($O_2^{\bullet -}$) upon burn injuries followed by production of ROS families including $^{\bullet}OH$, $^1O_2$, and H_2O_2 [66]. ROS directly cause damage to cellular protein and lipid membrane, resulting in cell death [66,67]. Those ROS induce prolonged damage to the burn injury sites and often provoke secondary damage to surrounding or distant tissues [65,68,69].

To address those problems, anti-inflammatory biomaterials have been reported so far. Zheng et al. demonstrated a gelatin hydrogel loaded with resveratrol and histatin-1 enhanced burn wound healing by inhibiting expression of pro-inflammatory cytokines and promoting expression of TGF-β [70]. Friedrich et al. reported that a HA modified with an anti-TNF-α antibody alleviated the inflammatory response and promoted tissue regeneration of burn site of rat [71]. However, those loaded drugs or peptides in biomaterials tend to diffuse rapidly and do not provide sufficient anti-inflammatory effects [72]. Moreover, modification of bioactive peptide or antibodies have difficulties in stability under physiological environments due to methionine oxidations [73–76].

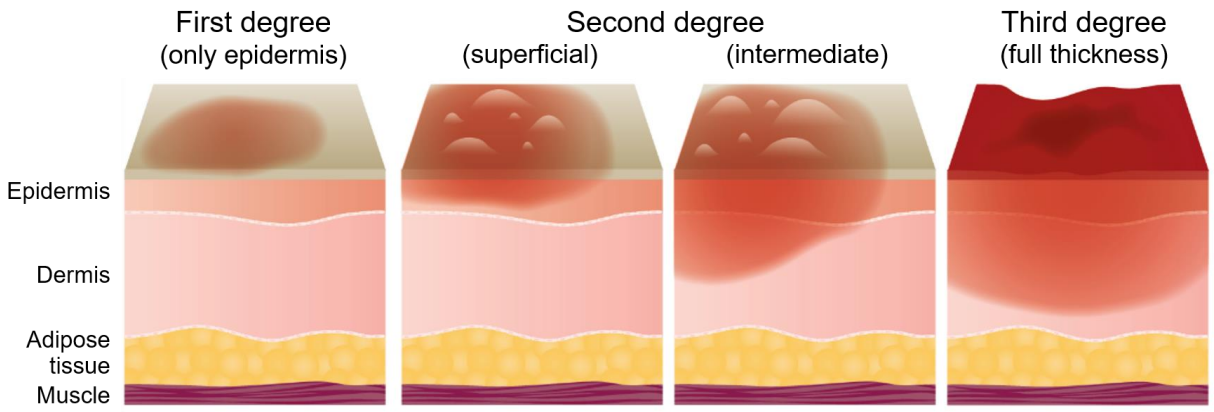

Figure 1-3. Severity of burn injury. (Adapted from ref. 63)

1.3.2. Biomaterials for Rheumatoid Arthritis Treatment

Rheumatoid arthritis (RA) is a systemic autoimmune disease, which involves destruction of synovial joints, joint swelling and joint stiffness [77,78]. Those symptoms are associated with overexpression of various pro-inflammatory cytokines such as TNF-α, IL-1, and IL-6 in joints; IL-6, in particular, plays important role in autoimmune diseases including RA [79–81]. Moreover, synovial fluid, a viscous protective barrier between cartilages, are damaged by inflammatory responses upon RA, resulting in loss of protection from mechanical friction and shock [82,83]. A variety of drugs including non-steroidal anti-inflammatory drugs (NSAID), disease-

modifying antirheumatic drugs and glucocorticoids have been used to treat RA [84–86]. In addition to alleviation of inflammatory responses in inflamed joints, a mechanical support for damaged synovium is also required to alleviate pain and stiffness. A various kind of biomaterials based on HA, a main component of synovial fluid, has demonstrated mechanical support and anti-inflammatory effects for RA treatments [87–89]. On the other hand, collagen and gelatin, a main components of cartilage, is another choice of base materials for treatment of RA [90–92].

1.4. Thesis Overview

The aim of this study is to develop biomaterials for tissue regenerations from different perspectives (**Figure 1-4**). This thesis can be divided into two main themes: the angiogenic materials (Chapter 2-4) and the anti-inflammatory material (Chapter 5).

Chapter 2 provides the synthesis of saturated fatty acid-modified gelatin and the evaluation of angiogenic properties of them. Previous studies reported that a lauric acid (C12), which comprises lipid A of gram-negative bacteria, induced endogenous secretion of VEGF and angiogenesis. Therefore, it was hypothesized that the C12 modified gelatin-based biomaterials exert angiogenic properties with biocompatibility and biodegradability. The angiogenic properties of C12-ApGltn was evaluated by *in vitro* cell experiments and *in vivo* animal experiments.

Chapter 3 describes the sustained angiogenic responses by C12-ApGltn based microparticle (C12-MP). Physicochemical properties of C12-MP including rheological properties, surface contact angle and degradation rate was evaluated. The angiogenic properties of C12-MP was assessed by animal experiments using laser doppler perfusion imaging and histological observations.

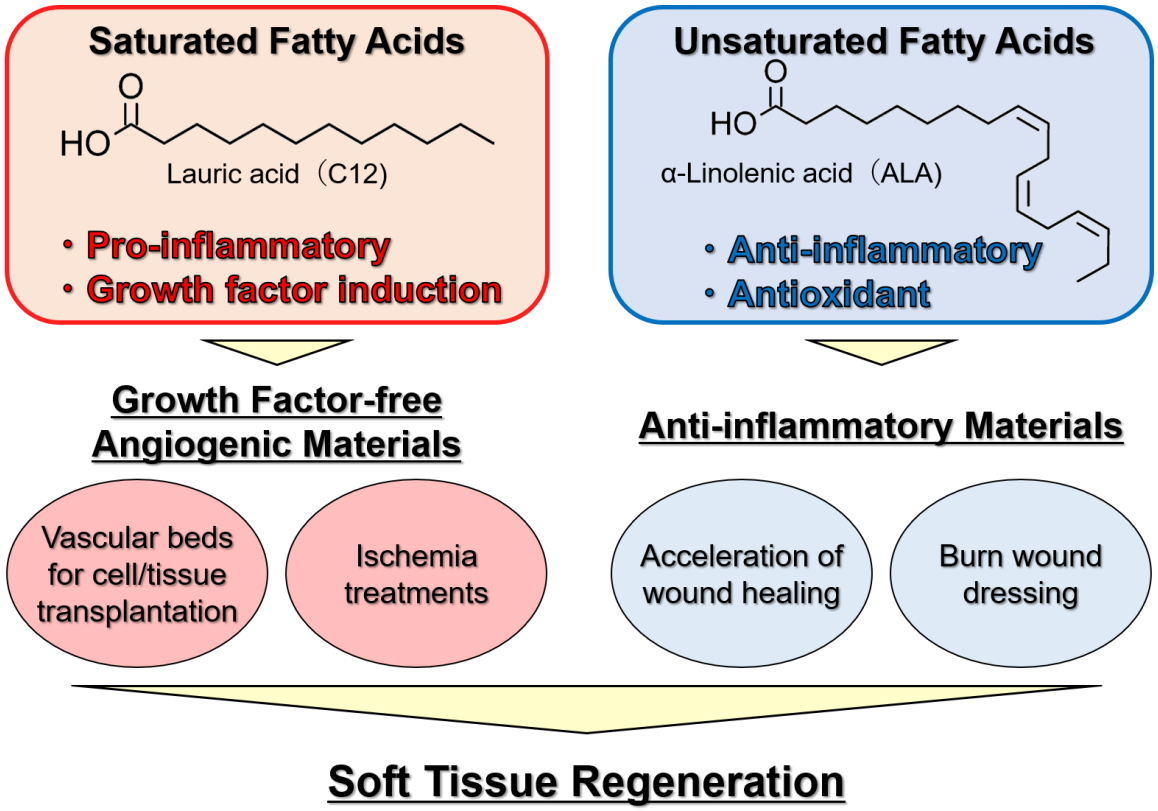

Figure 1-4. Objective and overview of this thesis.

Chapter 4 focuses on C16-ApGltn, in which ApGltn was modified with another functional group, hexadecyl group to achieve growth factor-free angiogenesis. C16-ApGltn was made into electrospun fiber sheets followed by thermal crosslinking (C16-FS) and was evaluated *in vivo* angiogenic responses.

Chapter 5 provides the anti-inflammatory biomaterial based on gelatin substituted with α-linolenic acid (ALA), an unsaturated fatty acid. ALA modified gelatin (ALA-ApGltn) was crosslinked with 4S-PEG crosslinker to form *in situ* hydrogel. The antioxidant property of ALA-ApGltn and ALA-hydrogel were evaluated by quantification of pro-inflammatory cytokines from activated macrophages.

CHAPTER 2: Effect of Alkyl Chain Length on In Vitro/Vivo Inflammatory Responses

2.1 Introduction

Angiogenesis supplies oxygen and nutrients from the host body to transplanted cells and tissues and thereby promotes their survival. Poly(lactic-co-glycolic acid) nanoparticles with a poly(vinyl alcohol) fiber mat incorporating and locally releasing vascular endothelial growth factor (VEGF) was shown to stimulate angiogenesis and enhance the viability of cardiomyocyte sheets [93], while VEGF-loaded collagen sponge crosslinked by glutaraldehyde showed sustained release of VEGF in vivo with the progressive degradation of the sponge [94]. Additionally, freeze-dried agarose containing heparin and basic fibroblast growth factor (bFGF) promoted subcutaneous pre-vascularization for subsequent islet transplantation in diabetic mice, resulting in the restoration of blood glucose level [95]. Peattie *et al*. reported a hyaluronic acid hydrogel crosslinked with poly(ethylene glycol) incorporated with VEGF and keratinocyte growth factor (KGF) [96]. This hydrogel induced microvascular formation around the implant site by the released VEGF and KGF. Although VEGF and bFGF can effectively induce angiogenesis in vivo, their use is limited by a lack of stability under physiological conditions [52]: the half-life of VEGF is about 50 min, and only 0.9% of injected bFGF was detected in ischemic heart 24 h after intracoronary administration [54,55]. To overcome these problems, we have investigated the possibility of stimulating endogenous VEGF secretion in the host by inducing weak

inflammation from biomaterials without additional growth factors. We previously reported that a porous sponge based on hydrophobically modified gelatin (hm-Gltn) showed angiogenic properties in the absence of growth factors in vivo [97], although the underlying mechanisms has yet to be elucidated.

To design an angiogenic hydrogel based on hm-Gltn, we focused on lipopolysaccharide (LPS), a major component of the outer membrane of Gram-negative bacteria that induces an inflammatory response in various cell types [98–100]. LPS also promotes VEGF secretion by inflammatory cells via Toll-like receptor (TLR)4-related pathways, including myeloid differentiation primary response protein (MyD)88 and nuclear factor (NF)-κB [101,102]. Lipid A, a component of LPS that contributes to inflammation, comprises disaccharides of glucosamine units acylated with saturated fatty acids (SFAs). SFAs, such as capric acid (C10), lauric acid (C12) and palmitic acid (C16), behave like lipopolysaccharide (LPS), which is a component of the outer membrane of gram-negative bacteria [98,99,103]. SFAs induce toll-like receptor 4 (TLR4)-mediated inflammation and enhance the secretion of proinflammatory cytokines such as tumor necrosis factor (TNF)-α [104–109].In Pseudomonas aeruginosa, the glucosamine units are acylated with capric acid (C10) and lauric acid (C12) (**Figure 2-1A**) [98]. To investigate the mechanisms of SFA-mediated inflammation, inflammatory cells such as RAW264 mouse macrophage-like cells and THP-1 human monocytic leukemia cells were cultured with lauric acid; this caused the secretion of tumor necrosis factor α and activation of NF-κB, which function upstream of VEGF [104,105,107,108].

In the present study, we developed an angiogenic hydrogel using lauric acid (C12) that induces inflammation and VEGF without requiring any additional growth factors. As a base material we used Alaska pollock-derived gelatin (ApGltn), which is biodegradable, does not cause severe inflammation, and is highly fluid at room temperature owing to a lower imino acid content [110–112]. We introduced a dodecyl group into the

ApGltn molecule to obtain C12-ApGltn and evaluated its viscoelastic properties, degradation rate, and cell response in vitro and angiogenic properties in vivo.

2.2 **Experimental**

2.2.1. Materials

ApGltn (molecular weight = 33,000) was donated by Nitta Gelatin (Osaka, Japan). Ethanol, 2-aminoethanol, 2, 4, 6-trinitrobenzensulfonic acid (TNBS), dimethyl sulfoxide (DMSO), triethylamine, and 10% formalin neutral buffer solution were purchased from Wako Pure Chemical Industries (Osaka, Japan). Hexanal, dodecanal, and octadecanal were from Tokyo Chemical Industry Co. (Tokyo, Japan). 2-Picoline borane (2-picBH3) was from Junsei Chemical Co. (Tokyo, Japan). Collagenase, water-soluble tetrazolium (WST)-8 reagent (Cell Count Reagent SF), and Dulbecco's phosphate-buffered saline (PBS) were from Nacalai Tesque (Kyoto, Japan). RAW264 (RCB0535) was provided by the RIKEN BRC through the National Bio-Resource Project of the MEXT/AMED, Japan.

2.2.2. Synthesis and Characterization of hm-ApGltn

The number of amino groups in ApGltn was initially quantified using TNBS as previously reported [112–115]. Briefly, ApGltn was dissolved in 50% DMSO/H2O solution at 0.5 w/v%, and 100 μL were dispensed in each well of a 48-well plate. TNBS and triethylamine separately dissolved in DMSO/H2O at 1% were added to each well followed by shaking for 1 min. After 2 h of incubation at 37°C, the absorbance at 335 nm was measured with a microplate reader (Spark 10M; Tecan, Männedorf, Switzerland). 2-Aminoethanol was used instead of ApGltn to generate a calibration curve.

ApGltn was modified with hydrophobic groups by reductive amination as previously described (**Figure 2-1B**) [112,116,117]. Briefly, ApGltn was dissolved in 30% EtOH/H2O at 20 w/v%. Hexanal, dodecanal, and octadecanal (1.0, 1.5, and 1.0 eq on ApGltn amino groups, respectively) dissolved in ethanol were then added; after 18 h, the reaction solution was added dropwise to 10 times the volume of cold ethanol with vigorous stirring to precipitate ApGltn, followed by vacuum filtration through a glass filter. The precipitate was washed three times with EtOH to remove unreacted reagents and 2-picBH3, followed by vacuum drying at room temperature (25°C). Modified ApGltn was obtained as a white powder and weighed to calculate yield. Non-modified ApGltn (Org-ApGltn) was also synthesized using the same protocol but without including fatty aldehyde and 2-picBH3. The modification ratio of hydrophobic groups on ApGltn was quantified with the TNBS method by comparing the absorbance at 335 nm with that of Org-ApGltn. Modification of hydrophobic groups was confirmed by Fourier transform infrared spectroscopy (FT-IR) (ALPHA II; Bruker Corp., Billerica, MA, USA) and ^{1}H nuclear magnetic resonance (^{1}H-NMR) (JNM-AL300; JEOL, Tokyo, Japan). To observe microstructures of Org-, C6-, C12-, and C18-ApGltn, their aqueous solutions at 20 w/v% were lyophilized and observed with scanning electron microscope (SEM) (S-4800 typeT0; HITACHI High-Technologies, Tokyo, Japan).

2.2.3. Rheological Properties

To assess the viscoelastic properties of the hydrogel, gelatin was dissolved in PBS at 20 w/v%. The gelatin solution was placed on the stage of an MCR 301 rheometer (Anton Paar GmbH, Graz, Austria) sandwiched between flat PP10 plates separated by a gap of 1.0 mm. A strain sweep was initially carried out to determine the linear viscoelastic region (LVE) for subsequent measurements at a frequency of 1 Hz and

temperature of 37°C (Zuidema, Rivet, Gilbert, & Morrison, 2014). The frequency sweeps were performed from 0.1 to 100 Hz at 1% strain and 37°C to determine storage modulus (G') and loss modulus (G''). To compare the elasticity of Org- and hm-ApGltn, the G' of the frequency sweep at 1 Hz was taken as the elastic modulus [118]. We also measured shear stress (τ) and viscosity (η) by changing the shear rate from 0.01 to 100 Hz at 37°C.

2.2.4. Degradation Profile

The degradation rate of C12-ApGltn hydrogel was measured using collagenase. A 200-μL volume of C12-ApGltn hydrogel was prepared in 2.5-mL tubes, and PBS was added to the tube to allow the hydrogel to swell. After 2 h, tubes containing the hydrogel were centrifuged, and the supernatant was removed and 500 μL of collagenase solution (10 U/ml in PBS) were added. After 15, 30, 60, 120, 240, 480, and 1080 min of incubation at 37°C, the tubes were centrifuged, and the supernatant discarded. The weight of the C12-ApGltn hydrogel was compared with the initial weight to determine the remaining % hydrogel volume.

2.2.5. In Vitro Cell Response

To evaluate the effect of C12-ApGltn on inflammatory cells, cell proliferation and the secreted amount of VEGF were examined using RAW264 cells, which were seeded on a 96-well plate at 2.0×10^4 cells/well and incubated overnight at 37°C and 5% CO_2. Org-, C6-, C12-, and C18-ApGltn were dissolved in PBS at 5 w/v% and sterilized by ultraviolet (UV) irradiation for 1 h. To assess the stimulation pathway of hm-ApGltn, cells were incubated with 30 mM of VIPER, a TLR4 inhibitor peptide for 1 h. Org-, C6-, C12-, and C18-ApGltn/PBS solutions at 5 w/v% were then diluted into each well to set at 0.5 w/v% followed by

incubation for 24 h. Cell viability was quantified with WST-8 reagent and LIVE/DEAD assay according to the manufacturer's instructions, and the viability of TCPS control was defined as 100% to calculate the %viability of cells cultured with each sample. The amount of VEGF secreted by RAW264 cells was determined with a Mouse VEGF enzyme-linked immunosorbent assay (ELISA) kit (Quantikine ELISA kit; R&D Systems, Minneapolis, MN, USA) according to the manufacturer's instructions.

2.2.6. In Vivo Experiments

Animal experiments were approved by the Animal Care and Use Committee of National Institute for Material Science (NIMS), Japan, and were performed in accordance with NIMS Regulations Pertaining to Animal Testing. A total of nine female Hos:HR-1 hairless mice (10–12 weeks old; Hoshino Laboratory Animals, Ibaraki, Japan) were used to evaluate the tissue response to the C12-ApGltn hydrogel and angiogenesis. Briefly, hydrogel samples were prepared by dissolving Org- or C12-ApGltn in PBS at 20 w/v% followed by UV sterilization for 1 h. A 500-μL volume of each sample was subcutaneously injected into the back of mice under isoflurane inhalation anesthesia. After 3 days, mice were sacrificed by intraperitoneal injection of somnopentyl. Skin tissue around the injection site was dissected, fixed with 10% formalin neutral buffer solution, embedded in paraffin, and cut into sections that were stained with haematoxylin and eosin (H&E) or labelled with antibodies against CD31, VEGF-A, and NF-κB (Abcam, Cambridge, UK). The labelled areas of tissue sections were quantified with Image J software.

2.2.7. Statistical Analysis

Data are shown as mean ± standard deviation and were analysed with the Student's t test. Differences were considered statistically significant at $P < 0.05$.

2.3 Results and discussion

2.3.1. Synthesis and characterization of hm-ApGltn

ApGltn was modified with hydrophobic groups by reductive amination between the fatty aldehyde and amino group of ApGltn. The yield of hm-ApGltn and modification ratio of hydrophobic groups are shown in Table 2-1. ApGltn modified with hexyl, dodecyl, and octadecyl groups are abbreviated as C6-ApGltn, C12-ApGltn, and C18-ApGltn, respectively. The actual/theoretical modification ratio decreased with increasing length of the hydrophobic group alkyl chain. This was due to hindrance of the reaction by self-aggregation of hm-ApGltn as the reaction proceeded. We also confirmed the modification of the hydrophobic group in hm-ApGltn by FT-IR and ^{1}H-NMR (**Figure A-1**). Two peaks at 1195 and 1300 cm^{-1} correlated with C-H rock and C-H scissoring, respectively, appeared in FT-IR spectra after the modification (**Figure A-1A**). Moreover, from the ^{1}H-NMR spectra, a strong peak originating from the alkyl carbon chain was observed at 1.25 ppm, which was consistent with those of each fatty aldehyde (**Figure A-1C**).

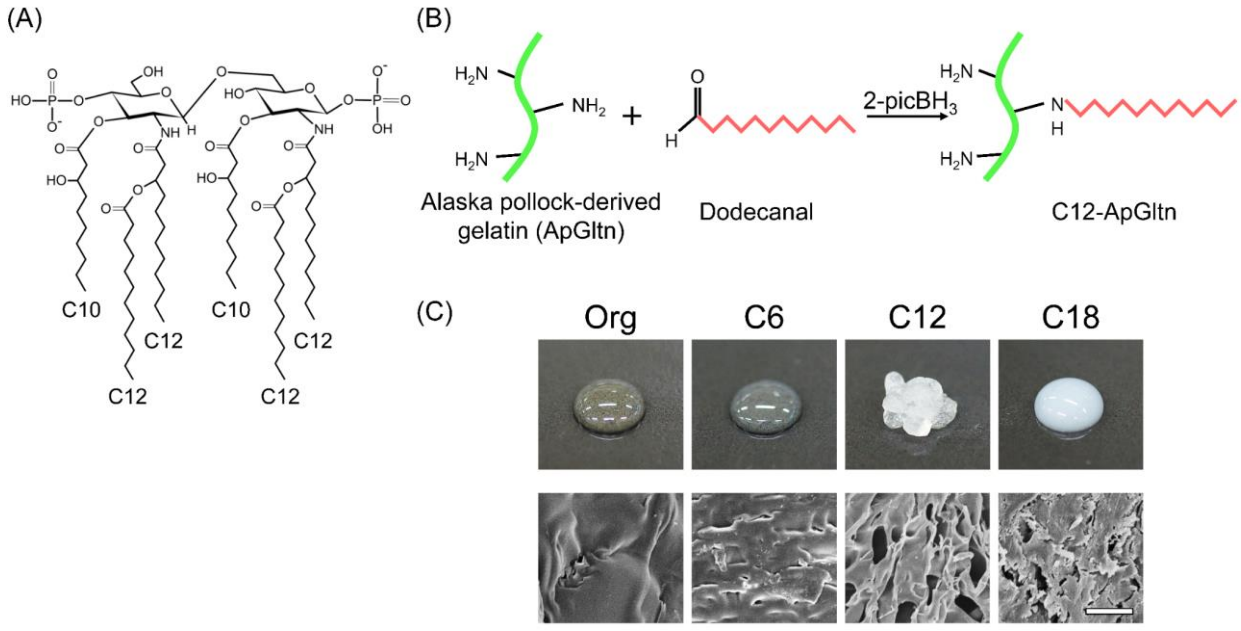

Figure 2-1. Synthesis of Alaska pollock gelatin-based hydrogel [119].
(A) Lipid A structure of Pseudomonas aeruginosa. (B) Synthesis of C12-ApGltn by reductive amination with dodecanal. (C) Solution/hydrogel of Org- and hm-ApGltn dissolved in PBS at 20 w/v%, and their microstructure observed by SEM. Scale bar = 20 μm.

Table 2-1. Modification ratio of hydrophobic groups on ApGltn and yield [119].

Abbreviation	Reagent	Reagent added (mol%)	Modification ratio (mol%)	% Yield (g/g)
C6-ApGltn	Hexanal	150	42	89
C12-ApGltn	Dodecanal	150	34	88
C18-ApGltn	Octadecanal	100	9	84

Interestingly, an aqueous solution of C12-ApGltn formed hydrogel (**Figure 2-1C**) despite the fact that ApGltn does not undergo a phase transition to a gel state at room temperature (25°C) due to a low imino acid content [110,111]. Moreover, the SEM observation of C12-ApGltn hydrogel showed microporous structures. This resulted from physical crosslinking caused by hydrophobic interactions between the dodecyl groups in C12-ApGltn. We previously reported a similar finding that C12-ApGltn hydrogel with a lower modification ratio crosslinked with poly(ethylene glycol) showed a higher elastic modulus compared to Org-ApGltn hydrogel [112].

On the other hand, the hexyl group in C6-ApGltn was not sufficiently hydrophobic to form physical crosslinks. The C18-ApGltn solution was opaque since C18-ApGltn has a highly hydrophobic octadecyl group and is presumed to form a hydrophobic colloid-like solution. The SEM image of C18-ApGltn solution showed the aggregated structure because of a highly hydrophobic octadecyl group, resulting in hydrophobic colloid-like solution and opaqueness of C18-ApGltn solution.

2.3.2. Rheological properties

We initially measured strain sweep to deter mine the LVE region for subsequent study. G' and G" of the C12-ApGltn hydrogel in the strain sweep test confirmed a near-parallel profile in the range of the strain

sweep (**Figure A-2**). We therefore set the strain to 1% for frequency sweep measurements (**Figure 2-2A**). G' exceeded G" over the entire range of the frequency sweep, indicating that strong intermolecular hydrophobic interactions between dodecyl groups lead to the formation of a physical crosslink network. We then measured shear stress and viscosity to evaluate the pseudoplastic properties of the C12-ApGltn hydrogel (**Figure 2-2B**). The shear stress of the hydrogel showed a thixotropic-like profile; moreover, viscosity decreased with increasing shear rate, indicating a shear-thinning property. Thus, 20 w/v% C12-ApGltn solution was determined to be injectable through an 18-G needle. The storage modulus of the C12-ApGltn hydrogel was 10 times higher than that of an injectable hydrogel with non-covalent crosslinking consisting of β-cyclodextrin vesicle and adamantane-modified hydroxyethyl cellulose [120], indicating weaker thixotropic and shear-thinning properties comparable to those of covalently crosslinked polymers.

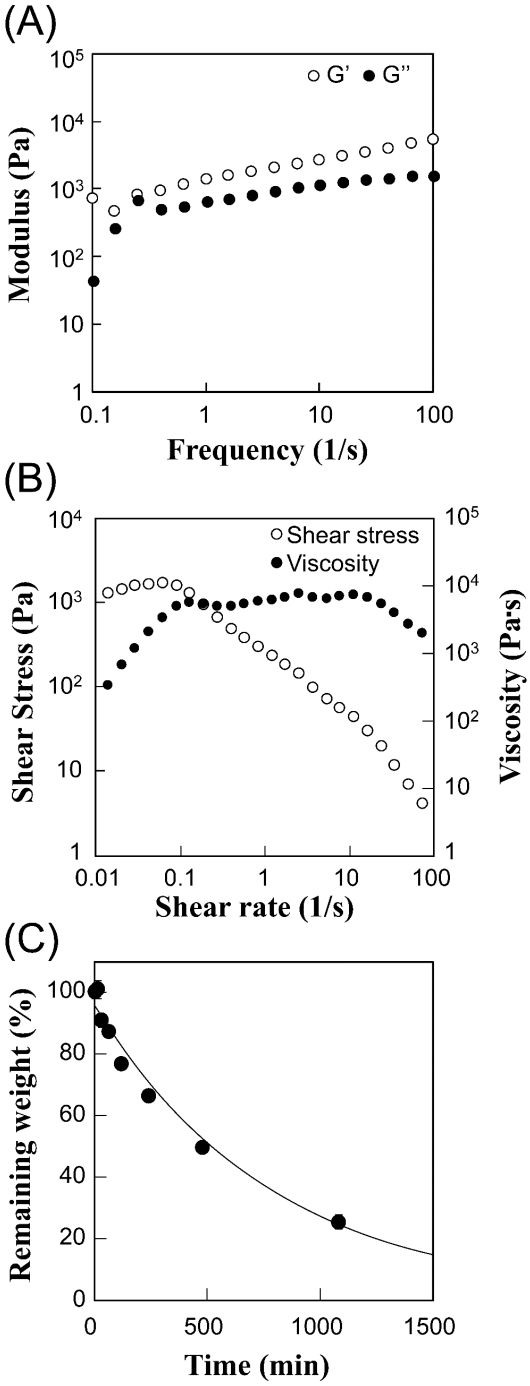

Figure 2-2. Viscoelastic properties of C12-ApGltn hydrogel at 20 w/v% [119].
(A) Storage modulus (G') and loss modulus (G") of C12-ApGltn hydrogel measured by frequency sweep at 1% strain. (B) Shear stress and viscosity measured by changing the shear rate. (C) Enzymatic degradation of C12-ApGltn hydrogel treated with collagenase at 37°C.

2.3.3. Degradation behavior of C12-ApGltn hydrogel

The enzymatic degradation of C12-ApGltn hydrogel was evaluated by adding collagenase solution to the hydrogel, which digested the gelatin peptide chain. That is, the hydrogel gradually degraded into the aqueous phase, and the remaining weight was less than 30% of the initial weight after incubation for 18 h (**Figure 2-2C**). Collagenase can cleave the Gly-Leu-Ala or Gly-Ile-Ala sequences of collagen, which are also frequently found in gelatin [121]. Thus, C12-ApGltn hydrogel is expected to be degradable in vivo since in addition to collagenase, other matrix metalloproteinases such as gelatinase are present in animals.

2.3.4. Stimulation of VEGF secretion by hm-ApGltn in vitro

The effect of hm-ApGltn on cell viability and VEGF secretion were evaluated using macrophage-like RAW264 cells since macrophages play an important role in inflammation as well as angiogenesis in vivo. We initially assessed cell viability after culturing in Org- or hm-ApGltn containing medium for 24 h (**Figure 2-3A**). Viability was higher in cells cultured with Org-ApGltn compared with the tissue culture polystyrene (TCPS) control. Moreover, there were no differences in viability among cells cultured on C6- or C12-ApGltn and Org-ApGltn, although viability was lower on C18-ApGltn. On the other hand, using LIVE/DEAD assay to quantify the % live cell compared with TCPS control, cells cultured with Org-, C6-, C18-ApGltn as well as LPS showed similar results when assessed with WST-8 **(Figure 2-3B)**. However, C12-ApGltn induced the decreased cell viability by 15% compared with the results measured by WST-8. This was likely due to the hydrophobicity of hm-ApGltn. In this study we used hexanal, dodecanal, and octadecanal with alkyl chain lengths of 6, 12, and 18, respectively, to modify ApGltn; these aqueous solutions or hydrogels had significantly different properties from those described above. Thus, the length of alkyl chain affects hydrogel morphology

to a greater extent than modification ratio. LPS at 10 EU/mL also had no effect on viability, with no difference compared with TCPS.

We also evaluated a secretion and inhibition of VEGF by RAW264 cells following treatment with Org- and hm-ApGltn compared with TCPS as a control **(Figure 2-3C)**. Although the concentration of VEGF secreted from RAW264 cultured with Org- and C6-ApGltn was under the detection limit, C12- and C18-ApGltn stimulated VEGF secretion 4.6 and 24.8-fold compared with TCPS. LPS at 10 EU/mL induced 26-fold higher secretion of VEGF than TCPS control. On the other hand, the effect of the stimulation by C12- and C18-ApGltn as well as LPS was suppressed when treated with VIPER. These results indicated that a hydrophobic group induced an inflammatory response in RAW264 cells via TLR4-mediated signalling in a manner similar to LPS, which first binds to CD14 on the cell membrane and then inserts five out of its six lipid chains into the hydrophobic pocket of myeloid differentiation (MD)2, leading to the formation of

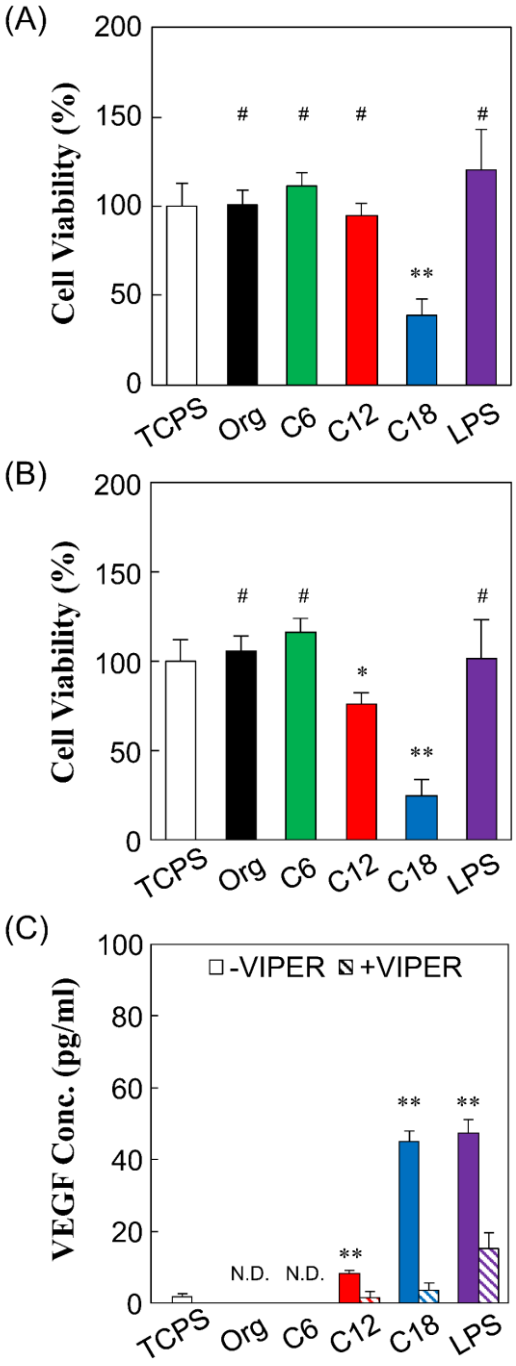

Figure 2-3. In vitro cell responses on hm-ApGltn[119].

Cell viability % compared with the TCPS control was evaluated with (A) WST-8 reagent and (B) LIVE/DEAD assay. #$P > 0.05$, *$P < 0.05$, **$P < 0.01$ ($n = 6$). (C) Quantitative analysis of secreted VEGF concentration from RAW264 cultured with Org- and hm-ApGltn with and without VIPER, a TLR-4 inhibitor peptide. **$P < 0.01$ ($n = 4$).

the LPS–MD2–TLR4 complex [107,122]. The TLR4-mediated inflammation pathway includes the activation of NF-κB, which is a promoter of VEGF gene, through a MyD88–TIR domain-containing adaptor protein (TIRAP)-dependent pathway [104]. Hence, C12- and C18-ApGltn were considered to activate NF-κB via MyD88–TIRAP signalling and promote VEGF secretion. To sum up, Org- and C6-ApGltn had no effects on RAW264 cell viability or VEGF secretion. C12-ApGltn induced slightly negative effect on cell viability and stimulated VEGF secretion from RAW264 cells. On the other hand, C18-ApGltn promoted VEGF secretion to a greater extent than C12-ApGltn, but negatively affected cell viability. Interestingly, LPS enhanced VEGF secretion while maintaining preserving cell viability.

2.3.5. Stimulation of angiogenesis by hm-ApGltn in vivo

Based on our in vitro observations that C12-ApGltn stimulates VEGF secretion in RAW264 cells, we hypothesized that C12-ApGltn can also promote VEGF secretion and angiogenesis in vivo without addition of any growth factors. Three days after injection into mice, the tissue at the site of injection appeared similar in the Org-ApGltn and PBS (control) groups, with no evidence of angiogenesis (**Figure 2-4**). In contrast, a substantial number of capillaries were observed around the site of C12-ApGltn hydrogel injection.

To investigate the tissue response to the hydrogel in greater detail, we performed histological and immunohistochemical analyses of tissue sections following injection of Org- and C12-ApGltn hydrogels. At the site of C12-ApGltn hydrogel injection, the number of NF-κB-expressing cells was increased in interstitial connective tissue (ICT); this was accompanied by increased VEGF secretion in ICT and panniculus carnosus (PC) (**Figure 2-5A**). However, no NF-κB-positive cells were present in ICT and only weak NF-κB immunoreactivity was observed in the PC in mice injected with PBS or Org-ApGltn solution. CD31 immunolabeling and H&E staining revealed almost no blood vessels in ICT around the sites of PBS and Org-

ApGltn injection, whereas C12-ApGltn hydrogel promoted new blood vessel formation in ICT as well as a perfusion of red blood cells in the lumen. A quantitative analysis of NF-κB, VEGF, and CD31 immunoreactivity showed that the NF-κB-positive area was over two times larger in mice injected with C12-

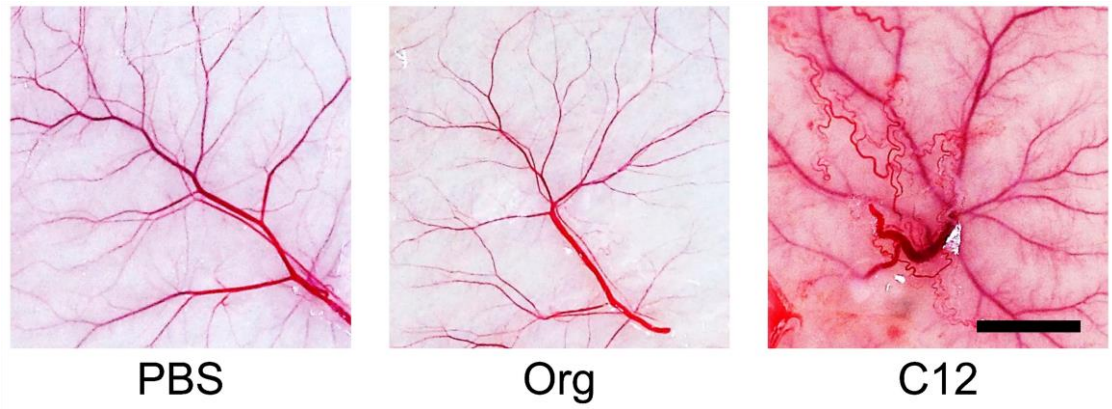

Figure 2-4. Gross morphology of tissue 3 days after injection of C12-ApGltn hydrogel [119].
Scale bar = 3 mm.

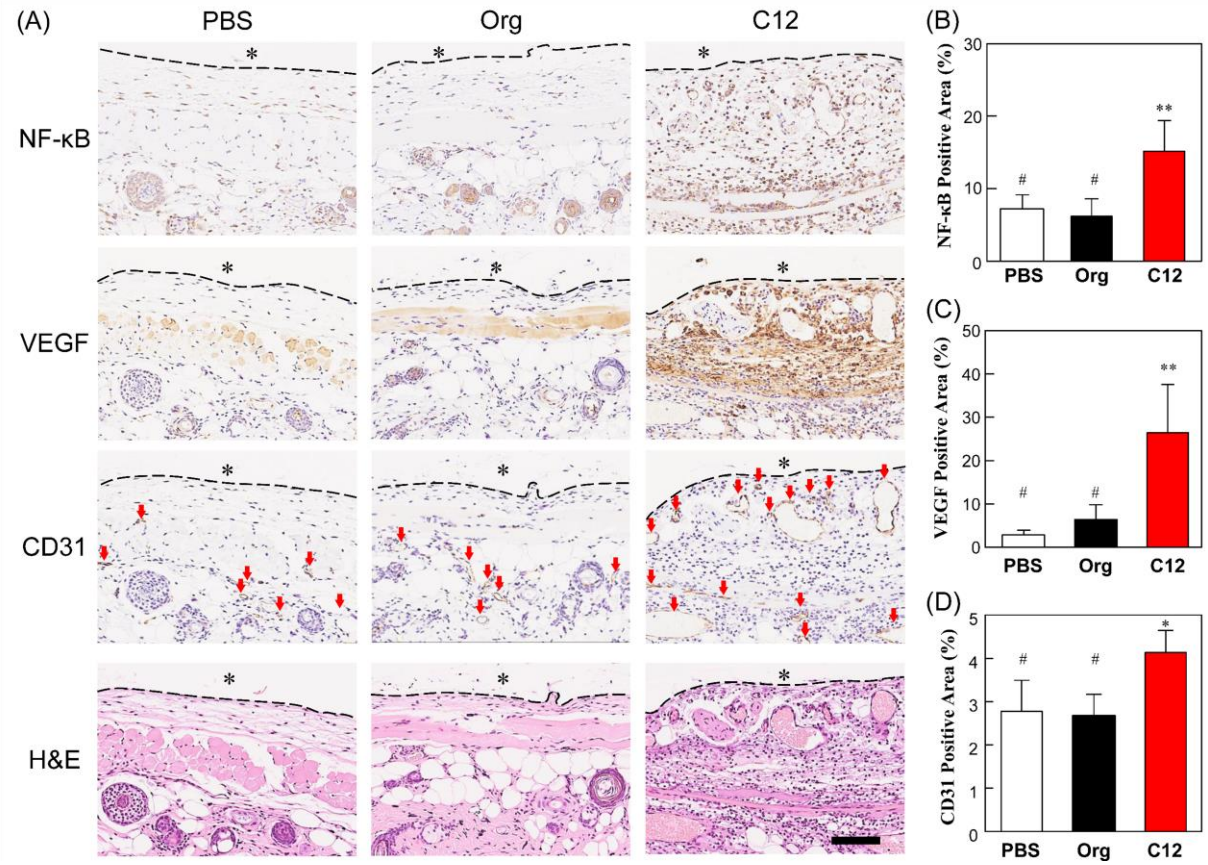

Figure 2-5. Histological analysis 3 days after subcutaneous injection of hydrogel into mice [119].
(A) Sections of tissue around site of PBS, Org-ApGltn, and C12-ApGltn injection (*) with H&E staining and NF-κB, VEGF, and CD31 immunolabeling. Red arrows indicate capillaries. Scale bar = 100 μm. (B–D) Quantification of area positive for (B) NF-κB, (C) VEGF, and (D) CD31 (%). #P > 0.05, *P < 0.05, **P < 0.01 (n = 9).

ApGltn hydrogel compared with PBS or Org-ApGltn (**Fi gure 2-5B**). A similar trend was observed for VEGF (nine- and four-times larger areas, respectively; **Figure 2-5C**). These results suggest that C12-ApGltn causes inflammation as evidenced by elevated NF-κB expression, leading to increased VEGF secretion. Gelatin has lower immunogenicity and higher degradability compared with collagen, and its hydrogel induces only initial foreign body reaction after in vivo implantation, which ameliorate as the progressive degradation of materials [123]. The modification of hydrophobic groups causes the immunogenic response through TLR4-mediated pathway and induced the enhanced secretion of NF-κB, leading to the secretion of pro-inflammatory cytokines. However, C12-ApGltn was not considered to completely bind to MD2 and induce weaker signalling than LPS because LPS is recognized by MD2 with multiple alkyl carbon chains, whereas, C12-ApGltn has only 3 dodecyl groups exist in one gelatin.

We also examined the expression of the endothelial cell marker CD31 to evaluate the effect of the hydrogel on angiogenesis. The CD31-positive area around the injection site was 1.5 times larger in the C12-ApGltn hydrogel group than in the PBS and Org-ApGltn groups (**Figure 2-5D**), indicating that C12-ApGltn hydrogel induced endogenous VEGF secretion and angiogenesis in vivo. Given our findings from in vitro and in vivo experiments, we propose the following mechanism for C12-ApGltn-induced angiogenesis (**Figure 2-6**): (1) activation of TLR4 induces an inflammatory response in

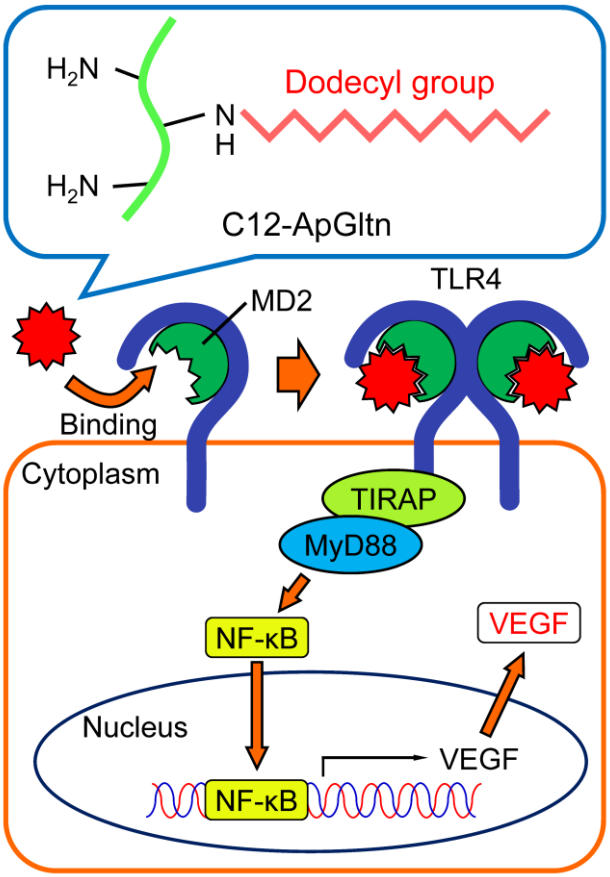

Figure 2-6. Proposed mechanisms of angiogenesis induced by injectable C12-ApGltn hydrogel [119].

macrophages, followed by NF-κB activation via MyD88-mediated pathways; (2) VEGF, which is the downstream of NF-κB, is secreted by macrophages; and (3) VEGF binds to VEGF receptor on the endothelial cell membrane, leading to vasculogenesis.

2.4 Conclusions

We developed a C12-ApGltn hydrogel that stimulates endogenous VEGF secretion and angiogenesis without addition of any drugs or growth factors. C12-ApGltn dissolved in PBS at 20% formed an injectable hydrogel with thixotropic properties that did not significantly affect the viability of RAW264 cells compared with TCPS and Org-ApGltn but induced inflammation, VEGF secretion, and angiogenesis to a greater extent. The angiogenic mechanism of C12-ApGltn was attributable to the activation of TLR4–NF-κB signalling, which stimulated VEGF secretion and consequently, the proliferation of endothelial cells. These results demonstrate that C12-ApGltn is a promising material for enhancing the survival of implanted cells and tissues by promoting local angiogenesis.

CHAPTER 3: Self-assembled Dodecyl Group-modified Gelatin Microparticle-based Hydrogels with Angiogenic Property

3.1. Introduction

Angiogenesis is necessary for the proliferation of implanted cells or tissues to supply oxygen and nutrients from host tissue. The incorporation of growth factors into biocompatible materials is a major strategy to induce angiogenesis before or during the transplantation of cells. Tabata *et al*. demonstrated vascular endothelial growth factor (VEGF) incorporated into a collagen hydrogel that showed a controlled release profile of VEGF and angiogenesis in vivo [94]. Peattie *et al*. reported a hyaluronic acid hydrogel crosslinked with poly(ethylene glycol) incorporated with VEGF and keratinocyte growth factor (KGF) [96]. This hydrogel induced microvascular formation around the implant site by the released VEGF and KGF. Although these growth factors effectively promote angiogenesis, their instability under physiological conditions is considered a limitation to their practical application [52] because VEGF and fibroblast growth factor-2 (FGF-2) have half-lives of only 50 and 9.6 min, respectively [54,55]. To overcome these problems, we focused on the use of endogenous growth factors to achieve angiogenesis. Proangiogenic growth factors such as VEGF are mainly secreted from macrophages in response to ischemia, injury and inflammation [124].

Saturated fatty acids (SFAs), such as capric acid (C10), lauric acid (C12) and palmitic acid (C16), behave like lipopolysaccharide (LPS), which is a component of the outer membrane of gram-negative bacteria

[98,99,103]. SFAs induce toll-like receptor 4 (TLR4)-mediated inflammation and enhance the secretion of proinflammatory cytokines such as tumor necrosis factor (TNF)-α [104–109]. We previously reported that a porous gelatin sponge comprising hydrophobically modified gelatin (hm-Gltn) induced angiogenesis in vivo without incorporating growth factors [97]. We also reported that a dodecyl group-modified (C12) Alaska pollock-derived gelatin (ApGltn) (C12-ApGltn), which mimics an LPS of *Pseudomonas aeruginosa* **(Figure 3-1A)**, formed a self-assembled hydrogel that stimulated VEGF secretion in vitro and in vivo through TLR4-mediated pathways [119]. Although the C12-ApGltn self-assembled hydrogel stimulated angiogenesis in vivo by itself without additional growth factors, the resulting hydrogel did not achieve sustained angiogenesis because of its fast degradation and dispersion in vivo. Furthermore, we recently reported that micrometer-sized particles based on hydrophobically modified ApGltn can be obtained using a coacervation method [125]. The resulting particle formed an enzymatically stable, self-assembled particle-based hydrogel when in contact with water.

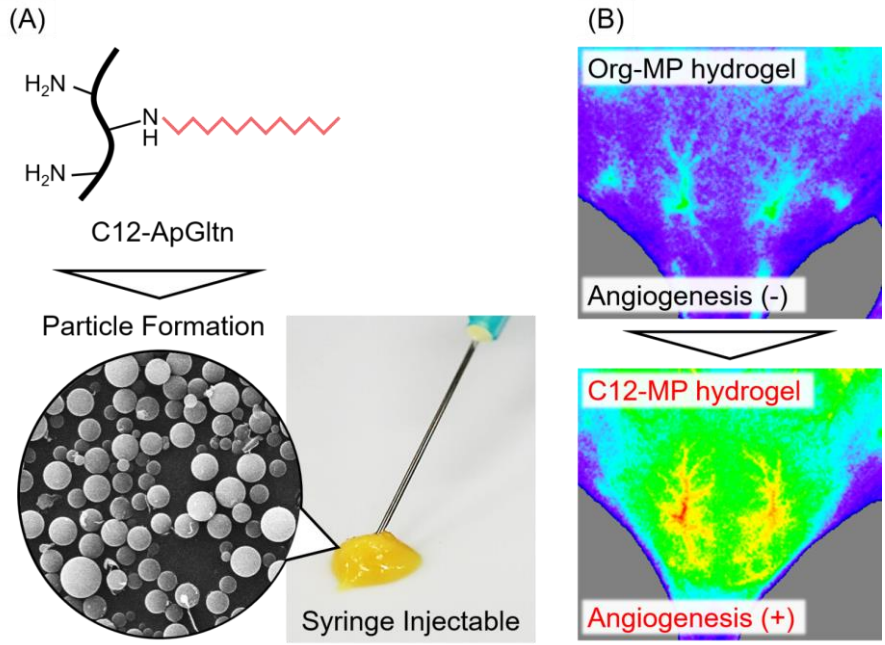

Figure 3-1. Overview of the angiogenic C12-MP hydrogel [126].
(A) The LPS-mimicking structure of C12-ApGltn. The aqueous suspension of C12-MP had shear-thinning properties and was injectable through a needle. (B) The increased blood flow in the C12-MP hydrogel-injected site.

In this chapter, C12-ApGltn was made into microparticles followed by thermal crosslinking to enhance degradation resistance for sustained angiogenesis. We characterized the hydrophobicity, enzymatic degradation rate and rheological properties of the resulting particle-based hydrogels followed by in vivo angiogenesis evaluations **(Figure 3-1B)**.

3.2. Experimental

3.2.1. Materials

ApGltn (molecular weight = 33,000) was purchased from Nitta Gelatin (Osaka, Japan). Dodecanal was purchased from Tokyo Chemical Industry (Tokyo, Japan). 2-Picoline borane (pic-BH_3) was purchased from Junsei Chemical (Tokyo, Japan). Collagenase, water-soluble tetrazolium (WST)-8 reagent (Cell Count Reagent SF) and Dulbecco's phosphate-buffered saline (PBS) were obtained from Nacalai Tesque (Kyoto, Japan). 2,4,6-Trinitrobenzenesulfonic acid (TNBS), triethylamine, 2-aminoethanol, ethanol, dimethyl sulfoxide (DMSO) and 10% formalin neutral buffer solution were purchased from Wako Pure Chemical Industries (Osaka, Japan). Minimum essential media (MEM)-α, MEM nonessential amino acids (NEAAs) and penicillin-streptomycin (Pen Strep) were purchased from Thermo Fischer Scientific (MA, USA). Fetal bovine serum (FBS) was purchased from Sigma-Aldrich (MO, USA). The TLR4 peptide inhibitor set (VIPER) was purchased from Novus Biologicals (CO, USA). Ultrapure LPS-EB was purchased from InvivoGen (CA, USA).

3.2.2. Synthesis and Characterization of C12-ApGltn

Quantification of the amino groups in ApGltn was initially conducted using the TNBS method as previously reported [112,113,115,127]. Briefly, 100 μL of ApGltn dissolved in a 50% DMSO/H_2O solution at 0.5 w/v% was dispensed into a 48-well plate followed by the addition of TNBS and triethylamine dissolved in 1% DMSO/H_2O. After shaking for 1 min, the microplate was incubated for 2 h at 37°C. The absorbance at 335 nm

was measured with a microplate reader (Spark 10M; Tecan, Männedorf, Switzerland), and the number of amino groups was calculated using a calibration curve generated by 2-aminoethanol instead of ApGltn.

ApGltn was modified with a dodecyl group by reductive amination [116,117,128,129] as previously described [112,130] **(Figure 3-2A)**. Briefly, ApGltn was dissolved in 30% EtOH/H_2O at 20 w/v%, and 1.5 eq of dodecanal on the remaining ApGltn amino groups dissolved in ethanol was added. After an 18-h reaction, the solution was added dropwise to 10 times the volume of cold ethanol to precipitate C12-ApGltn. The precipitate was filtered under vacuum and washed three times with EtOH to remove unreacted reagents and 2-picBH_3. The precipitate was then vacuum dried at room temperature (25°C) to obtain C12-ApGltn as a white powder and subsequently weighed. Nonmodified ApGltn (Org-ApGltn) was similarly synthesized but without the addition of dodecanal or 2-picBH_3. The modification ratio of C12-ApGltn was quantified using the TNBS method by comparing the absorbance at 335 nm with that of Org-ApGltn. Modification of the hydrophobic groups was confirmed by Fourier transform infrared spectroscopy (FT-IR) (ALPHA II; Bruker Corp., Billerica, MA, USA) and ^{1}H nuclear magnetic resonance (^{1}H-NMR, JNM-AL300; JEOL, Tokyo, Japan). The modification ratio of the dodecyl group was also calculated by comparing the Org- and C12-ApGltn spectra. The arginine-based peak at 2.95 to 3.25 ppm was normalized in each spectrum, followed by comparing the peak integration of the ε-methylene protons of lysine (2.70 to 2.90 ppm).

3.2.3. Preparation of the ApGltn Microparticles

Although the aqueous solution of C12-ApGltn became a hydrogel due to the hydrophobic crosslinking between dodecyl groups, the hydrogel was easily dispersed into water. Therefore, C12-ApGltn was transformed into microparticles by coacervation followed by thermal crosslinking to improve water resistance [131]. Briefly, Org- and C12-ApGltn were dissolved in distilled water and a 20% EtOH/H_2O solution at 5 w/v%,

respectively. EtOH was added to each solution with vigorous stirring to dilute each solution 2-fold and precipitate the microparticles. The solution with microparticles was cooled at −20°C for 18 h followed by lyophilization. The resulting Org- and C12-microparticles (MPs) were subjected to mortar pulverization and sieving using a 32-μm opening mesh. Org- and C12-MPs were then placed on a holder with carbon tape for scanning electron microscopy (SEM). (S-4800 ultrahigh-resolution SEM, HITACHI, Japan). Platinum was sputtered on the MPs at a thickness of 10 nm. The particle size was quantified from nine SEM images using ImageJ software. The polydispersity index (PDI) of the MPs was calculated by the following equation [132,133]

$$PDI = \left(\frac{\sigma}{d}\right),$$

where σ and d indicate the standard deviation and average diameter of the MPs, respectively. The obtained MPs were then thermally crosslinked under vacuum at 150°C for 3, 6 and 9 h to introduce MPs with degradation resistance (MP3, MP6 and MP9, respectively). The remaining amino group of the MPs after thermal crosslinking was determined by the TNBS method with slight changes. Briefly, MP3, MP6 and MP9 were dissolved in a 50% DMSO/H_2O solution at 0.5 w/v% followed by incubation for 2 h at 50°C. Next, 100 μL of solution was transferred to a 48-well plate, and 100 μL of 1% TNBS solution and 1% TEA solution were added to each well. After 2 h of incubation at 37°C, the reaction was stopped by the addition of 50 μL of 6 N HCl. The absorbance at 335 nm was measured for each well to determine the remaining number of primary amino groups in the Org- and C12-MPs.

3.2.4. Surface Contact Angle of the Particles

To determine the hydrophobicity of thermally crosslinked Org- and C12-MPs, the surface contact angle was measured by the sessile-drop method [130]. Briefly, double-sided tape was pasted on the slide glass and then covered with Org- and C12-MPs. The contact angle measurements started 0.5 s after a 3 μL PBS

droplet was dropped on the MP surface using DropMaster DM701 (Kyowa Interface Science, Japan) for 15 s.

3.2.5. Rheological Properties

Org- and C12-MPs were dispersed in PBS at 40 w/v% to form a particle suspension. These suspensions were placed on the stage of an MCR 301 rheometer (Anton Paar GmbH, Graz, Austria) sandwiched between flat PP10 plates separated by a gap of 1.0 mm. A strain sweep was initially carried out to determine the linear viscoelastic region (LVE) for subsequent measurements at a frequency of 1 rad/s and temperature of 37°C [134]. Frequency sweeps were performed from 0.1 to 100 rad/s at 1% strain and 37°C to determine the storage modulus (G′) and loss modulus (G″). To compare the elasticity of Org- and C12-ApGltn, the G′ of the frequency sweep at 1 rad/s was taken as the elastic modulus [135]. Moreover, the effect of the shear rate on the viscosity was also measured to evaluate the behavior of the MP suspension during syringe injection. The same samples used in the strain and frequency sweep were employed to measure the viscosity with a changing shear rate from 0.01 to 1 Hz at 37°C.

3.2.6. Degradation Test

The enzymatic degradation rates of the Org- and C12-MPs were evaluated using collagenase. Briefly, 80 mg of C12-ApGltn was dissolved in 200 μL of PBS to prepare the hydrogel in 2.5-ml tubes followed by the addition of PBS to the tube to allow the hydrogel to swell for 2 h. After centrifuging the tubes to precipitate the particles, the supernatant was removed, and 500 μL of collagenase solution (10 U/ml in PBS) was added. After up to 1080 min of incubation at 37°C, the tubes were centrifuged to separate the hydrogel from the supernatant, and the supernatant was discarded. The weight of the C12-MP hydrogel was compared with the initial weight to determine the remaining % hydrogel volume.

3.2.7. In Vitro Cell Response

Mouse macrophage-like RAW264 cells were cultured in MEM α supplemented with 10% FBS, 1% NEAAs and 1% Pen Strep. Cells were then seeded on a 96-well plate at 2.0×10^4 cells/well and incubated for 18 h at 37°C and 5% CO_2. Org- and C12-MPs dispersed in PBS at 0.5, 1 and 2 w/v% were sterilized by ultraviolet (UV) irradiation for 1 h. To confirm the TLR4-mediated pathway, VIPER, a TLR4 blocking peptide, was added at 30 mM to the culture medium followed by incubation for 1 h [136]. Org- and C12-MP suspensions were then added to the culture plate at a 10-fold dilution to obtain final concentrations of 0.05, 0.1 and 0.2 w/v%. RAW264 cells were also cultured in media supplemented with and without 10 ng/ml LPS as a positive and negative control, respectively. After incubation for 24 h, the supernatants were separated for the enzyme-linked immunosorbent assay (ELISA) followed by evaluation of the cell viability using a WST-8 reagent according to the manufacturer's instructions. The amounts of secreted VEGF and TNF-α were quantified with an ELISA kit (Quantikine ELISA kit; R&D Systems, Minneapolis, MN, USA) according to the manufacturer's instructions.

3.2.8. Subcutaneous Implantation of the C12-MP and Laser Doppler Perfusion Imaging (LDPI) Evaluation

Animal experiments were approved by the Animal Care and Use Committee of National Institute for Material Science (NIMS), Japan, and performed in accordance with NIMS Regulations Pertaining to Animal Testing. Hos:HR-1 hairless mice (4 weeks old; Hoshino Laboratory Animals, Ibaraki, Japan) were used to evaluate the tissue response of the Org- and C12-MP hydrogels. Briefly, Org- and C12-MPs were dispersed in PBS at 40 w/v% followed by UV sterilization for 1 h. Next, 50 μL of each sample was injected through a 21-gauge needle into the backs of the mice exposed to inhalational anesthetics. LDPI measurements were performed immediately after implantation and for up to 22 days using an OZ-2Pro (OMEGAWAVE, Tokyo,

Japan). To stabilize the blood flow in different mice, the respiratory rate was set to once per second. For the histological studies, PBS, Org-MP3 and C12-MP3 hydrogels were subcutaneously injected into mice, and after 2 days, the mice were sacrificed by intraperitoneal injection of a lethal dose of somnopentyl. The skin tissue around the injection site was dissected and fixed with a 10% formalin neutral buffer solution. The fixed tissues were then embedded in paraffin and cut into sections followed by staining with hematoxylin and eosin (H&E) or labeling with antibodies against CD31, NF-κB, and myeloperoxidase (MPO) (Abcam, Cambridge, UK). The labeled areas of the tissue sections were quantified using ImageJ software.

3.2.9. Statistical analysis

Data are shown as the mean ± standard deviation and were analyzed with Student's t test. Differences were considered statistically significant at $p < 0.05$. One-way analysis of variance (ANOVA) followed by the Tukey–Kramer method was used to determine whether there were any statistically significant differences between the means of three or more independent groups.

3.3. Results and Discussion

3.3.1. Synthesis of C12-ApGltn

The yields of the obtained Org- and C12-ApGltn were 90.2 and 81.6%, respectively. The modification ratio of the dodecyl group in C12-ApGltn was 32.6 mol% for the total amount of amino residues in ApGltn **(Table 3-1)**. The modification ratio of the dodecyl group in C12-ApGltn was also calculated by NMR spectroscopy **(Figure A-3A)**. The integration of the Arg peak at 2.95 to 3.25 ppm was normalized to 1.0 **(Figure A-3C)** [137,138]. The peak integrations of the ε-methylene protons of lysine at 2.70 to 2.90 ppm in Org- and C12-ApGltn were 0.562 and 0.435, respectively, indicating a 29% decrease in the ε-methylene of lysine by dodecyl modification **(Figure A-3B, C)**. Therefore, quantitation of the modification ratio from the NMR

spectra was correlated with that from the TNBS method.

Table 3-1. Characterizations of Org- and C12-MPs [126].

Abbreviation	Modification ratio (mol%)	Average diameter (μm)	PDI (–)	Crosslinking time (h)	Half-life in collagenase solution (h)
Org-MP	–	2.66	0.34	–	–
-MP3	–	–	–	3	7.18
-MP6	–	–	–	6	9.47
-MP9	–	–	–	9	9.07
C12-MP	32.6	2.22	0.27	–	–
-MP3	–	–	–	3	19.58
-MP6	–	–	–	6	21.82
-MP9	–	–	–	9	20.86

The modification ratio of the dodecyl group in C12-ApGltn was measured before transformation into C12-MPs. The average diameter and PDI were calculated from the SEM images. The half-lives of the Org- and C12-MP hydrogels under physiological conditions were calculated from the degradation profile **(Figure 3-4F)**.

3.3.2. Preparation and characterization of Org- and C12-MPs

SEM images of Org- and C12-MP showed that these particles were successfully formed with a spherical shape using the coacervation method, and almost no deformed particles were observed **(Figure 3-2B)**. The particle diameter distribution was calculated from SEM images using ImageJ software **(Figure 3-2C, D)**. Most of the diameters of the MPs were distributed within 1 – 4 μm; however, the number of C12-MPs with diameters smaller than 1 μm was greater than that of the Org-MPs. Moreover, there were almost no C12-MPs larger than 5 μm, whereas approximately 10% of the Org-MPs exceeded 5 μm in diameter. These results correlated with the higher PDI of Org-MP than C12-MP (Table 1). Additionally, we observed hydrophobic moieties on the surface of the C12-MPs using FT-IR. **Figure A-4** shows the FT-IR spectra of the Org- and C12-MPs. The absorbances at 2853 and 2927 cm^{-1}, which correlate to C-H stretching, were increased in the spectrum of C12-MP, which indicates that the dodecyl group existed on the surface of C12-MP. The remaining

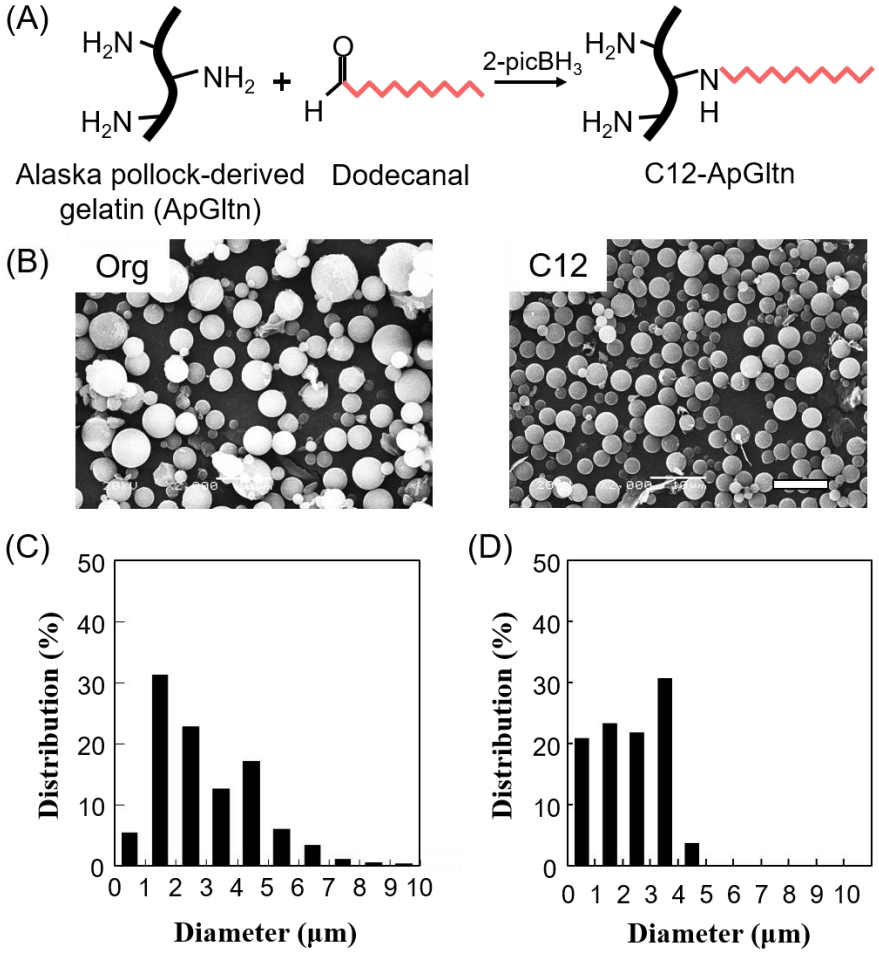

Figure 3-2. The fabrication of C12-ApGltn and MPs [126].
(A) Synthesis of C12- ApGltn. (B) SEM images of the Org- and C12-MPs (scale bar = 10 μm) and particle diameters of the (C) Org-MPs and d C12-MPs calculated by ImageJ software.

amino groups of Org- and C12-MPs with different thermal crosslinking times were evaluated using the TNBS method. **Figure A-5** shows the relative ratio of the remaining amino groups in the Org- and C12-MPs with thermal crosslinking compared with that in Org- and C12-ApGltn. The remaining amino groups significantly decreased with increasing thermal crosslinking time, indicating successful covalent crosslinking. However, there was no significant difference between Org- and C12-MP crosslinked for 6 and 9 h due to fewer amino groups in C12-ApGltn because of the approximately 33% modification. Therefore, only a few amino groups in C12-ApGltn could contribute to the formation of an amide bond with a carboxylic acid during thermal crosslinking.

3.3.3. *Contact angle measurements*

The contact angles of the Org- and C12-MPs were measured to evaluate the bulk hydrophobicity of the MPs. **Figure 3-3A** shows the PBS droplets on the Org-MP6 and C12-MP6 layers. The PBS droplet was more quickly absorbed onto Org-MP6 than the C12-MP6 layer. The time course of the surface contact angle on MP3, MP6 and MP9 indicated a significantly faster decrease of the contact angle on Org- and C12-MP3, whereas Org-MP6 and Org-MP9, as well as C12-MP6 and C12-MP9, showed similar behavior in the decrease of the contact angle **(Figure 3-3B)**. **Figure 3-3C** compares the contact angles on the MP layers at 15 s and indicates that only Org- and C12-MP3 had significantly lower contact angles than Org- and C12-MP6 and Org- and C12-MP9. Although modification with the dodecyl group contributed to the significant difference in

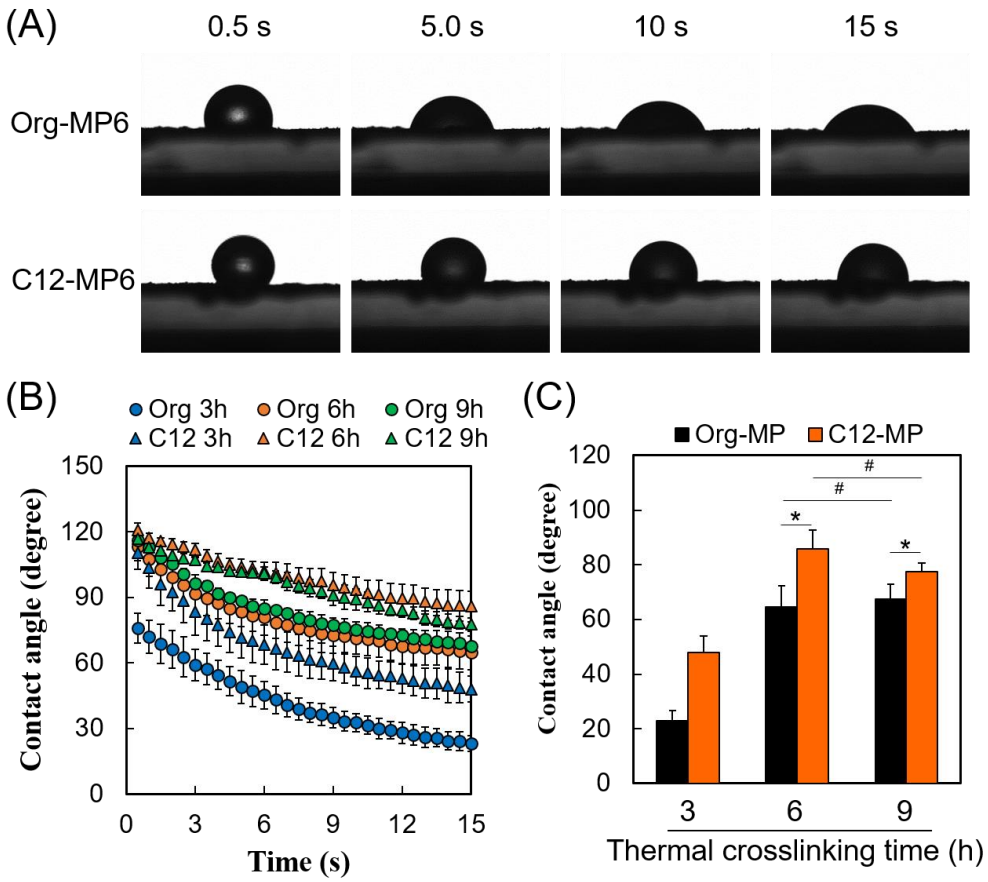

Figure 3-3. Surface contact angle measurements of the Org- and C12- MPs [126]**.**
(A) Representative images of the behavior of PBS droplets on the Org-MP6 and C12-MP6 surfaces for 15 s. (B) Surface contact angle measurements over 15 s (n = 3). (C) Comparison of the contact angle on Org- and C12-MPs at 15 s. *p < 0.5, #p > 0.05.

the surface contact angle, there was no significant difference between the MP6 and MP9 layers. The longer thermal crosslinking significantly affected the crosslinking ratio **(Figure A-5)**, but that difference was not considered dominant regarding the surface contact angle and water absorption. On the other hand, from a topological perspective, the C12-MP layer was considered to be smoother than the Org-MP layer because the C12-MPs contained a larger number of smaller particles than the Org-MPs. Therefore, the increased contact angle of the C12-MPs was attributed to not only the increased hydrophobicity but also the decreased surface roughness of the C12-MP layers.

3.3.4. Viscoelastic properties of the C12-MPs

Before measuring the frequency sweep, the linear viscoelastic region (LVE) was determined by the strain sweep **(Figure A-6A, B)**. The LVE indicates the strain range in which the measurement can be executed without breaking the samples. Therefore, the strain was set at 1% to measure the frequency sweep. The frequency sweep measurement results showed that the storage modulus (G′) of the Org- and C12-MP suspensions exceeded their loss modulus (G″) within the frequency range **(Figure 3-4A, B)**, which indicates that all concentrations of the Org- and C12-MP suspensions formed a hydrogel. Thermal crosslinking promoted dehydration condensation between the carboxylic group and amino group in ApGltn, preventing its decomposition in water. Moreover, Org- and C12-MP absorbed water and swelled into a microgel-like condition, which formed the hydrogel as a whole. Alternatively, the effects of the change in the crosslinking time were also evaluated. The G′ of the hydrogels was dependent on the hydrodynamic radius of the swollen MPs. A longer crosslinking time led to increased amide bonding formation and crosslinking density of the surface of MPs, resulting in a lower swelling ratio and smaller hydrodynamic radius. Therefore, Org- and C12-MP3, which have lower crosslinking densities, have larger hydrodynamic radii and sparser distributions in the

hydrogel, which resulted in lower G' values among all hydrogels **(Figure 3-4C)**. Conversely, MP6 and MP9 have a greater G' than Org- and C12-MP3 because of the greater crosslinking density and smaller hydrodynamic radii, which leads to the formation of a dense hydrogel **(Figure 3-4C)**. However, no significant increase was confirmed between the G' of the Org-MP6 and Org-MP9 hydrogels, indicating that the difference

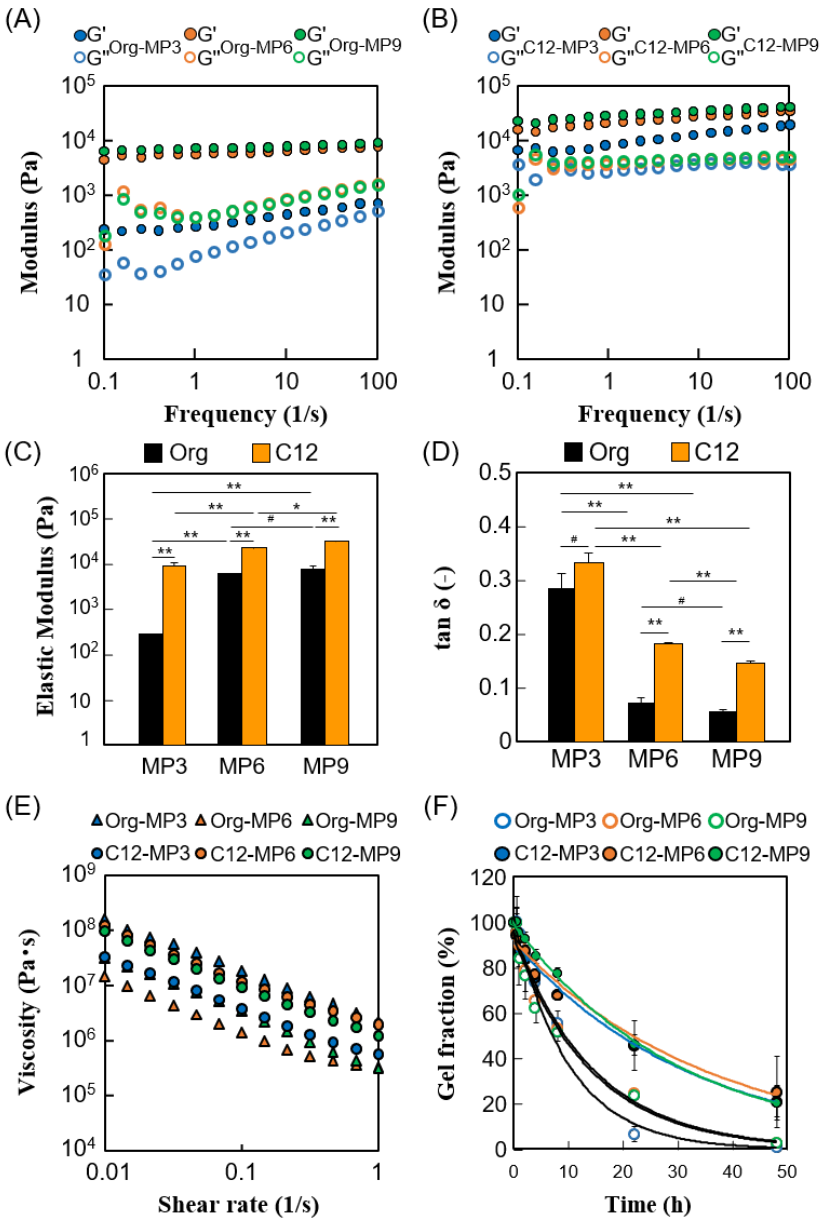

Figure 3-4. Physicochemical properties of MP hydrogels [126].

Storage (G′) and loss (G″) moduli of the (A) Org- and (B) C12-MP hydrogels with 3–9h of thermal crosslinking measured by frequency sweep rheometry. (C), (D) Comparison of the elastic modulus and tan δ at 1Hz taken from the rheometry of the Org- and C12-MP hydrogels. (E) Shear-thinning properties of the MP hydrogels. (F) Enzymatic degradation profile of the Org- and C12-MP hydrogels with different crosslinking times.

in the crosslinking ratio between Org-MP6 and Org-MP9 did not significantly affect their G' values. By comparing the Org- and C12-MP hydrogels, the G' of the C12-MP hydrogels was significantly higher than that of Org-MP hydrogels among all crosslinking times **(Figure 3-4C)**. These results were due to the increased interaction between C12-MPs caused by the dodecyl group modification in C12-ApGltn. On the other hand, we also evaluated tan δ, which is the ratio of G'' to G', to evaluate the viscous or elastic features of the MP hydrogels. **Figure 3-4D** shows that the significantly higher tan δ values of the Org- and C12-MP3 hydrogels were confirmed. These results indicated that the Org- and C12-MP3 hydrogels dissipated the loaded oscillation stress and behaved like viscous materials due to the large hydrodynamic radius and sparse distribution in hydrogels. Org- and C12-MP6 as well as Org- and C12-MP9 hydrogels had lower tan δ values compared with the respective MP3 hydrogels, indicating that they formed packed structures, presumably due to their smaller hydrodynamic diameters, and behaved like elastic materials. However, the tan δ values of C12-MP6 and C12-MP9 were significantly higher than those of Org-MP6 and Org-MP9, respectively. Hydrated Org-MPs tend to interact with other MPs, and the hydrogel as a whole behaves like a chemically crosslinked hydrogel. However, C12-MPs had a lower tendency of hydration because of their higher hydrophobicity and formed a denser packing structure compared with Org-MPs, resulting in the dissipation of loaded force by deforming the packing structure of C12-MPs.

Alternatively, the shear-thinning properties of the Org- and C12-MP hydrogels were evaluated using a rotational rheometer. **Figure 3-4E** indicates that the viscosity of the Org- and C12-MP hydrogels decreased with increasing shear rate, indicating that those hydrogels could be injected via syringe. Org- and C12-MP hydrogels were assumed to form aggregates in particle suspensions by hydrophobic interactions between particles. When the shear stress was loaded onto the hydrogels, those interactions could not tolerate the shear stress, and the particle aggregation eventually deformed [139]. Therefore, the Org- and C12-MP hydrogels had

shear-thinning behavior and were injectable through a 21-gauge needle **(Figure 3-1B)**.

3.3.5. Degradation profile of the Org- and C12-MP hydrogels

To evaluate the effects of the hydrophobic group in C12-ApGltn and the crosslinking time on the degradation rate, MP hydrogels were immersed in a collagenase solution for up to 48 h. The degradation rate of the C12-MP hydrogels was slower than that of the Org-MP hydrogels across all crosslinking times **(Figure 3-4F)**. This result was likely due to the greater interparticle interactions of the C12-MP hydrogels than that of the Org-MP hydrogels because of the additional physical crosslinking by the dodecyl group in C12-ApGltn that suppressed penetration of the collagenase solution into the C12-MP hydrogel matrix. Alternatively, the gel fraction of the Org-MP3 hydrogel remained at only 7% after incubation for 24 h, whereas that of the Org-MP6 and Org-MP9 hydrogels was greater than 20%. Additionally, the gel fraction of the C12-MP9 hydrogel was greater than that of the C12-MP3 and C12-MP6 hydrogels by 8 h; however, no difference was confirmed among the C12-MP3, C12-MP6 and C12-MP9 hydrogels after 24 h. These results indicate that a longer crosslinking time tends to enhance the degradation resistance because of the increased covalent crosslinking density. The degradation rate of the C12-MP hydrogels was, however, affected by hydrophobic modification and crosslinking time. The half-life of Org- and C12-MP hydrogels was also calculated by using the approximate curves in each plot (Table 1). The Org-MP3 hydrogel had the shortest half-life in the collagenase solution among all the groups. The half-lives of the Org-MP6 and Org-MP9 hydrogels were approximately 2 h longer than that of the Org-MP3 hydrogel; however, C12-MP hydrogels had half-lives that were two times longer, indicating that the C12-MP hydrogels were more stable in a physiological environment.

3.3.6. Cellular response to the Org- and C12-MP hydrogels

To evaluate the effects of the MPs on cell viability and angiogenic properties, MPs were cultured with

RAW264 cells at low MP concentrations that did not aggregate. The average viabilities of RAW264 cells cultured with Org- and C12-MPs are shown in **Figure A-7**. Org-MP3, Org-MP6 and Org-MP9 showed enhanced cell viability compared with the tissue culture polystyrene (TCPS) control. Gelatin contains the Arg-Gly-Asp (RGD) sequence, which is recognized by cell integrins and promotes cell attachment and viability [140,141]. Therefore, RAW264 cells recognized the RGD sequences of the degraded Org-ApGltn molecules and the surface of Org-MP, which led to greater viability than the TCPS control. Although C12-MP3 at 0.05 w/v% showed a similar effect as Org-MP3 on the viability, a higher concentration of C12-MP3 induced inhibitory effects on the cell viability. C12-MP6 and C12-MP9 at all concentrations had higher inhibitory effects on cell viability than C12-MP3 because the former MPs did not degrade during culture, and the hydrophobic moieties deposited on the C12-MP surface affected those effects. Moreover, C12-MP6 and C12-MP9 are considered to be more frequently internalized in RAW264 cells because of their smaller size [142], which is attributed to the hydrophobic modification and longer crosslinking time [143]. Therefore, C12-MP6 and C12-MP9 increased the concentration of the hydrophobic moieties in the cells, which led to cytotoxicity.

The amounts of secreted VEGF and TNF-α from RAW264 cells cultured with Org- and C12-MPs were also evaluated. As shown in **Figure 3-5A**, C12-MP3, C12-MP6 and C12-MP9 stimulated VEGF secretion at concentrations of 5.47, 15.3 and 36.8 pg/mL, respectively, and a significant increase with increasing crosslinking time was confirmed. LPS at 10 ng/ml induced 143 μL of VEGF secretion, which was more than 3.8 times greater than that induced by C12-MPs **(Figure 3-5A)**. The TCPS control and Org-MPs did not stimulate VEGF secretion from RAW264 cells. C12-MPs also promoted the secretion of TNF-α compared with TCPS and Org-MPs **(Figure 3-5B)**. The longer crosslinking time of the C12-MPs tended to induce higher levels of VEGF and TNF-α expression because the longer crosslinking time of these MPs retained the particle shape and higher concentration of the dodecyl group on the surface of the C12-MPs during cell culture, leading

to a greater interaction of the dodecyl group with cells. To evaluate the stimulation pathways of the enhanced secretion of VEGF and TNF-α, RAW264 cells were pretreated with VIPER, the TLR4 inhibitor peptide, before the addition of C12-MPs and LPS. VIPER successfully suppressed the secretion of VEGF and TNF-α from RAW264 cells stimulated with C12-MPs and LPS **(Figure 3-5C, D)**. These results indicated that the C12-MP is a TLR4 ligand and stimulates downstream pathways, including the myeloid differentiation primary response protein (MyD) 88-TIR domain-containing adaptor protein (TIRAP)-dependent pathway [101,102,104]. NF-κB, the promoter of VEGF and the TNF-α gene [102], was then activated, which enhances VEGF and TNF-α secretion.

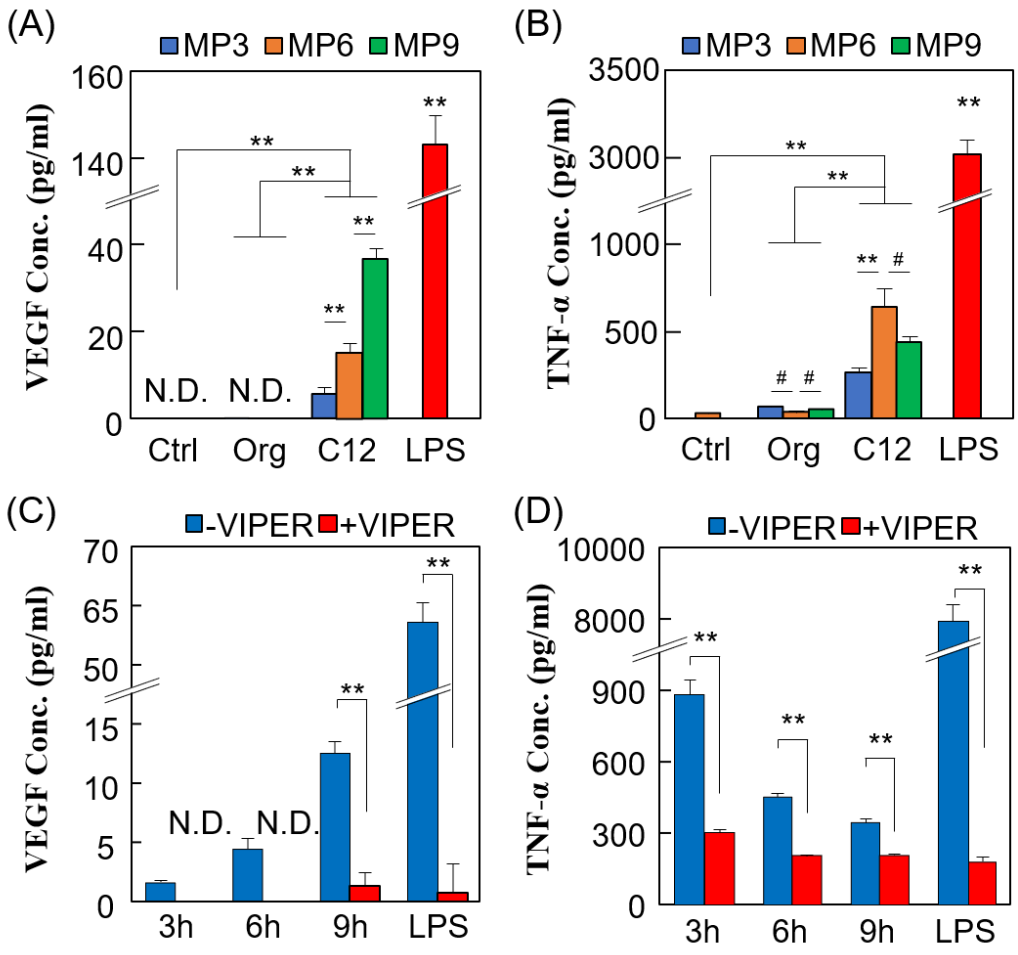

Figure 3-5. In vitro angiogenic and inflammatory responses to MPs [126].
Quantification of the secreted amounts of (A) VEGF and (B) TNF-α by ELISA when cells were cultured with Org-MPs and C12-MPs. The secreted amounts of (C) VEGF and (D) TNF-α stimulated by C12-MPs when the TLR4 receptor was inhibited by VIPER, a TLR4 blocking peptide. *p < 0.5, **p < 0.01, #p > 0.05.

3.3.7. *In vivo tissue responses to C12-MPs*

To evaluate the in vivo angiogenic properties of C12-MPs, we employed hairless mice and observed the blood flow and histological responses. **Figure 3-6A** shows blood perfusion images of the PBS, Org-MP and C12-MP hydrogels at the injection site taken with an LDPI system for up to 22 days. PBS and Org-MP hydrogels showed no increased blood flow for up to 22 days, whereas the C12-MP3 hydrogel induced significantly higher blood perfusion on day 2 compared with not only PBS and Org-MPs but also the C12-MP6 and C12-MP9 hydrogels **(Figure 3-6B)**. Alternatively, the blood flow around the C12-MP3 hydrogels decreased by day 7, returning to normal blood flow. The C12-MP6 hydrogel showed significantly higher blood flow from days 7 to 15, followed by a decrease that was not significant compared with PBS and Org-MP hydrogels at day 22. On the other hand, the C12-MP9 hydrogel induced significantly higher blood flow from days 15 to 22 compared with all the other groups. The time course of the increased blood flow was dependent

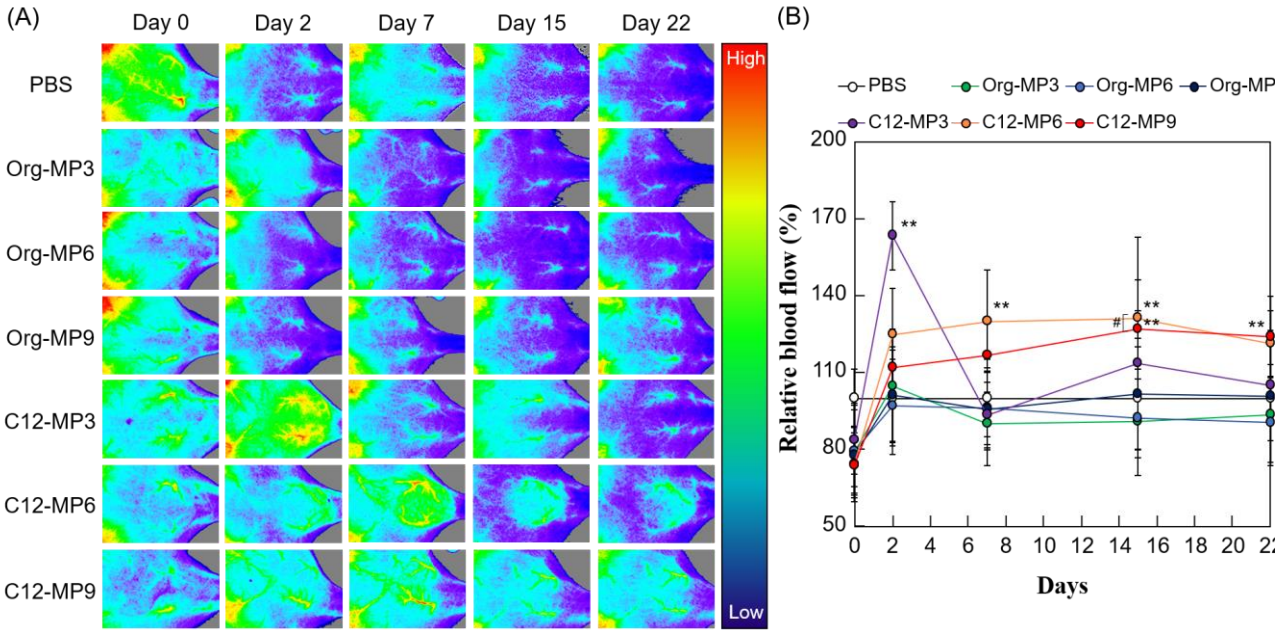

Figure 3-6. In vivo quantitative analysis of angiogenesis by LDPI [126].
(A) Laser Doppler perfusion images of mouse backs after implantation of the Org- and C12-MP hydrogels. The image hues indicate the intensity of the blood perfusion: red and blue indicate higher and lower perfusion, respectively. (B) Quantification of the blood flow from the LDPI images up to 22 days. The blood flow of the PBS-injected mice each day was defined as 100%. * and ** indicate significant differences (*$p < 0.05$ and **$p < 0.01$, respectively). No symbol or # indicates no significant difference (#$p > 0.05$).

on the thermal crosslinking time. The C12-MP3 hydrogel was quickly degraded after injection, and the C12-ApGltn polymer increased around the injection site to promote angiogenesis, similar to our previous study [119]. Angiogenesis then decreased with enzymatic degradation and dispersion of the C12-MP3 hydrogel, and the blood flow also became equal to that of PBS and the Org-MP hydrogel injection. Alternatively, the C12-MP6 and C12-MP9 hydrogels maintained a high level of blood flow for up to 22 days due to the slow degradation rate, sustaining a high concentration of the C12-ApGltn molecule at the injection site. To evaluate the tissue responses on the C12-MP hydrogel, we also observed tissue sections of the Org-MP3 and C12-MP3 hydrogels on day 2 to quantify the degree of inflammation and angiogenesis **(Figure 3-7A)**. The stained area of NF-κB, the inflammation marker and promoter of the VEGF gene, increased to a greater extent after C12-MP3 hydrogel injection compared with PBS and Org-MP3 **(Figure 3-7B)**. Moreover, the stained area of CD31, an endothelial cell marker, was also significantly higher in the C12-MP3 hydrogel than in the PBS and Org-MP3 hydrogels, which indicates that the number of blood vessels increased around the C12-MP3 hydrogel injection site **(Figure 3-7A, C)**. Aoki *et al*. reported that poly(lactic-co-glycolic acid) (PLGA) nanosheets loaded with 250 ng of fibroblast growth factor (bFGF) induced angiogenesis in vivo [144]. The CD31 stained areas in tissue sections from the sham operation and unloaded PLGA nanosheets were comparable with our PBS and Org-MP3 hydrogel groups, respectively. However, the CD31-stained area around the C12-MP3 hydrogel was approximately 1.7-fold greater than that of the bFGF-loaded PLGA nanosheet, indicating that the estimated efficacy of the C12-MP3 hydrogel was at least comparable to 250 ng of bFGF. Additionally, the red blood cells inside the blood vessels were confirmed from the tissue sections stained with H&E **(Figure 3-7A)**. The C12-MP3 hydrogel promoted angiogenesis around the injection site by inducing NF-κB. In addition, MPO staining revealed that the accumulation of granulocytes around the C12-MP3 hydrogel increased because of the enhanced secretion of inflammatory cytokine signaling through NF-κB **(Figure 3-7A)**. On the other hand, cell

infiltration into Org- and C12-MP3 hydrogels was confirmed in MPO-stained sections, indicating that Org- and C12-MP3 did not have severe cytotoxicity. Based on the in vitro experimental results that indicated that C12-ApGltn stimulated TLR4-mediated VEGF secretion from RAW264 cells, C12-MP3 was considered to stimulate the TLR4-mediated pathway followed by increased secretion of NF-κB in vivo. Therefore, the proposed mechanisms of angiogenesis by the C12-MP hydrogel are: (1) binding of the C12-ApGltn molecule degraded from C12-MP on TLR4 in macrophages and activation of NF-κB; (2) enhanced secretion of VEGF by the activated NF-κB pathway; and (3) proliferation of endothelial cells by secreted VEGF, followed by blood perfusion **(Figure 3-8)**. Enhanced long-term angiogenesis could be beneficial for cell transplantation;

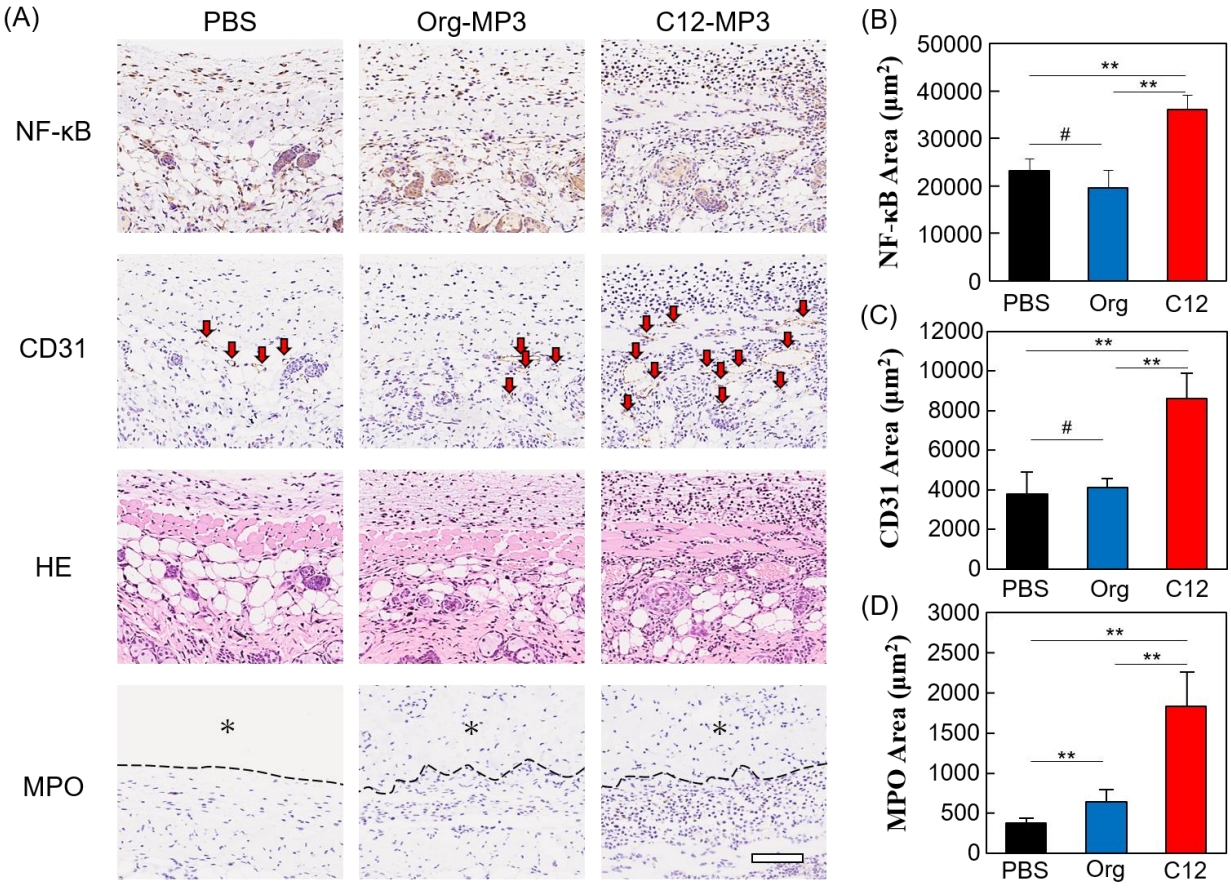

Figure 3-7. Immunohistochemical evaluations of angiogenesis [126]**.**

(A) Histological studies of tissues 2 days after implantation of the Org- and C12-MP3 hydrogels. The red arrows indicate blood vessels from CD31 staining. * and dashed lines in the MPO staining indicate MP hydrogels and the boundaries of the MP hydrogels and tissues. Active areas of NF-kB, CD31, and MPO were quantified using ImageJ and are shown in (B)–(D), respectively. #$p > 0.05$, **$p < 0.01$. scale bar = 50 μm.

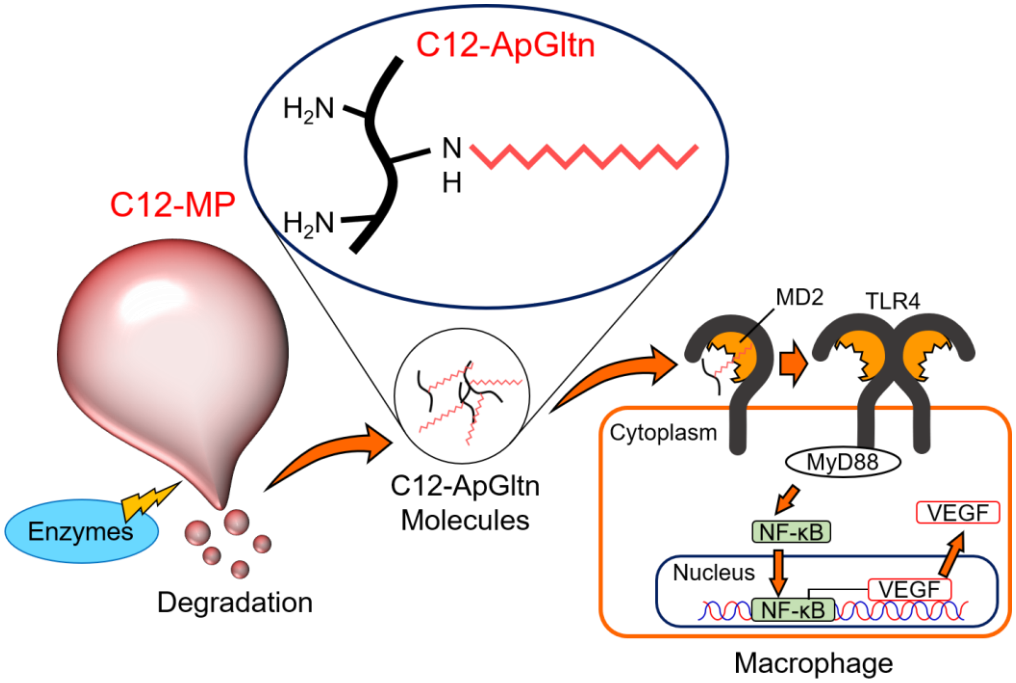

Figure 3-8. Proposed mechanisms of angiogenesis by the C12-MP hydrogels [126].

however, angiogenesis based on C12-MP hydrogels is accompanied by a weak inflammatory response and the secretion of inflammatory cytokines. Therefore, long-term secretion of inflammatory cytokines stimulated by C12-MP6 and C12-MP9 hydrogels may provoke the recruitment of fibroblasts and their proliferation, resulting in the formation of fibrous tissue near the injection site [145]. Hence, finding an optimal time point for cell transplantation by observing the time course of angiogenic and inflammatory responses stimulated by the C12-MP hydrogel is considered to be a clue for medical applications. Moreover, a combination of C12-MPs and anti-inflammatory drugs or materials to achieve a balance between inflammation and anti-inflammation may induce the recruitment of pericytes and the stabilization of newly formed blood vessels, leading to long-term stabilized angiogenesis [146].

3.4. Conclusion

To achieve drug- and growth factor-free angiogenesis, we developed a C12-MP hydrogel that stimulates endogenous VEGF secretion and angiogenesis. C12-MPs stimulated the TLR4-mediated pathway

and VEGF secretion in an in vitro study using the TLR4 blocking peptide. Moreover, the C12-MP hydrogel induced increased blood perfusion and the stained areas of NF-κB, CD31, and MPO at the injection site. These results demonstrate that the C12-MP hydrogel is a potential material the construction of vascular beads to improve the survivability of implanted cells or tissues.

CHAPTER 4: A hydrophobic Gelatin Fiber Sheet Promotes Secretion of Endogenous Vascular Endothelial Growth Factor and Stimulates Angiogenesis

4.1. Introduction

Tissue engineering and regenerative medicine is a promising approach to repair or replace damaged tissues and organs. Clinical studies in this field are mainly based on injecting cell suspensions or transplanting engineered tissues at a target site, where they are expected to serve as a substitute for the damaged tissue. However, the survivability of implanted cells and tissues is low because the supply of oxygen and nutrients via native blood vessels is insufficient[29,147]. To overcome these challenges, vascular beds can be used to enhance the survivability and function of implanted cells or tissues[30,32,33].

Biomaterials researchers have developed various angiogenic materials by incorporating growth factors (GFs), such as vascular endothelial growth factor (VEGF), basic fibroblast growth factor (bFGF), and stromal cell-derived factor (SDF)-1, in hydrogels[94,148,149], particles[150,151], and porous scaffolds[152,153]. The sustained release of GFs from these materials promotes angiogenesis *in vitro* and *in vivo* as well as wound healing[154–156], regeneration in an infarcted heart[157], and survivability of implanted islets[95]. However, GFs are easily inactivated under physiological conditions, compromising their bioactivity[52,54,55,158].

On the other hand, Kanno *et al.* reported that inoculation with *Pseudomonas aeruginosa*, a gram-negative bacterium, promotes re-epithelialization and angiogenesis by attracting neutrophils to the wound site[12].

However, the bacteria proliferate rapidly, leading to an unstoppable cytokine storm and sepsis. These inflammatory response and angiogenesis are caused by lipopolysaccharide (LPS), a constituent of the cell wall of gram-negative bacteria. Besides, saturated fatty acids (SFAs), a partial structure of LPS, promote the secretion of inflammatory cytokines and growth factors from inflammatory cells *via* the Toll-like receptor (TLR) 4-mediated pathway[101,104,106–109]. We previously reported that SFA-modified Alaska-pollock-derived gelatin (ApGltn), self-assembles into a hydrogel when hydrated with phosphate-buffered saline (PBS) and stimulated VEGF secretion and angiogenesis *in vitro* and *in vivo*[119]. However, the SFA-ApGltn hydrogels could not maintain their shapes under physiological conditions as they are vulnerable to enzymatic degradation. Chemical[159,160], enzymatic[161], and physical[162,163] methods have been used to make gelatin-based materials resistant to enzymatic degradation *in vivo*[164]. However, in the case of electrospinning, it is difficult to attain homogenous crosslinking and remove residual crosslinker and byproducts with chemical and enzymatic methods. Therefore, we utilized a physical method, thermal crosslinking, to fabricate electrospun microfiber sheets because of its simplicity and the ability to control the crosslinking density by changing the heating time[163,165–167].

In the present study, we used a hexadecyl group (C16) as an immune activator[109] to synthesize C16-modified ApGltn (C16-ApGltn), then used electrospinning to fabricated C16-ApGltn-based fiber sheets (C16-FSs) then thermally crosslinked to increase the crosslinking density and enhance their stability. The physicochemical properties of the C16-FSs with different crosslinking densities were evaluated in terms of the water contact angle, swelling ratio, and degradation rate. Moreover, the *in vivo* angiogenic properties of the C16-FSs in rats were quantified by laser doppler perfusion imaging (LDPI) and immunohistochemical staining.

4.2. Experimental

4.2.1. Materials

ApGltn (molecular weight = 33,000 g/mol) was purchased by Nitta Gelatin (Osaka, Japan). Hexadecanal was purchased from Tokyo Chemical Industry (Tokyo, Japan). 2-Picoline borane (pic-BH_3) was purchased from Junsei Chemical (Tokyo, Japan). Collagenase and Dulbecco's PBS were from Nacalai Tesque (Kyoto, Japan). 2,4,6-trinitrobenzensulfonic acid (TNBS), triethylamine, 2-aminoethanol, ethanol, dimethyl sulfoxide (DMSO), and 10% formalin neutral buffer solution were purchased from Wako Pure Chemical Industries (Osaka, Japan).

4.2.2. Synthesis of C16-ApGltn

Before the modification ApGltn with hexadecyl groups, the amino group concentration in the gelatin was quantified by the TNBS method, as previously reported[112,115,127]. Briefly, 100 μL of 0.1 w/v% ApGltn dissolved in 1:1 DMSO/H_2O was dispensed into each well of a 48-well plate. 100 μL of a solution of 0.1% TNBS and 0.1% triethylamine in 1:1 DMSO/H_2O was then added to each well. The plate was then shaken for 1 min using a microplate shaker and incubated or 2 h at 37°C. Then, the absorbance at 335 nm in each well was measured with a microplate reader (Spark 10M; Tecan, Männedorf, Switzerland) to calculate the number of amino groups. 2-aminoethanol (which has a known concentration of amino groups) was used instead of ApGltn to generate a calibration curve.

C16-ApGltn was synthesized by reductive amination[117,129,168] as described previously[112] **(Figure A-8)**. Briefly, 20 w/v% ApGltn was dispersed in a 30% ethanol aqueous solution and dissolved by heating at 50°C. Hexadecanal and 2-picoline borane were dissolved in ethanol and added to the ApGltn solution in 1.5-fold molar excesses relative to the remaining amino groups in the ApGltn. The reaction was carried out for 18 h. The reaction solution was then added dropwise to cold ethanol (10 times the reaction solution volume) to

precipitate the C16-ApGltn, which was then isolated by suction filtration using a glass filter. The C16-ApGltn was then re-dispersed in ethanol three times to remove remaining the hexadecanal and 2-picoline borane. The C16-ApGltn precipitate was finally vacuum-dried at 25°C, yielding a white powder. Unmodified ApGltn (Org-ApGltn) was prepared by the same protocol used for C16-ApGltn without the addition of hexadecanal and 2-picoline borane. The modification ratio of hexadecyl groups in C16-ApGltn was quantified using the TNBS method and comparing the absorbance at 335 nm with that of Org-ApGltn. The degree of modification was further confirmed by ^{1}H nuclear magnetic resonance (^{1}H-NMR) (JNM-AL300; JEOL, Tokyo, Japan).

4.2.3. Fabrication and Characterizations of C16-FS

Microfiber sheets were fabricated by electrospinning the gelatin solution. Briefly, Org-ApGltn was dissolved in a 40% aqueous ethanol solution at 30 w/v%, and C16-ApGltn was dissolved in a 50% EtOH aqueous solution at 15 w/v%. Electrospinning was conducted using a NANON-03 instrument (MECC, Japan) at room temperature (25 ° C) **(Figure 4-1A)**. Org- and C16-ApGltn solutions were extruded from an 18G needle at a feed rate of 1 ml/h with voltages of 20 and 25 kV, respectively. The obtained Org-FS and C16-FS

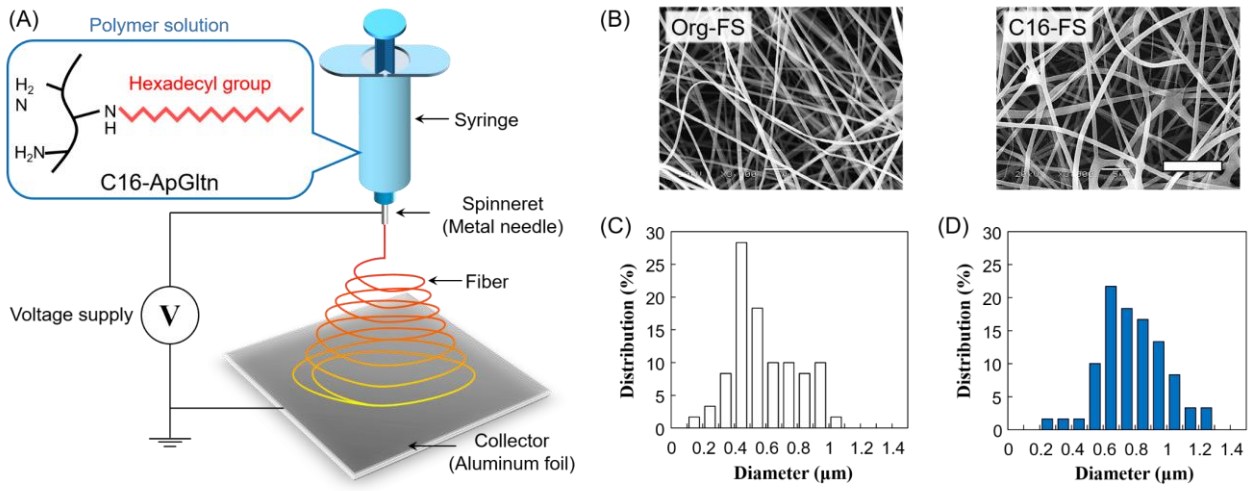

Figure 4-1. Fabrication and characterization of electrospun fiber sheets [169]**.**
(A) Electrospinning of C16-ApGltn into a fiber sheet (FS). (B) SEM images of FSs (scale bar = 10 μm). (C–D) Histograms of the fiber diameters in (C) Org-FS and (D) C16-FS, as quantified using Image J (n=60).

were observed with a scanning electron microscope (SEM) (S-4800 ultrahigh-resolution SEM, HITACHI, Japan), and the fiber diameters were measured using Image J software (n = 60). Fourier transform infrared spectroscopy (FT-IR) (ALPHA II; Bruker Corp., Billerica, MA, USA) was conducted on a C16-FS to confirm the presence of hexadecyl groups. Fiber sheets were then thermally crosslinked in a vacuum oven at 150°C for 4 h to improve their degradation resistance.

4.2.4. Water Contact Angle Measurements

To evaluate the hydrophobicity of the fiber sheets, water contact angle measurements were conducted using a DropMaster DM-701 (Kyowa Interface Science, Japan). Contact angle measurement was initiated 0.5 s after a 3 μL PBS droplet was dropped on the fiber sheet and continued for up to 15 s. The surface contact angle of the PBS droplet on the fiber sheet was then analyzed using FAMAS software.

4.2.5. Swelling Ratio

After 4 h of thermal crosslinking, fiber sheets were cut into 10 mm-diameter circles, each of which was weighed to determine the dry weight (W_d). Fiber sheets were then immersed in PBS at 37°C for up to 1,440 min. The swollen fiber sheets were weighed at each time point to determine the swollen weight (W_s). Hence, the swelling ratio of each sheet was calculated using the following equation:

$$\text{Swelling ratio} = \frac{W_s - W_d}{W_d}$$

4.2.6. Enzymatic Degradation of C16-FS

The enzymatic degradation of Org-FS and C16-FS was evaluated using collagenase. Briefly, after 4 h of thermal crosslinking, Org-FS and C16-FS were cut into 10 mm-diameter circles and immersed in PBS at

37°C for 1 h for pre-swelling. The swollen FSs were then immersed in a solution of 5 U/ml collagenase in PBS and incubated at 37°C for up to 240 min. The FSs were weighed at each time point to determine the degradation profiles.

4.2.7. Evaluation of Angiogenesis in Mice

Animal experiments were approved by the Animal Care and Use Committee of National Institute for Material Science (NIMS), Japan, and were performed in accordance with NIMS Regulations Pertaining to Animal Testing. To evaluate the angiogenic properties of C16-FS, the FSs were implanted subcutaneously in mice backs and evaluated by blood flow imaging and histological observation. Thermally crosslinked Org-FS and C16-FS were cut into 10 mm-diameter circles. A total of 24 hairless mice (Hos:HR-1, female, 4 weeks old; Hoshino Laboratory Animals, Japan) were anesthetized by isoflurane inhalation. An incision was made in the back of each mouse, the FS was implanted, and the incision was sutured closed. Sham surgery was also conducted by making an incision and then sutured without implanting FSs. The FSs were implanted near the mice's tail roots to avoid the blood flow instability caused by the movement associated with breathing.

The blood flows around the implant site was measured using an LDPI system (OZ-2, OMEGAWAVE, Japan) immediately after and 1, 2, 3, 7, 14, and 24 days after the implantation. To stabilize and control the blood flow rate in the mice for imaging, the isoflurane concentration was adjusted until each mouse's breathing rate was 1 breath/s. To analyze the mechanisms of angiogenesis *in vivo*, immunohistochemical staining was conducted on different mice from those used for the LDPI experiment. 3 days after the subcutaneous implantation of Org-FS and C16-FS, the mice were sacrificed using somnopentyl. The FSs and the surrounding tissue were dissected and fixed in a 10% formaldehyde neutral buffer solution. Tissue sections were stained with hematoxylin and eosin (H&E); nuclear factor-κB (NF-κB), VEGF, CD31, and myeloperoxidase (MPO)

were stained as markers of inflammation and angiogenesis. Stained areas of NF-κB, VEGF, and CD31 were quantified using Image J.

4.2.8. Statistical analysis

Data are shown as mean ± standard deviation (SD). Differences between groups were evaluated for statistical significance with the Student's t-test. Differences were considered statistically significant when $p < 0.05$.

4.3. Results and Discussion

4.3.1. Synthesis of C16-ApGltn

C16-ApGltn was synthesized by reacting the residual amino groups in ApGltn with hexadecanal followed by reduction with 2-picoline borane. The yields of Org- and C16-ApGltn were 90.2% and 82.0%, respectively (Table 4-1). The modification ratio of C16-ApGltn was 24.0 mol%, as measured by the TNBS method. The ^{1}H-NMR spectra shown in **Figure A-9** show peaks at 1.4 ppm in the C16-ApGltn spectrum, which correlates with a strong peak at the same chemical shift in the hexadecanal spectrum, confirming the substitution of hexadecyl groups into ApGltn.

4.3.2. FS Fabrication

The FT-IR spectra of the FSs **(Figure A-10)** show that the absorbance of C-H at 2853 and 2927 cm^{-1} was increased in the C16-FS spectrum compared with the Org-FS spectrum, which was attributed to the modification of the alkyl chains with hexadecyl groups in C16-ApGltn. Therefore, C16-ApGltn molecules but C16-FS were expected to be more hydrophobic than Org-ApGltn and Org-FS. Org-FS and C16-FS were fabricated by accumulating electrospun fibers into non-woven sheets. The mean thicknesses of Org-FS and C16-FS were 223 ± 17 μm and 276 ± 26 μm, respectively (Table 4-1). The SEM images of Org-FS and C16-

Table 4-1. Characterization of Org-FS and C16-FS [169].

Abbreviations	Sheet thickness (μm)	Fiber diameter (μm)
Org-FS	223 ± 17	0.58 ± 0.20
C16-FS	276 ± 26	0.78 ± 0.20

FS shown in **Figure 4-1B** show that the fibers were successfully formed and molded into a non-woven fabric-like structure. The mean fiber diameter of C16-FS (0.78 ± 0.20 μm) was larger than that of Org-FS (0.58 ± 0.20 μm), as measured from the SEM images. Histograms of the fiber diameters are shown in **Figure 4-1C** and D; these data show that over 70% of the fibers in the Org-FS were between 0.3 and 0.8 μm, whereas the same percent in the C16-FS were between 0.5 and 1.0 μm. After the thermal crosslinking, fiber diameters of Org- and C16-FS were 0.61 ± 0.13 μm and 0.72 ± 0.29 μm, respectively, which were not significantly different with that before crosslinking. Besides, fiber morphologies and histograms of Org- and C16-FS were quite similar to that before crosslinking **(Figure A-11)**. ApGltn has significantly lower sol-gel transition temperature (21.2 ° C) than porcine and bovine-derived gelatin (31.2°C) due to the lower content of proline and hydroxyproline, which contribute to forming the helical structure of gelatin [110,111]. Therefore, ApGltn in FSs was considered to have a random coil and amorphous structure because electrospinning was conducted at room temperature (25°C) [170]. The previous study reported that uncrosslinked and thermally-crosslinked gelatin fibers demonstrated similar dependence on elastic modulus and tan δ, which suggested that the thermally-crosslinked FSs retained amorphous structure [171].

4.3.3. FS Hydrophobicity

The surface contact angle on each FS was measured to evaluate the surface hydrophobicity, which may affect the water absorption rate. **Figure 4-2A** shows the behavior of PBS droplets on Org-FS and C16-FS. 0.5 s after dropping the PBS droplets, the surface contact angle of that on Org-FS was already smaller than that on C16-FS. The PBS droplets were then quickly absorbed into the Org-FS compared with the C16-FS. **Figure 4-2B** shows the rates of decrease in the contact angles of PBS droplets on Org-FS and C16-FS over 15 s. The surface contact angle was consistently higher on C16-FS than on Org-FS over 15 s because the modification of hexadecyl groups in C16-ApGltn resulted in higher hydrophobicity. Moreover, the hexadecyl

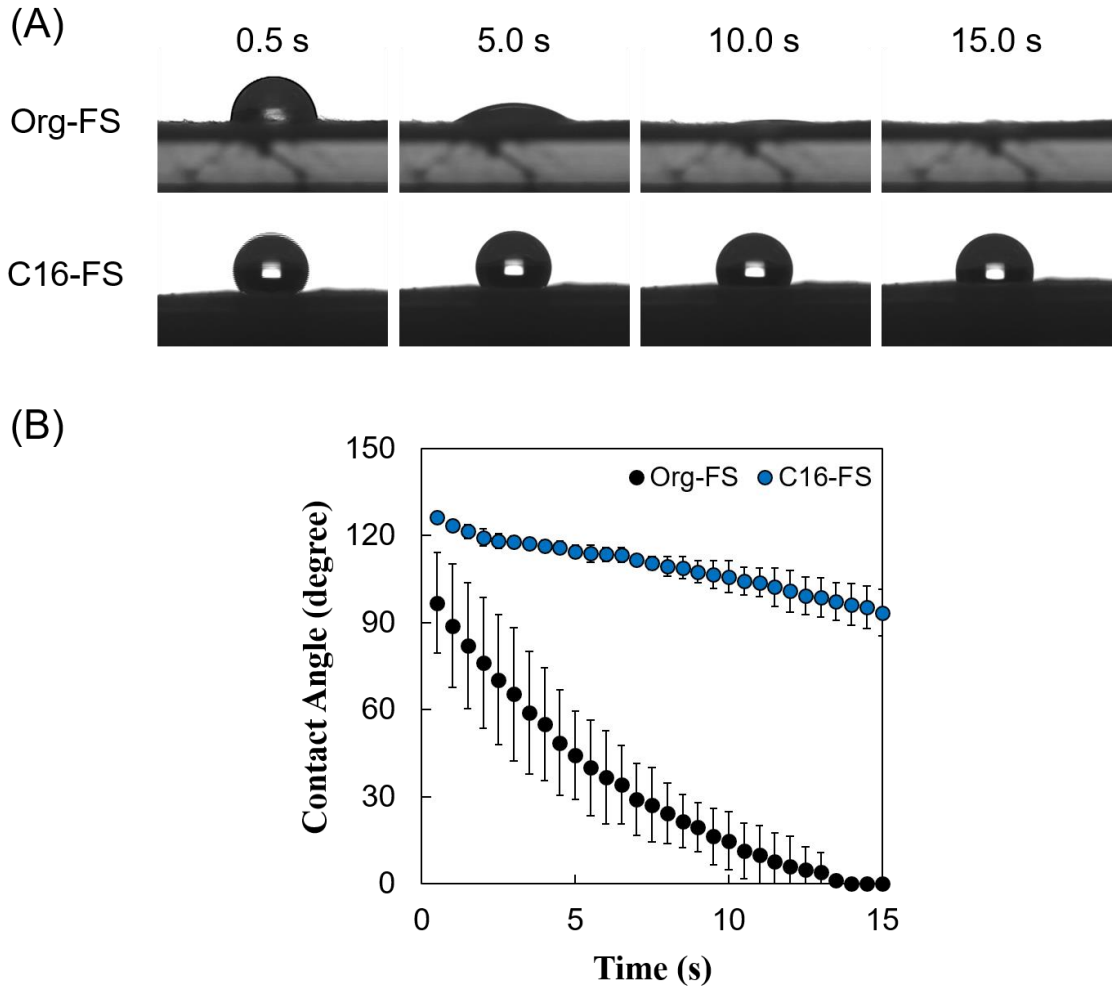

Figure 4-2. Surface contact angle measurements of Org-FS and C16-FS [169]**.**
(A) Representative images of the behavior of PBS droplets over 15 s on Org-FS and C16-FS after 4 h of thermal crosslinking. (B) Quantification of the decrease in the contact angle over time. Error bars represent SDs of each point (n = 3).

groups in C16-ApGltn were considered to be localized on the surface of the C16-FS because the FSs were fabricated in air, and hydrophobic molecules tend to move toward air-water interfaces[172]. We previously confirmed that hydrophobic groups conjugated to gelatin molecules tended to localize on the surfaces of thermally crosslinked microparticles by X-ray photoelectron spectroscopy[125]. Owing to this surface hydrophobicity, the C16-FS repelled PBS droplets and delayed their absorption into the FS.

4.3.4. Swelling Ratio

The swelling ratios of the FSs were measured to evaluate the effect of the hexadecyl groups in C16-FS on its stability in water **(Figure 4-3A)**. After immersing the FSs in PBS, they quickly absorbed PBS, as evidenced by significant weight gain in the 1 h of swelling. Both FSs then continued absorbing water and gaining weight over time, reaching steady states after 8 h. Although the swelling ratio of C16-FS was significantly lower than that of Org-FS for the first 2 h of swelling, no significant difference between them was observed after 4 h until 24 h. The swelling ratio basically depends on the crosslinking density in a polymer network; higher crosslinking densities result in less swelling, while lower crosslinking densities lead to

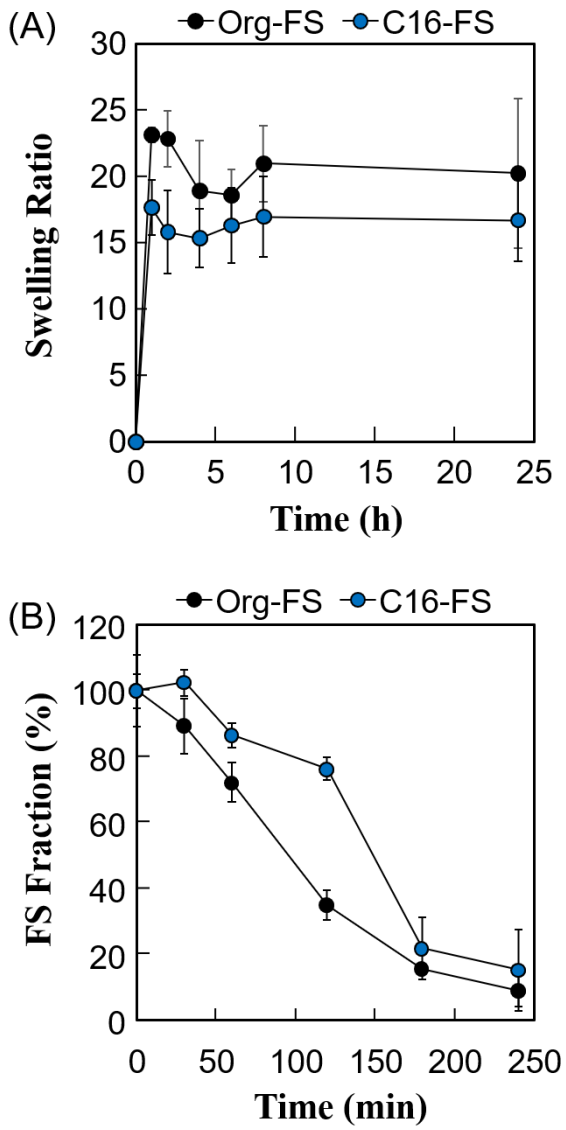

Figure 4-3. Physicochemical evaluations of FSs [169]. (A) Swelling ratios of Org-FS and C16-FS in PBS at 37°C (n = 5). (B) Enzymatic degradation rates of Org-FS and C16-FS. Error bars represent SDs of each point (n = 4).

increased swelling. However, the crosslinking density of C16-FS was considered to be lower than that of Org-FS due to the substitution of hexadecyl groups for amino groups, which contributes to amide bonding *via* dehydration condensation; this should lead to a higher swelling ratio in C16-FS. Therefore, the relatively swelling ratio of C16-FS despite its lower crosslinking density was attributed to physical crosslinking between hexadecyl groups (C16) in the C16-ApGltn molecules. We previously reported that the modification of hydrophobic groups in gelatin molecules contributes to decreased swelling ratios and increased mechanical strength in hydrogels, which is consistent with the results of the present study[39].

4.3.5. Enzymatic Degradation of FSs

The effect of the hexadecyl groups in C16-FS on degradation rate was evaluated by applying collagenase, an enzyme that cleaves peptide bonds in gelatin and collagen, and measuring the weight over time. Before the degradation test, Org-FS and C16- FSs were pre-swelled in PBS for 1 h. **Figure 4-3B** shows the degradation profiles of Org-FS and C16-FS in a collagenase solution. Results show that the weights of these FSs gradually decreased with time, and the weight of remaining C16-FS was higher than that of Org-FS after 120 min. These results were attributed to the suppressed swelling ratio of C16-FS for the first 2 h, which lead the delayed uptake of collagenase molecules into fibers. However, the weights of Org-FS and C16-FS were not significantly different after immersion in the collagenase solution for 180 min because both FSs broke into small fragments, leading to rapid degradation.

4.3.6. Angiogenesis Evaluation in vivo

The *in vivo* angiogenic properties of C16-FS were evaluated using LDPI and histological observations. **Figure 4-4A** shows that the LDPI results after subcutaneous FSs implantation in mice, followed by quantification of blood flow at the implantation site. There were no significant differences between the LDPI

images or blood flow in mice with Org-FS implanted, mice with C16-FS implanted, and control mice that received the sham operation (control) immediately after the implantation (Day 0), or on Day 1. However, on Day 3, the blood flow in the tissues around the C16-FS implantation site was increased, and visible blood vessels were observed, indicating an angiogenic response; however, the blood flow decreased after Day 3 until Day 24 **(Figure 4-4A)**. The quantitative analysis of blood flow over 24 days is shown in **Figure 4-4B**. The blood flow measured on each day was normalized to that of the sham group on the corresponding; thus, the

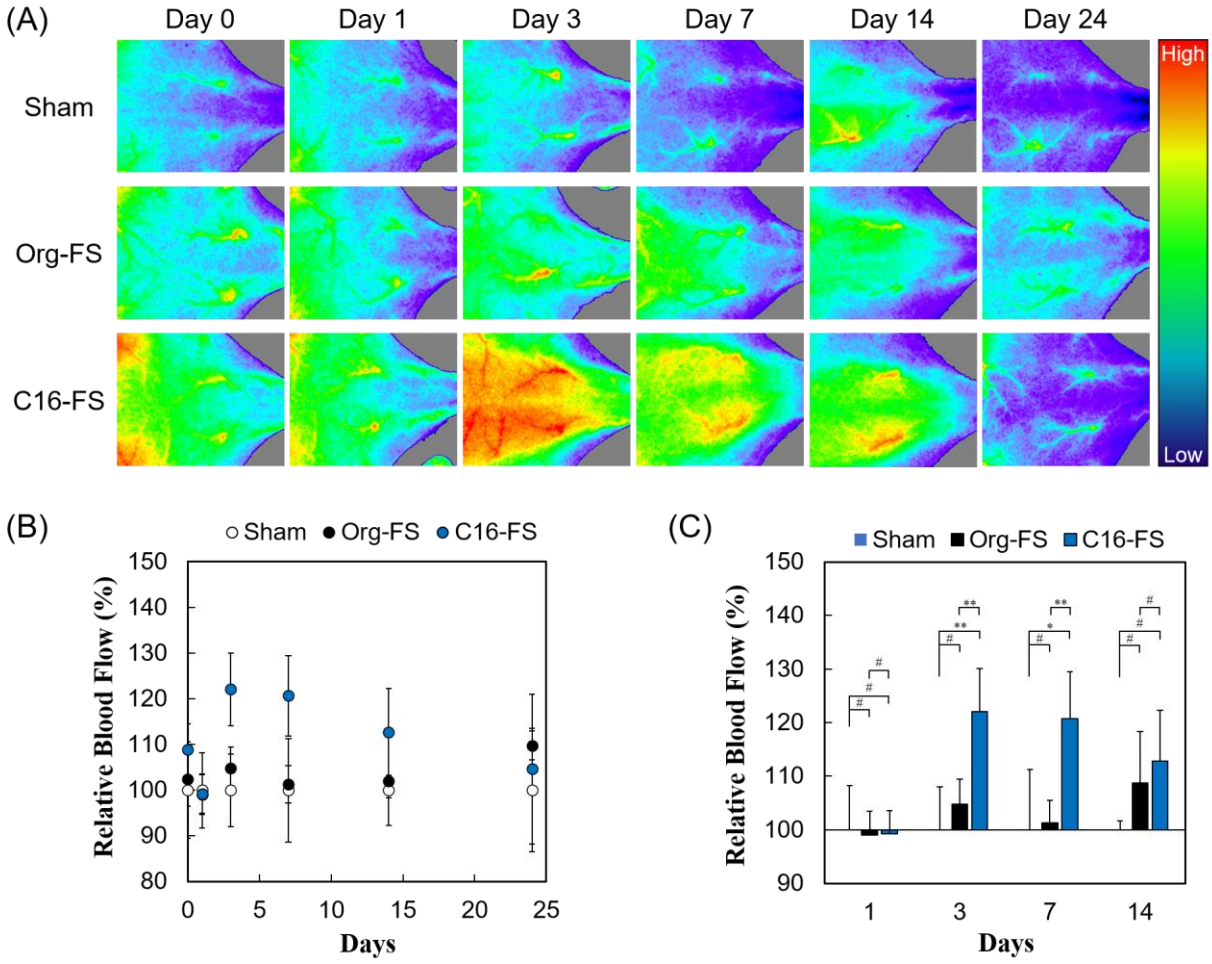

Figure 4-4. In vivo angiogenesis evaluations of C16-FS [169]**.**

(A) LDPI images of mice backs after the sham implantation and implantation of Org-FS or C16-FS. The hues in images indicate the intensity of blood perfusion: red and blue indicate higher and lower perfusion, respectively. (B) Blood flow over 24 days, as quantified from the LDPI images. The blood flow values were normalized to that in the mice treated with the sham operation (control) for each day. Error bars represent SDs of each point (n = 4–5). (C) Comparison of mean blood flows in different groups on each day (* indicates $p < 0.05$, ** indicates $p < 0.01$, and $^{\#}$ indicates $p > 0.05$).

sham group was used as a reference and consistently exhibited 100% blood flow. There was no statistically significant difference in the mice with Org-FS implanted compared with the sham group over 24 days. However, in the C16-FS group, the blood flow was elevated (122%) on Day 3 and sustained until Day 7, after which time it gradually decreased to 104% on Day 24. The time-dependent decrease in blood flow around the C16-FS was attributed to the ongoing enzymatic degradation of the C16-ApGltn molecules in the FS, as demonstrated in the *in vitro* degradation test **(Figure 4-3B)**. On Day 24, the blood flow in the C16-FS groups returned to an approximately normal level, and the C16-FS was considered to be almost completely degraded.

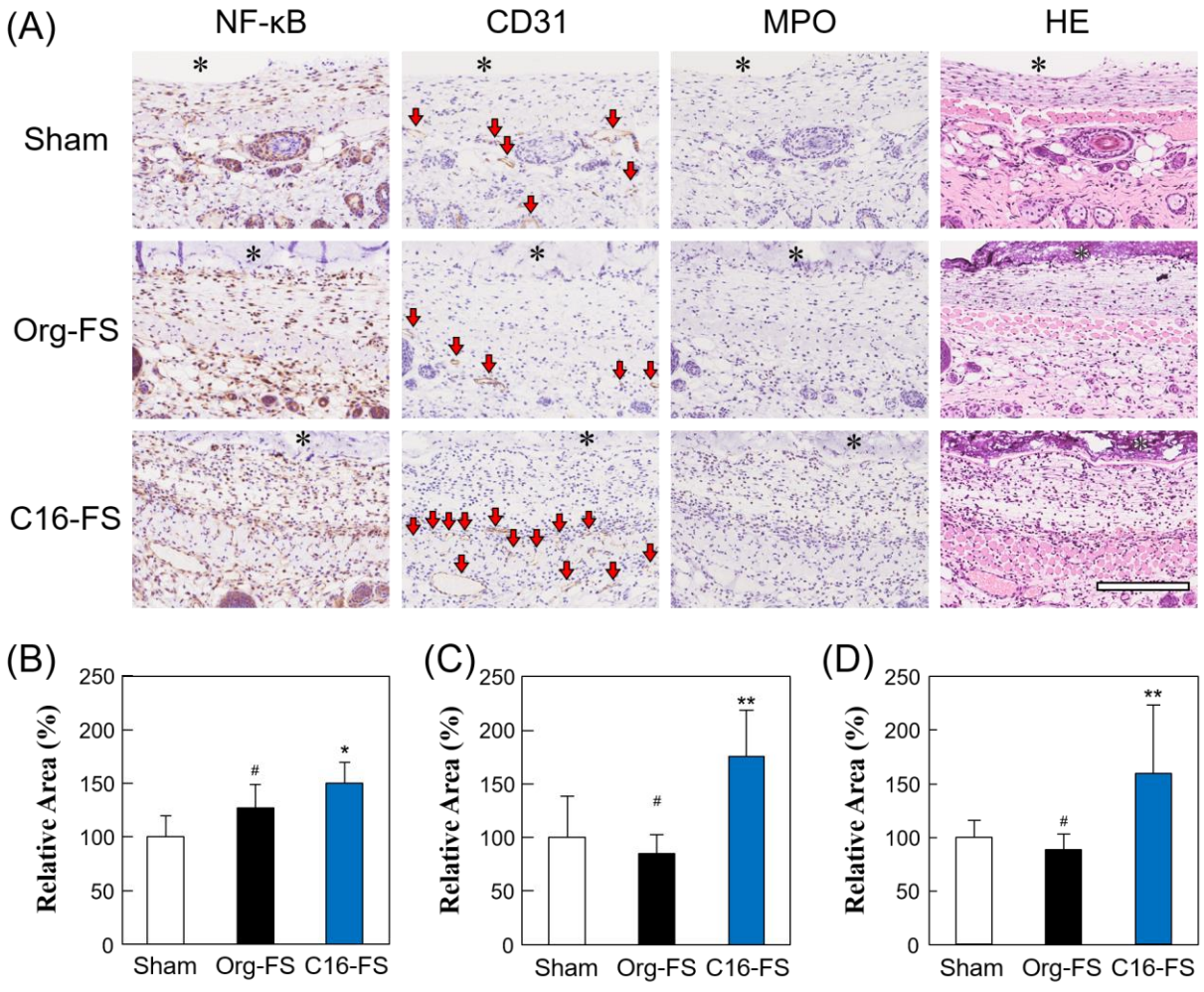

Figure 4-5. Evaluation of angiogenesis by immunohistochemical studies [169]**.**
(A) Immunohistochemical studies of FSs and surrounding tissues 3 days after the sham operation and implantation of Org-FS or C16-FS (* denotes the FS, and the red arrows in the CD31-stained tissue sections indicate blood vessels). (B–D) Active areas of NF-kB, CD31, and MPO, respectively, as quantified using Image J (* indicates $p < 0.05$, ** indicates $p < 0.01$, and $^{\#}$ indicates $p > 0.05$).

We also analyzed the difference in blood flow between groups at several time points **(Figure 4-4C)**. Although there was no statistically significant difference between the blood flows in the sham, Org-FS, and C16-FS groups on Day 1, C16-FS induced significantly higher blood flow on Day 3. Moreover, the C16-FS group sustained significantly higher blood flow up to Day 7 compared with the sham and Org-FS groups. However, the increased blood flow associated with C16-FS compared with Org-FS was no longer observed on Day 14. Comparing with the results of our previous study with an angiogenic self-assembled hydrogel[27], the C16-FS prepared with thermal crosslinking suppressed the subcutaneous spreading of material and successfully induced sustained localized angiogenesis for 14 days.

Figure 4-5A shows tissue sections with immunohistochemical staining of NF-κB, CD31, MPO, and HE. The area of NF-κB staining revealed significantly increased NF-κB expression in the tissue around the C16-FS **(Figure 4-5A, B)**. NF-κB promotes genes associated with inflammatory cytokines and growth factors, such as VEGF, and we have previously shown that SFA-modified gelatin stimulates NF-κB *via* TLR4-mediated pathways[27]. However, there were no statistically significant differences between the levels of VEGF staining in the Sham, Org-FS, and C16-FS implanted site, although the higher level of VEGF staining was confirmed inside of C16-FS compared with Org-FS **(Figure A-12)**. We previously reported an increased affinity of VEGF to hydrophobically-modified gelatin based on surface plasmon resonance measurements[97]. Therefore, VEGF was considered to be entrapped in the C16-FS by hydrophobic interactions between VEGF and the hexadecyl groups in C16-ApGltn, which results were correlated with the increased water contact angle of C16-FS. Furthermore, the level of the stained area of CD31, an endothelial marker, was elevated around the C16-FS implantation site compared with the sham and Org-FS **(Figure 4-5A, C)**. In addition, the number of blood vessels (indicated by red arrows in the CD31-stained sections) was higher in the C16-FS sample than in the Org-FS and sham samples, indicating that the C16-FS enhanced angiogenesis **(Figure 4-5A)**. The H&E

staining showed that there was blood perfusion inside of the newly formed blood vessels around C16-FS **(Figure 4-5A)**. We further investigated the accumulation of granulocytes (including monocytes, neutrophils, and macrophages) by MPO staining, as shown in **Figure 4-5A, D**. The observed increased accumulation of granulocytes around C16-FS was attributed to an increased foreign body reaction by the enhanced protein adsorption on C16-FS or a direct stimulation of inflammatory cells by hexadecyl groups.

In summary, C16-FS activated NF-κB secretion by stimulating TLR4-mediated pathways. NF-κB then activated the expression of VEGF, which became entrapped within the C16-FS and gradually released upon the degradation of C16-FS. The secreted VEGF promoted endothelial cell proliferation and, consequently, angiogenesis, which gave rise to increased blood perfusion **(Figure A-12)**. Based on these findings, it was concluded that C16-FS is a promising method to induce angiogenesis for prevascularization in cell or tissue transplantation without the addition of any growth factors. However, various types of inflammatory cytokines are secreted in response to VEGF, which is stimulated by NF-κB; the effects of those cytokines on implanted cells need to be further assessed in future studies. Moreover, long-term inflammation may lead to fibrosis[145], which would be a significant challenge for clinical application. Therefore, the incorporation of anti-inflammatory drugs may alleviate the inflammatory responses and modulate the balance of pro- and anti-inflammatory responses to lead the angiogenesis without fibrosis. The modification of cyclodextrin group in FSs enables not only the incorporation of anti-inflammatory drugs by forming inclusion complexes, but increased hydrophilicity, which prevents the adhesion of proteins on FSs in vivo followed by the foreign body reaction [173]. Furthermore, we are now investigating how changing the thermal crosslinking time may influence the time-dependent modulation of the angiogenic response elicited by C16-FS.

4.4. Conclusion

Here, we developed a C16-FS with thermal crosslinking to achieve sustained and localized angiogenesis *in vivo*. The C16-FS elicited a high-water contact angle and exhibited a lower water absorption rate, indicating increased hydrophobicity of the C16-FS compared with the Org-FS. In addition, the C16-FS was stable in PBS for 24 h due to the thermal crosslinking, but the C16-FS was degraded by collagenase in 4 h (as was the Org-FS). *In vivo* experiments followed by LDPI observations revealed that the C16-FS induced significantly higher blood perfusion when implanted subcutaneously in mice compared with the Org-FS. Moreover, C16-FS induced sustained and localized angiogenesis for up to 7 days, followed by a decrease in blood flow to a normal level after 24 days. Immunohistochemical evaluations revealed that C16-FS promoted NF-κB secretion, leading to VEGF secretion, which was entrapped within the C16-FS and released, resulting in elevated CD31 expression and angiogenesis with blood perfusion. These results demonstrate that the C16-FS is a promising material for making vascular beads to improve the survivability of implanted cells or tissues without the need for drugs or growth factors.

CHAPTER 5: Anti-Inflammatory and Tissue Adhesion Properties of an α-Linolenic Acid-modified Gelatin-based in situ Hydrogel

5.1. Introduction

Wound healing processes are always accompanied with inflammation to kill bacteria or enhance tissue regeneration. Although these remodeling processes are necessary for healing wounds, excess and chronic inflammation delays the healing processes and induces pain [60–62]. Deep burn injury in particular is accompanied by the stimulation of inflammatory responses including the activation of nuclear factor (NF)-κB and secretion of various inflammatory cytokines, followed by the production of reactive oxygen species (ROS), which leads to progressive tissue damage [65]. Rheumatoid arthritis, an autoimmune disorder, involves the progressive destruction of cartilage and bone in joints caused by accumulation of inflammatory cells and secretion of excess levels of inflammatory cytokines such as tumor necrosis factor (TNF)-α [174,175]. To address these inflammatory responses, drugs [72,176,177], proteins/peptides [178], and antibodies [71] have been incorporated into or conjugated to biomaterials. Anti-inflammatory drugs incorporated into micro/nano spheres [176] or hydrogels [177] have demonstrated significant reduction of inflammation in vivo; however, the rapid diffusion of these low-molecular weight drugs from biomaterials prevents these systems from exhibiting sustained anti-inflammatory effects [72]. The modification of proteins or antibodies is an alternative approach to suppressing inflammation by targeting cytokines or their receptors. A hydrogel functionalized with an inhibitory peptide of interleukin

(IL)-1β receptor significantly reduced cell death in the presence of various kinds of inflammatory cytokines [178]. In addition, use of an anti-TNF-α antibody modified hydrogel led to reduced accumulation of inflammatory cells around a burn injury site and secretion of IL-1β, followed by prevention of progressive tissue damage [178]. However, peptides and antibodies have short half-lives due to methionine oxidation under physiological conditions [73–76], leading to the rapid decrease of their efficacy. In the present study, we aimed to develop the naturally derived multifunctional biomaterials with anti-inflammatory and tissue sealing properties for clinical translations including treating severe wounds, burn, and inflammation related diseases.

Poly unsaturated fatty acids (PUFAs)—natural chemicals extracted from fish and nut oils—are another class of anti-inflammatory [179–181] and antioxidant [182,183] agents. Although both ω-3 and ω-6 PUFAs activate GPR120, a G-protein coupled receptor, and induce anti-inflammatory effects, these metabolites shows different inflammatory behaviors [179,184]. On the other hand, ω-3 PUFA-derived metabolites have anti-inflammatory properties, whereas ω-6 PUFA-derived metabolites demonstrate pro-inflammatory reactions and immunoreactive functions [184,185]. Besides, excess internalization of PUFAs and their oxidants induces cell cytotoxicity by inhibiting the mitochondrial respiratory system [186–188]. Therefore, in this study, ω-3 PUFA - modified Alaska pollock-derived gelatin (ApGltn) was synthesized to evaluate the cytotoxicity and anti-inflammatory properties when compared with unmodified PUFA and ApGltn molecules. We previously reported that hydrophobically-modified Alaska pollock-derived gelatin hydrogel demonstrated significantly higher bonding strength on tissue than a commercial fibrin adhesive, which suggests that ω-3 PUFA modified ApGltn-based hydrogel also exert tissue adhesion properties; however, the longer hydrophobic groups caused a decrease in the bonding strength on tissues due to the self-aggregation of modified gelatin molecules [112,189–191]. Therefore, we employed α-linolenic acid (ALA), the shortest chain length among natural ω-3 PUFAs, to synthesize ALA-modified ApGltn (ALA-ApGltn), which was thereby crosslinked with a poly(ethylene

glycol)-based crosslinker to develop ALA-ApGltn based hydrogel (ALA-gel). ALA-ApGltn and ALA-gel were evaluated on the physicochemical properties, anti-inflammatory effects, and tissue adhesion properties to assess the potential applications for various medical use.

5.2. Experimental

5.2.1. Materials

ApGltn (molecular weight = 33,000) was purchased from Nitta Gelatin (Osaka, Japan). Collagenase and Dulbecco's phosphate-buffered saline (PBS) were acquired from Nacalai Tesque (Kyoto, Japan). ALA, potassium persulfate, 2, 4, 6-trinitrobenzensulfonic acid (TNBS), triethylamine, 2-aminoethanol, ethanol, dimethyl sulfoxide (DMSO), and 4% paraformaldehyde phosphate buffer solution (PFA/PBS) were purchased from FUJIFILM Wako Pure Chemical (Osaka, Japan). 1-ethyl-3-(3-dimethylaminopropyl) carbodiimide (EDC) hydrochloride and 4',6-diamidino-2-phenylindole dihydrochloride (DAPI) were purchased from Dojindo Laboratories (Kumamoto, Japan). N-Hydroxysuccinimide (NHS), 2,2′-azino-bis(3-ethylbenzothiazoline-6-sulfonic acid) diammonium salt (ABTS), and phalloidin-tetramethylrhodamine B isothiocyanate (TRITC), MitoTracker Orange CMTMRos, CellROX Orange Reagent, and NucBlue Live ReadyProbes Reagent were purchased from Sigma-Aldrich (USA). Triton™ X-100 was purchased from Thermo Fisher Scientific (USA). Pentaerythritol poly(ethylene glycol) ether tetrasuccinimidyl glutarate (4S-PEG) with a molecular weight of 10,000 was purchased from NOF Corporation (Japan).

5.2.2. Synthesis of ALA-ApGltn

The primary amino groups in ApGltn were quantified using the TNBS method prior to synthesizing ALA-ApGltn according to our previous method [112,113,115,127]. Briefly, ApGltn was dissolved in 1:1 DMSO/H_2O at 0.1 w/v%. 100 μL of ApGltn solution was then mixed with 100 μL of 0.1% TNBS and 0.1% TEA in each

well of a 48-well plate followed by stirring using a plate shaker for 60 s. After 2 h of incubation at 37°C protected from light, the reaction was stopped by adding 50 µL of 6N HCl. To calculate the concentration of the primary amino groups in ApGltn, the absorption at 335 nm of each well was measured using a microplate reader (Spark 10M; Tecan, Männedorf, Switzerland) and compared with a standard curve. The standard curve was generated using 2-aminoethanol (which has a known concentration of amino groups) instead of ApGltn. Lipopolysaccharide (LPS) was purchased from InvivoGen (USA).

ALA-ApGltn was synthesized by activation of ALA with EDC/NHS followed by reacting with the amino groups in ApGltn **(Figure 5-1A, B)** [192]. Briefly, 10 g of ApGltn was dissolved in 50 mL of 40 % ethanol/0.2 M pH 9.5 borate buffer. 896 µL of ALA (1 eq to the available amino groups in ApGltn) was dissolved in 50 mL of aqueous ethanol solution and then 1.5 eq of EDC and 2.0 eq of NHS were added to give the ALA-NHS ester **(Figure 5-1A)**. After reacting for 3 min, the pH of the reaction solution was adjusted to 4 to degrade unreacted EDC [193]. The activated ALA-NHS ester was then added dropwise to the ApGltn solution to initiate the modification reaction, which was allowed to run for 18 h at 50°C **(Figure 5-1B)**. The reaction solution was then added dropwise to 1000 mL of cold ethanol (10 times the reaction solution volume) to precipitate ALA-ApGltn. The ALA-ApGltn precipitate was then isolated by suction filtration using a glass filter and re-dispersed in 500 mL of ethanol to remove unreacted reagents, this was repeated 3 times. The remaining precipitate was dissolved in ultrapure water at 20 w/v% and dialyzed for 24 h using regenerated cellulose dialysis membrane (MWCO 3,500) (Spectra/Por® 3; Repligen, USA). The resulting white ALA-ApGltn powder was vacuum-dried at 25°C for 24 h. The modification ratio of the ALA group in ALA-ApGltn was determined using the TNBS method comparing the absorbance at 335 nm with that of Org-ApGltn. The modification was also confirmed by ^{1}H nuclear magnetic resonance (^{1}H-NMR) (JNM-ECS400; JEOL, Japan) and Fourier transform infrared spectroscopy (FT-IR) (ALPHA II; Bruker Corp., Billerica, USA).

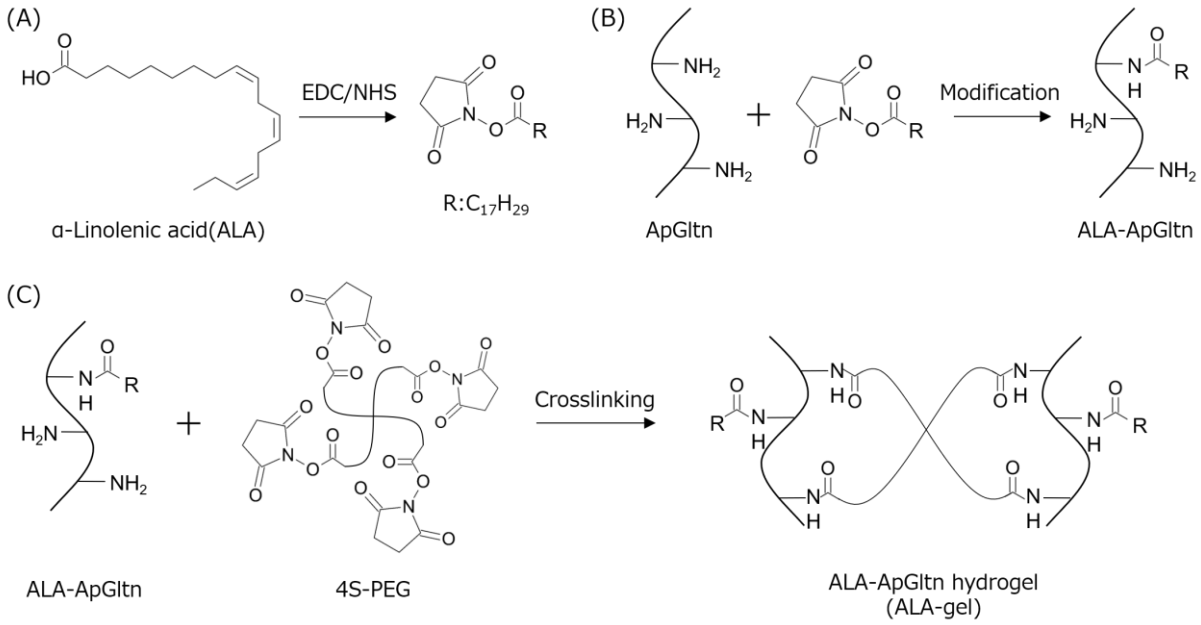

Figure 5-1. Synthesis of ALA-ApGltn via EDC/NHS chemistry [194]**.**
(A) Activation of ALA with EDC/NHS chemistry. (B) Modification of the activated ALA group to ApGltn molecules. (C) Preparation of ALA-gel using a 4S-PEG cross-linker.

5.2.3. Preparation of the Hydrogels

Org- and ALA-ApGltn were dissolved in 0.1 M pH 9.5 borate buffer at 20 w/v%. The amount of 4S-PEG was fixed at 0.5 eq of the residual amino groups in ALA-ApGltn. The same volume of Org- or ALA-ApGltn solution and 4S-PEG dissolved in 0.01 M pH4 phosphate solution were mixed to give Org- and ALA-gel **(Figure 5-1C)**.

5.2.4. Viscoelastic Properties of the Hydrogels

To evaluate the effect of ALA modification on the viscoelastic properties of the hydrogel, the rheology of Org- and ALA-gel was measured using a rheometer (MCR301; Anton Paar GmbH, Graz, Austria). Org- and ALA-ApGltn/4S-PEG mixtures were applied to the rheometer stage at 37°C and then a PP10 parallel plate was lowered to give a 1.0 mm gap before the hydrogels were cured. After waiting for 5 min, excess sample was removed, and the measurement was started. To determine the linear viscoelastic (LVE) region, strain sweep measurements were initially conducted at frequency (ω) = 10 rad/s and strain (γ) = 0.01%–1000 % [134].

Then a frequency sweep was measured using the specific strain value within the LVE region (10 %) and ω = 0.1%–100 %. We also evaluated the rheology of swollen hydrogels using a PP10 plate with waterproof sandpaper (C947H, Noritake Coated Abrasive, Japan) to prevent slipping during measurements. Org- and ALA-gel were cured at 1 mm thickness and then immersed in PBS at 8°C for 24 h. Swollen hydrogels were placed on the stage and sandwiched with a PP10 plate with sandpaper. A frequency sweep was conducted under the same conditions as for the measurement of the hydrogels that were not swollen. To assess the effect of ALA modification and swelling on the rheology, the storage modulus at 10 rad/s, which is defined as the elastic modulus [118], and tan δ at the same frequency were compared.

5.2.5. *Swelling Ratio of the Hydrogels*

The effect of ALA modification on the swelling ratio was evaluated using a previously reported method. Briefly, Org- and ALA-gels were prepared and cut into disks with 7 mm diameter and 1 mm thickness, and were weighed to give the initial weight. Hydrogels were separately immersed in PBS at 37°C using 5 mL tubes. At certain time points the PBS was discarded, remaining PBS around the hydrogels was wiped away, and the swollen weight of the hydrogels was measured. After weighing at 48 h, hydrogels were immersed in ultrapure water for 24 h to remove the remaining salt and then freeze dried. The freeze-dried hydrogels were weighed to give the dried weight. The swelling ratio was calculated using the following equation.

$$\text{Swelling Ratio} = \frac{W_s - W_d}{W_d}$$

where W_s and W_d indicate the weight of swollen and dried sealants, respectively.

5.2.6. *Degradation Properties of the Hydrogels*

The enzymatic degradation of the hydrogels was evaluated using collagenase, which cleaves peptide bonds in gelatin molecules. After preparation of the hydrogels, they were cut into 7 mm diameter and 1 mm

thick disks and allowed to pre-swell in PBS at 8°C for 24 h. The initial weights of the swollen hydrogels were denoted the 100 % fraction. The hydrogels were then immersed in 3 U/mL collagenase/PBS solution and weighed at predetermined time points. The percentage of the gel fraction was calculated by comparing with the initial weights of the swollen hydrogels.

5.2.7. Tissue Adhesion Properties of Hydrogels

The tissue adhesion properties of the hydrogels were evaluated on collagen sheets (casing) and porcine blood vessels. The tissue adhesion test was conducted according to the American Society of Testing and Materials (ASTM) F2392-04 [195], as we previously reported [189,190,195]. Briefly, collagen sheets and porcine blood vessels were cut into 30 mm diameter disks and then a 3 mm hole was punched in the center. The hydrogels were applied to the collagen sheets and porcine tissue before curing and molded into 15 mm diameter, 1 mm thicknesses using a silicone ring. After curing for 5 min, the tissue and hydrogel samples were placed in the testing apparatus. Saline was flowed at 2 mL/min to load pressure from the bottom of the hydrogels. The maximum pressure when the hydrogels were broken, or saline leakage was confirmed, was defined as the burst strength.

5.2.8. Antioxidant Properties

The antioxidant properties of ALA-ApGltn were evaluated using ABTS according to the procedure in a previous study with a minor change [196]. Briefly, ABTS was dispersed in ultrapure water at 7 mM and then 2.45 mM potassium persulfate was added to generate $ABTS^{\bullet+}$. After mixing for 5 min, 100 μL of solution was dispensed into a 96 well plate. Org- and ALA-ApGltn were dissolved in PBS at 0.03~1.0 w/v%, and 50~800 μM of ALA conjugated to BSA at a 5:1 molar ratio was also dissolved in PBS. 100 μL of each solution was mixed with $ABTS^{\bullet+}$ in a well plate and then incubated for 24 h at 37 °C. The absorbance of the resulting

solution at 734 nm (Abs_x) was measured using a microplate reader (Spark 10M, Tecan, Männedorf, Switzerland). PBS mixed with $ABTS^{\bullet+}$ was used as the control absorbance (Abs_{PBS}). The radical scavenging efficiency was calculated using the following equation:

$$\text{Scavenging (\%)} = \left(1 - \frac{Abs_x}{Abs_{PBS}}\right) \times 100$$

In addition, the required radical inhibitory concentrations (IC) 80% were calculated using each approximate curve.

5.2.9. *In vitro Anti-Inflammatory Activity of ALA-ApGltn and Hydrogels*

The anti-inflammatory effects of ALA-ApGltn were evaluated using mouse macrophage-like cells RAW264.7 (purchased from the European Collection of Authenticated Cell Cultures (ECACC)). Cells were cultured in RPMI 1640 supplemented with 10% FBS and 1% PenStrep. Cells were seeded in a 96-well plate at 2.0×10^4 cells/well and then incubated for 24 h at 37°C in 5% CO_2. The culture media was then replaced with new media supplemented with various concentrations of Org- and ALA-ApGltn/PBS solutions and ALA/BSA complex (5:1 molar ratio) [197,198]. LPS dissolved in PBS was then added to the culture (final concentration 10 ng/mL). After incubating for 24 h, the culture supernatants were separated for the enzyme-linked immune sorbent assay (ELISA) and replaced with WST-8 reagent (Nacalai Tesque, Kyoto, Japan) 10× diluted in new culture media. The culture plate was incubated for 2 h, and its absorbance at 450 nm was measured using a microplate reader (Spark 10M, Switzerland). The calibration curve was generated by serial dilutions of cell suspensions. The cell viability (%) was calculated by comparing with the cell number of the control group. The concentration of TNF-α in the culture supernatants was measured using an ELISA kit (R&D Systems, USA), following the manufacturer's instructions.

The cell viability on the hydrogels was measured using Org- and ALA-gels and the same conditions

as for other experiments. After swelling in PBS for 24 h, hydrogels were cut into 10 mm diameter samples, placed in 48-well plates and UV sterilized for 60 min. RAW264.7 cells were seeded on the hydrogels at 6.0×10^4 cells/well, and LPS was added to give a final concentration of 10 ng/mL. After incubating at 37°C in 5 % CO_2 for 24 h, the cell viability and ELISA of TNF-α were measured.

Following the cell viability measurement, cells on the well plate and hydrogels were fixed with 4 % PFA/PBS for 15 min and then permeabilized with 0.1 % Triton-X100/PBS for 20 min. Actin filaments in the cells were then stained with 5 μg/mL of phalloidin-TRITC in PBS solution for 30 min. In addition, cell nuclei were stained with 1 μg/mL DAPI/PBS solution for 20 min.

Mitochondria and intracellular ROS were visualized to assess the cellular activity and anti-inflammatory effects. Briefly, RAW264.7 cells were seeded in a 96-well plate at 2.0×10^4 cells/well and cultured for 24 h. Various concentrations of Org- and ALA-ApGltn/PBS solutions as well as ALA/BSA complex (5:1 molar ratio) were added to the cell culture and then incubated for 24 h. Subsequently, the cell supernatants were replaced with new media supplemented with 30 nM of MitoTracker Orange CMTMRos or 5 μM of CellROX Orange Reagent. After incubating for 30 min at 37°C, the culture media was replaced with new media containing NucBlue (2 drops/mL) and then sample were incubated for 20 min.

5.3. Results and Discussion

5.3.1. Synthesis of ALA-ApGltn

ALA-ApGltn was synthesized by condensation between the carboxy groups of ALA and amino groups of ApGltn through EDC/NHS chemistry. The yield of ALA-ApGltn was 80.6 g/g%, and the modification ratio of ALA groups to the total amino groups in ApGltn, determined using the TNBS method, was 44.6 mol%. The FT-IR spectra of Org- and ALA-ApGltn are shown in **Figure A-13**. The difference spectrum between the Org- and ALA-ApGltn spectra indicates that the increase of absorption at 2850~3000 cm^{-1} was attributed to C-H

stretching, which was enhanced by the ALA modification. In addition, the ^{1}H-NMR spectra of Org- and ALA-ApGltn showed that peaks at 2.43, 3.24, and 5.18 ppm emerged following ALA modification (**Figure A-14**). The peak at 2.43 ppm was attributed to the α-methylene of ALA. The peak at 3.24 ppm was attributed to the ε-methylene of lysine, which was shifted downfield from 2.86 ppm by modification with the carbonyl group of ALA and the resulting decrease in electron density. Besides, the peak at 5.18 ppm in the ALA-ApGltn spectrum was attributed to the vinylic protons of the ALA molecule. Therefore, ALA-ApGltn was successfully synthesized by EDC/NHS chemistry.

5.3.2. Viscoelastic Properties of the Hydrogels

The bulk strength of hydrogels plays an important role in tissue adhesion. Hence, we assessed the effects of ALA modification on the rheological properties before and after swelling to evaluate the mesh structure of the ALA-gel. A strain sweep of the Org- and ALA-gels was initially measured to determine the LVE region **(Figure A-15)**. As the strain range of 0.1~10 % was found to be LVE region, the frequency sweep measurement was conducted at 1 % strain. **Figure 5-2A, B** show the frequency sweeps for Org- and ALA-gels with and without swelling, respectively. The rheology before and after swelling showed that the storage modulus (G′) of both the Org- and ALA-gels exceeded their loss modulus (G″) over the whole frequency range, indicating characteristic hydrogel properties resulting from successful crosslinking. The elastic modulus of the Org- and ALA-gels was taken at 10 rad/s to compare their bulk strength **(Figure 5-2C)**. No significant difference between Org- and ALA-gel was observed before or after swelling, indicating that neither introduction of the ALA group into ALA-ApGltn nor swelling led to significant change in the elastic moduli. We previously reported that saturated fatty acid (SFA)-modified ApGltn hydrogels ha d a significantly higher elastic modulus compared with Org-ApGltn hydrogel owing to the increased physical crosslinking points

provided by hydrophobic interactions between SFA moieties [112,119,191]. SFAs contain a linear hydrocarbon chain and can easily form lateral packing structures, which correlates with their relatively high melting point. In addition, the conformational freedom of hydrocarbon chains in SFAs is relatively high, leading to the formation of physical crosslinking points and enhancement of the bulk strength of the hydrogels. However, PUFAs contain at least one double bond in the hydrocarbon chain leading to a bent structure, which results in lower packing densities. Therefore, the intermolecular physical crosslinking between ALA groups was easily disrupted by loaded force and insufficient to significantly change the elastic modulus of the ALA-gel. We also

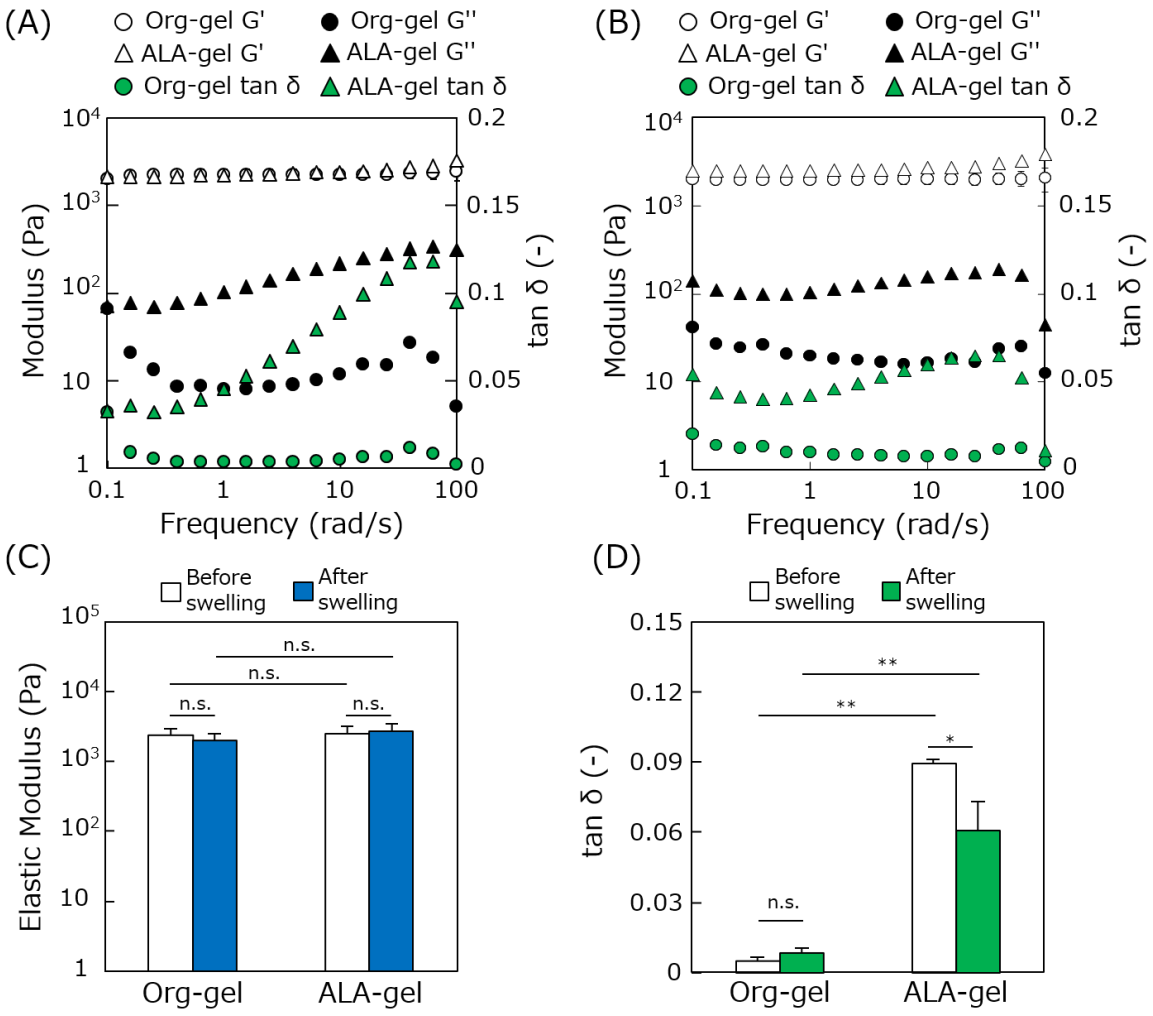

Figure 5-2. Rheological measurements of hydrogels [194].

Viscoelastic properties of Org- and ALA-gel with (A) and without (B) swelling. Comparison of elastic modulus (C) and tan δ at 10 rad/s (D). n.s. indicates no significant difference ($p>0.05$). * and ** indicate significant differences with $p<0.05$ and $p<0.01$, respectively.

measured tan δ, which is a ratio of G″ to G′, to evaluate the morphological change when force was applied to the hydrogels **(Figure 5-2D)**. Although tan δ of the swollen Org-gel was not significantly different to that of the pre-swollen state, both were significantly lower than tan δ of ALA-gel with and without swelling. These observations are attributed to energy dissipation by the intermolecular interaction and rearrangement of ALA moieties in ALA-ApGltn. When force was applied to the ALA-gel, the stacked ALA moieties are thought to have deformed and rearranged with other ALA groups, leading to increases in G″ and tan δ. However, Org-gel was elastically deformed by the force because it had no additional physical crosslinking, resulting in lower G″ and tan δ. In addition, tan δ of the swollen ALA-gel was significantly lower than that of the pre-swollen state. It is thought that in the swollen state the ALA groups were less likely to form the stacked state as easily owing to the expanded mesh structure of the hydrogel, leading to a decrease in energy dissipation properties and a lower value of tan δ.

5.3.3. Swelling Ratio of Hydrogels

The swelling ratios of Org- and ALA-gels were measured to assess the effect of swelling on tissue adhesive properties. **Figure 5-3A** shows that the swelling ratio of Org- and ALA-gel reached a plateau after 8 and 2 h, respectively. In addition, the swelling ratio of ALA-gel exceeded that of Org-gel throughout the measuring time. Although the ALA modification did not significantly affect the elastic modulus of ALA-gel, it significantly enhanced the resistance to swelling owing to the increase of physical crosslinking points and the hydrophobicity of ALA-ApGltn molecules, leading to the inhibition of hydrogel mesh network expansion and the repulsion of water molecules. However, the swelling of materials inhibits the tissue adhesion properties because swelling exerts shear force on the interface between the tissue and the adhesive. ALA-gel has a lower swelling ratio than Org-gel and is suitable for tissue adhesion under physiological conditions.

5.3.4. *Degradation Properties of Hydrogels*

The degradation profiles of Org- and ALA-gel were measured to assess the degradation profile under physiological conditions. **Figure 5-3B** shows the degradation profiles of Org- and ALA-gel, it can be seen that ALA-gel has a slower degradation rate than Org-gel. To compare the degradation of Org- and ALA-gels, their half-lives were calculated using the approximate curves. The half-life of Org-gel was 2.88 h, whereas, that of ALA-gel was 3.6 h. In addition, the complete degradation times of Org- and ALA-gel were 6 and 8 h, respectively. The difference between these findings is attributed to inhibition of collagenase molecule entry into the hydrogel by the increased physical crosslinking between the ALA groups in ALA-ApGltn, in addition to the swelling. Therefore, ALA-gel is considered appropriate for use as a tissue adhesive for wound closure because it can remain stable under physiological conditions for a relatively long period.

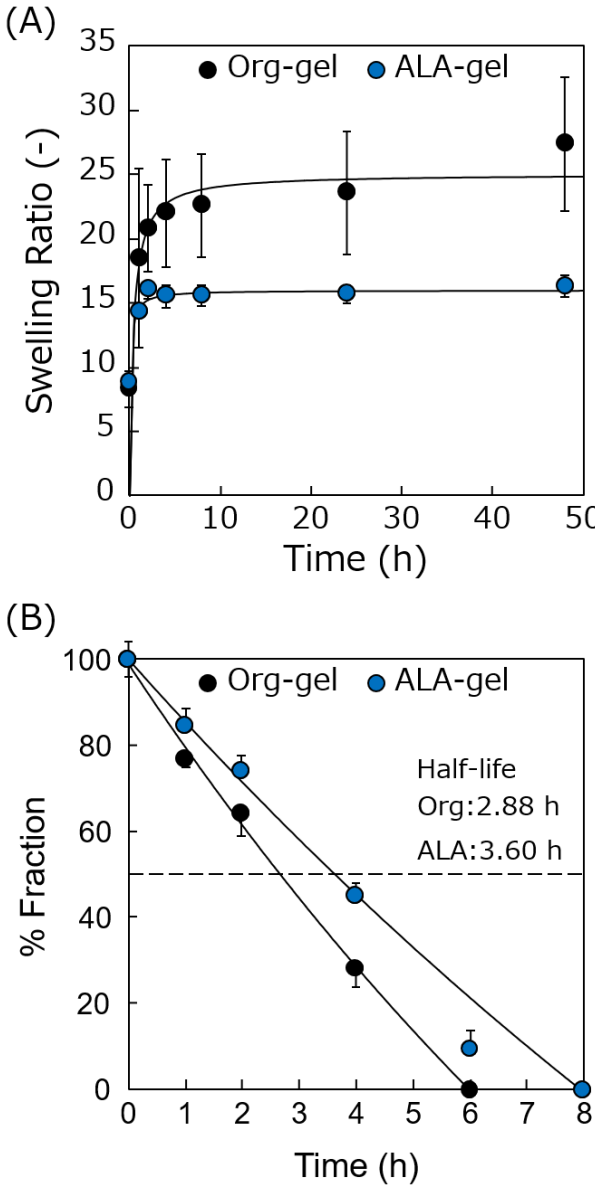

Figure 5-3. Swelling and degradation properties of FSs [194].

Time course change of swelling ratio (A) and enzymatic degradation behavior (B) of Org- and ALA-gel.

5.3.5. *Tissue Adhesion Measurements*

ALA modification of the gel was expected to enhance the burst strength since SFA-modified ApGltn-based adhesive showed significantly higher burst strength than both non-modified adhesive and a commercially available adhesive, as we reported previously [112,189–191]. Hence, the burst strength of ALA-gel was evaluated using collagen casing and porcine aorta tissue with a 3 mm hole **(Figure 5-4A)** and ASTM F2392-04 apparatus **(Figure 5-4B)**. **Figure 5-4C** shows the burst strength of Org- and ALA-gel as well as commercially available fibrin adhesive, on a collagen casing. Although the storage modulus of fibrin adhesive was reported to be 2~3 kPa [199], which was compatible with that of Org- and ALA-gel, the burst strength of fibrin adhesive was 19.1 ± 13.3 cmH_2O, which was significantly lower than that of Org- and ALA-gel. This is expected to be the result of fibrin adhesive having insufficient interfacial adhesion, whereas, 4S-PEG

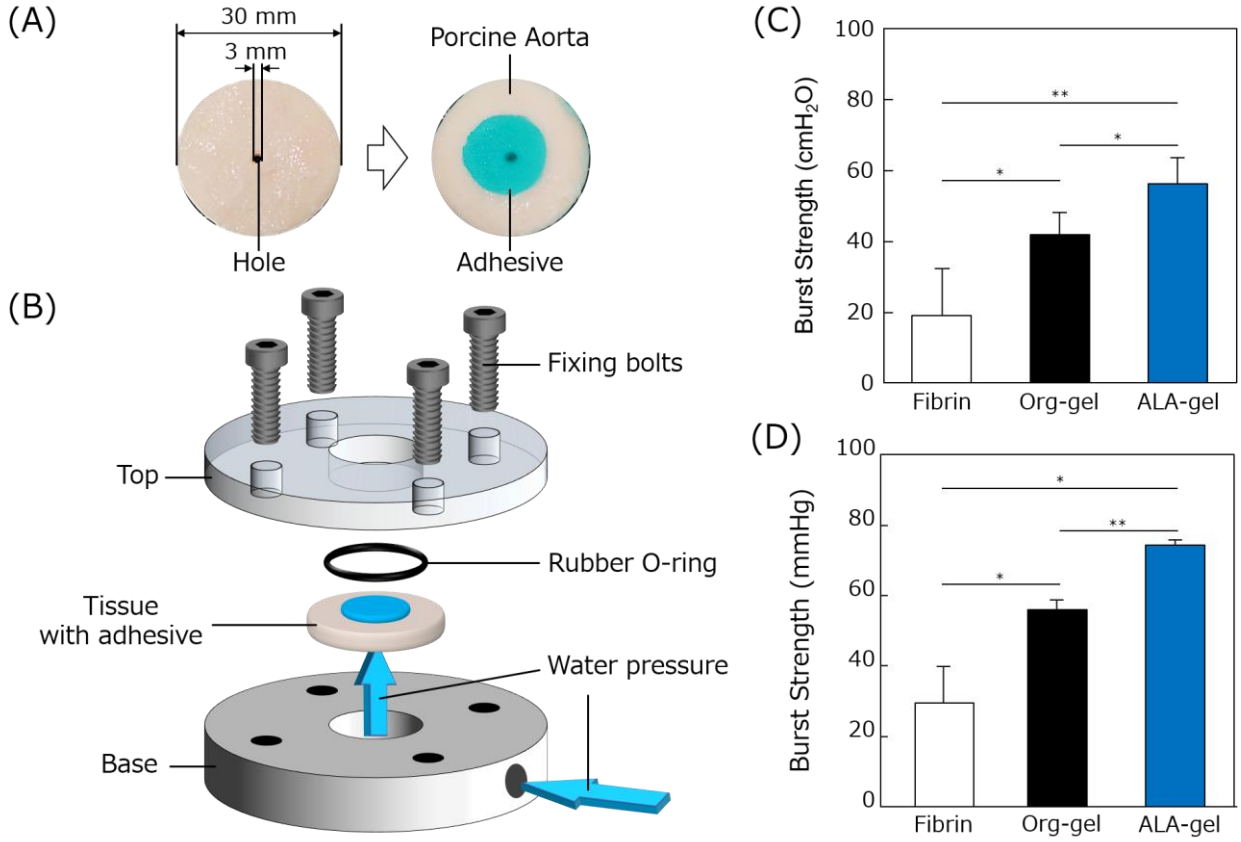

Figure 5-4. Burst strength test using ASTM F2392-04 [194].
(A) Image showing the dimensions of tissue with a hole following ASTM. (B) Test apparatus for burst strength test. Burst strength of Org- and ALA-gel on collagen casing (C) and porcine aorta (D). * and ** indicate significant differences with $p<0.05$ and $p<0.01$, respectively.

crosslinker can react with amino groups in tissue matrices as it crosslinks ApGltn molecules, enhancing the interfacial adhesion. ALA-gel demonstrated a significantly higher burst strength (56.4 ± 7.4 cmH_2O) than Org-gel (42.1 ± 6.1 cmH_2O) because the introduction of hydrophobic moieties in ApGltn enhanced its interaction with hydrophobic amino acid-rich sequences in collagens [140,200].

We also measured the burst strength on porcine aorta using a similar method **(Figure 5-4D)**. The burst strengths of Org- and ALA-gel were significantly higher than the previously reported value for fibrin adhesive (29.3 ± 10.5 mmHg) [189]. In addition, similarly to the results of burst strength on a collagen casing, ALA-gel demonstrated a significantly higher burst strength (74.3 ± 1.5 mmHg) than Org-gel (56.0 ±2.6 mmHg). These observations were a result of the enhanced interaction of the ALA group with porcine aorta tissue. We previously reported that SFA-modified ApGltn demonstrated increased interactions with cells and extracellular matrices (ECM) [191]. Therefore, in the case of ALA-ApGltn it was assumed that the ALA moieties interacted with the hydrophobic components of the cell membrane and ECM such as collagen, tropoelastin, and fibronectin. In addition, the followability of ALA-gel to porcine tissue increased. Upon porcine tissue swelling as a result of the loaded pressure during the burst strength test, ALA-gel followed the swelling tissue well and was prevented from peeling by its higher loss modulus and tan δ. Based on the normal human systolic (120–139 mmHg) and diastolic (80–89 mmHg) blood pressures [201], the burst strength of ALA-gel was not sufficient to close blood wounds alone. Therefore, ALA-gel could be clinically applied as a supportive adhesive or a hemostatic sealant to accompany suturing.

5.3.6. *Antioxidant Properties of ALA-ApGltn*

The antioxidant properties of ALA-ApGltn were measured to evaluate whether the antioxidant properties of the ALA molecule were maintained after modification on ApGltn. **Figure 5-5A** shows the

antioxidant properties of Org- and ALA-ApGltn at 0.03–1.0 w/v%, indicating that their scavenging percentage increased up to 0.25 w/v% in a dose dependent manner, and then reached a plateau over 0.25 w/v%. The required concentration for IC80 was calculated from the approximate curve. The IC80 concentrations of Org- and ALA-ApGltn were 0.18 and 0.15 w/v%, respectively, indicating that they had compatible antioxidant effects. These findings were a result of the natural antioxidant properties of ApGltn, which are attributed to specific amino acid sequences such as YGCC, DSSCSG, NNAEYYK, and PAGNVR [202], and modification with ALA did not dominantly affect the antioxidant properties at a modification ratio of 45 mol%. We also compared the antioxidant properties of ALA/BSA complex and ALA-ApGltn in terms of the molar ratio of ALA moieties. **Figure 5-5B** indicates that the scavenging percentage of ALA-ApGltn reached a plateau around 330 μM, whereas, the ALA/BSA complex required 600 μM to reach a plateau. The IC80 concentration of ALA moieties in ALA/BSA and ALA-ApGltn was 555.1 and 192.9 μM, respectively, indicating that ALA-ApGltn exerted more effective radical scavenging properties than ALA/BSA by the natural antioxidant properties of ApGltn. Therefore, both Org- and ALA-ApGltn were expected to efficiently scavenge ROS in cells or tissue to reduce continuous inflammation.

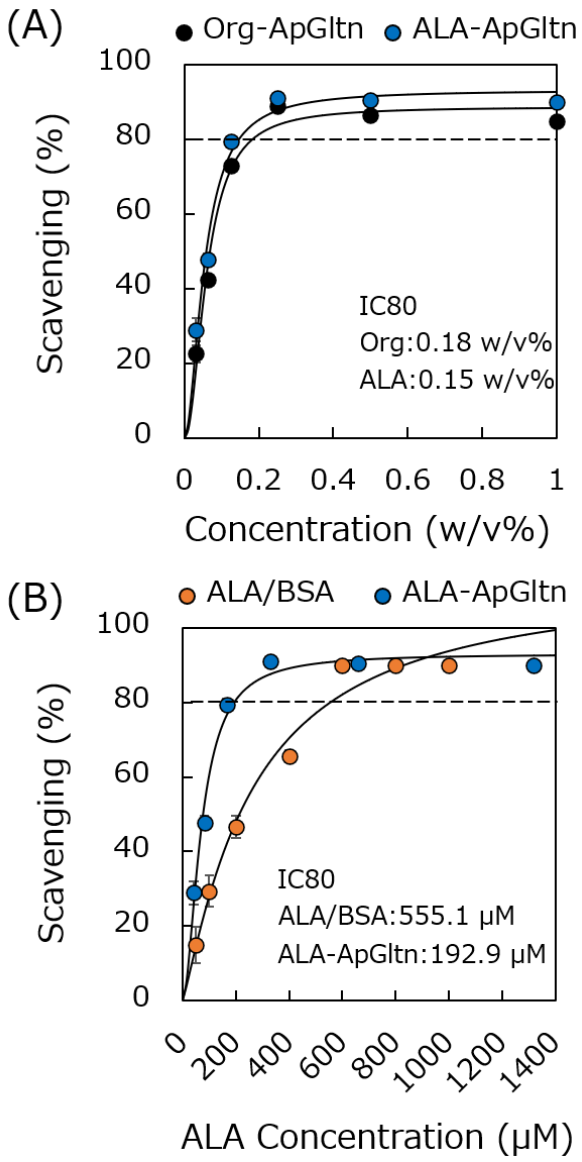

Figure 5-5. Measurements of antioxidant properties using ABTS [194].
Radical scavenging activities in terms of gelatin concentration (A) and ALA concentration (B).

5.3.7. In Vitro Anti-inflammatory Effects

The anti-inflammatory effects and the advantage of ALA modification in ALA-ApGltn were also evaluated. **Figure 5-6A, A-17** indicates the cell morphology of LPS-activated RAW264.7 cells cultured with ALA/BSA complex, Org-, and ALA-ApGltn. The size of LPS-activated cells was increased by Toll-like receptor (TLR)-4 mediated pathways including myeloid differentiation primary response 88 (MyD88) and JNK as well as p38 MAPK [203], leading to an increase in the number of vacuoles [204]. ALA/BSA conjugate suppressed the enlargement of cells and was expected to have anti-inflammatory responses. Despite the antioxidant properties of Org-ApGltn, it did not affect the morphological changes of LPS-activated cells; however, ALA-ApGltn successfully suppressed the enlargement of RAW264.7 cells, which was attributed to be the suppressive effect on LPS-mediated inflammation. The cell viability quantified by WST-8 indicated the significant cytotoxicity of ALA/BSA complex in a dose dependent manner, whereas, other groups did not show significant lower viability except for ALA-ApGltn at 1.0 w/v% **(Figure 5-6C)**. The cytotoxicity of high concentrations of ALA was attributed to the oxidized product of ALA. An increase of intracellular PUFA level leads to lipid peroxidation by enzymatic and non-enzymatic reactions to produce cytotoxic oxidized products [186,188]. Oxidized DHA induced apoptosis by inhibiting the mitochondrial respiratory system [186] and activation of caspase due to the increased ROS production caused by lipid peroxides followed by the activation of caspase-8 and -9 [186,187]. Hence, ALA, which is also an omega-3 PUFA, was expected to inhibit mitochondrial activity, leading to cell apoptosis. **Figure 5-6B** (left column) shows that lower mitochondrial activity (red staining) was confirmed when cells were cultured with ALA/BSA at 600 μM compared with the other groups, indicating that the significant cytotoxicity was based on the mitochondrial dysfunction. On the other hand, ALA-ApGltn did not negatively affect the mitochondrial activity. This phenomenon was seemingly due to the suppressed cell internalization of ALA moieties by the introduction of them to ApGltn.

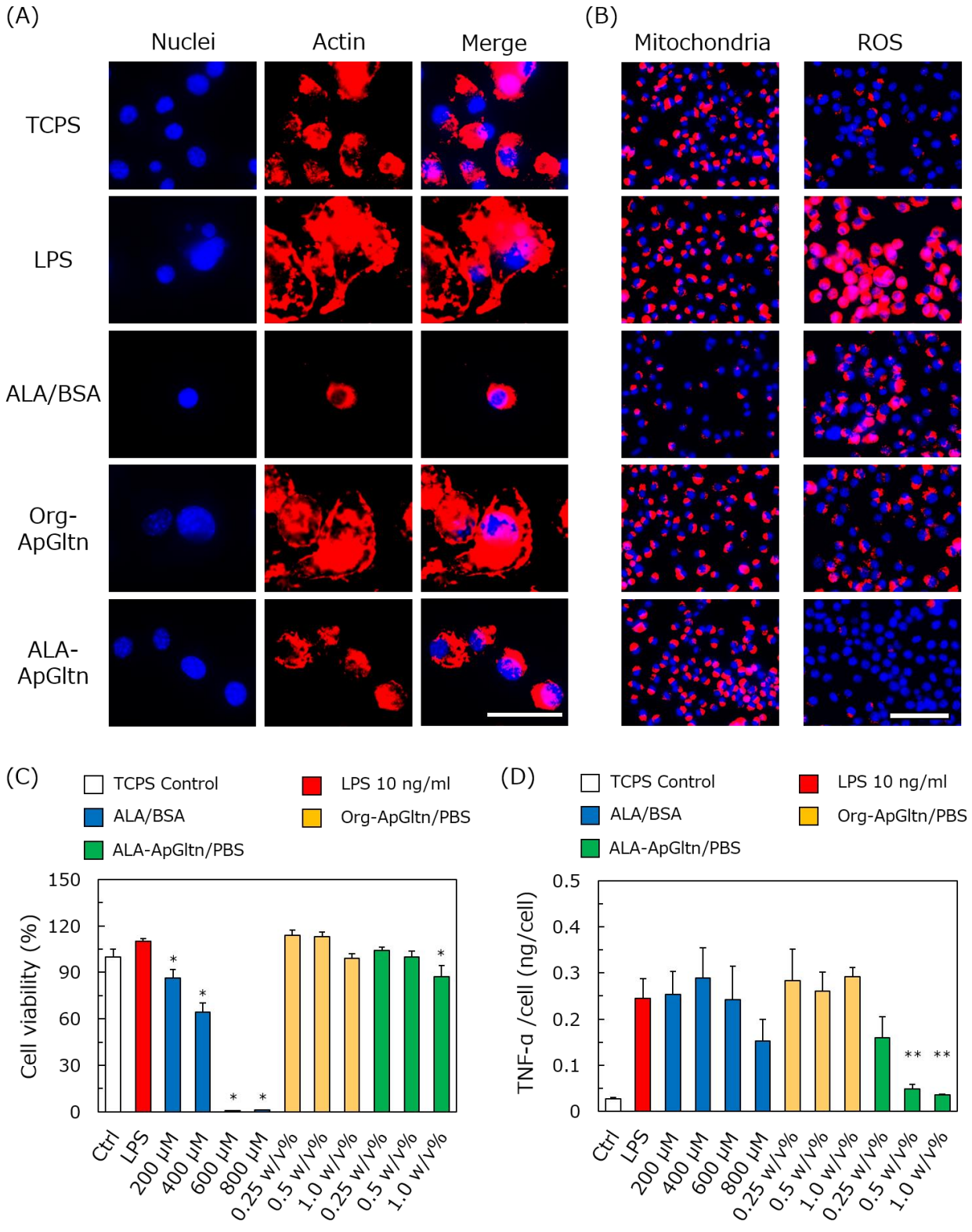

Figure 5-6. Cell responses on Org- and ALA-ApGltn [194]**.**

(A) Microscopy of RAW264.7 cells cultured with each group. Scale bar = 50 μm. (B) Intracellular mitochondrial and ROS activities. Scale bar = 100 μm. (C) Cell viability of RAW264.7 cells cultured with different concentration samples. * indicates a significant difference from the viability of TCPS control. (D) Secreted amount of TNF-α per cell. ** indicates significant difference from the TNF-α/cell of LPS ($p<0.01$).

The secreted amount of TNF-α per cell is shown in **Figure 5-6D, A-16**. LPS strongly stimulated the secretion of TNF-α (0.245 ng/cell) compared with the TCPS control (0.027 ng/cell). The ALA/BSA complex demonstrated no significant decrease in TNF-α/cell even at concentrations of 600 or 800 μM, despite having antioxidant effect. This result was due to the enhanced inflammatory response and TNF-α secretion caused by the strong cytotoxicity of those concentrations. In contrast, Org-ApGltn did not inhibit the inflammatory response despite the natural antioxidant properties of ApGltn, whereas, ALA-ApGltn at 0.5 and 1.0 w/v% significantly reduced the TNF-α secretion. The ALA concentrations in 0.5 and 1.0 w/v% ALA-ApGltn were 659 and 1318 μM, respectively, indicating that ALA-ApGltn demonstrated comparable anti-inflammatory activity to ALA/BSA at the same concentration, while maintaining higher cell viability. The anti-inflammatory effect of ALA-ApGltn was attributed to the interaction between ALA and GPR120 or GPR40, leading to the suppression of NF-κB and its downstream signaling pathways [179]. We also observed the intracellular ROS level (**Figure 5-6B** right column), which indicated that ROS production was significantly enhanced by LPS stimulation. The sustained high level of intracellular ROS when cultured with ALA/BSA at 600 μM was due to the increased cytotoxicity and production of ROS by lipid peroxidation [187]. Org-ApGltn also had a low intracellular antioxidant effect despite the prominent antioxidant properties of ApGltn because the cell internalization of ApGltn was lower than that of smaller molecules such as ALA. This result correlated with the higher TNF-α secretion. However, ALA-ApGltn significantly suppressed intracellular ROS to the normal level, which was correlated with the inhibited secretion of TNF-α by ELISA. Therefore, the anti-inflammatory effects of ALA-ApGltn were ascribed to the dominant inhibition of NF-κB pathways as a result of binding ALA moieties to GPR120 or GPR40 receptors, followed by suppressed TNF-α secretion and ROS production.

We also evaluated the effect of ALA-gel on cell viability and anti-inflammatory effects. The cell morphology of LPS-activated cells on Org- and ALA-gel indicated the significant suppression of cell

enlargement and formation of lamellipodia **(Figure 5-7A)** [204,205]. **Figure 5-7B** shows the cell viability on Org- and ALA-gel with different final concentrations of Org- and ALA-ApGltn, indicating that no significant difference was confirmed among those groups. ALA-gel did not demonstrate significant cytotoxicity despite the cytotoxicity of ALA-ApGltn at 1.0 w/v% in **Figure 5-6C**, indicating that crosslinking with 4S-PEG reduced the internalization of free ALA-ApGltn molecules and suppressed cytotoxicity. Moreover, ALA-gel with 5–15 w/v% significantly suppressed the secretion of TNF-α from LPS-activated RAW264.7 cells compared with

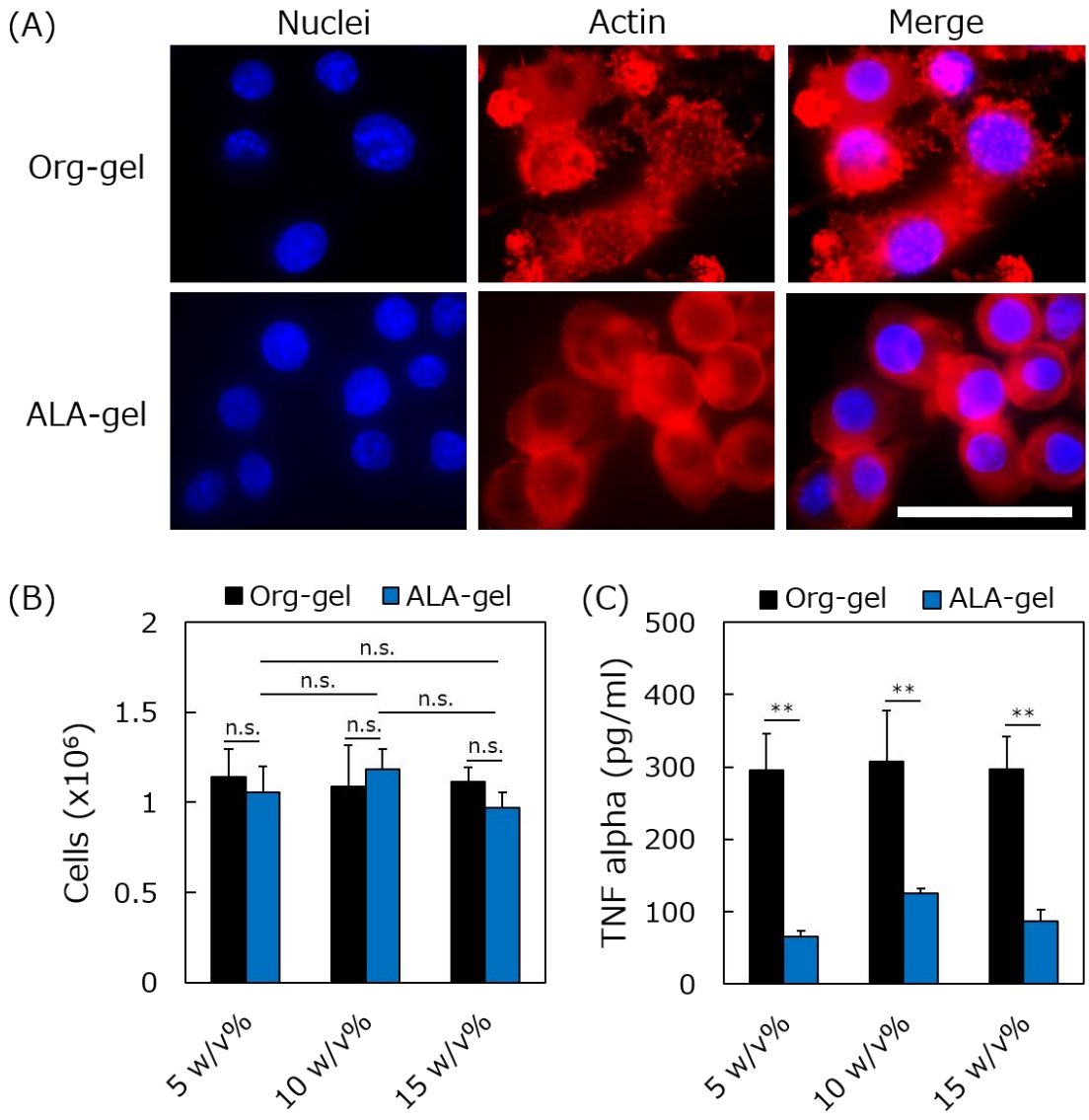

Figure 5-7. Anti-inflammatory activity of ALA-gel [194]**.**
(A) Microscopy of LPS-activated RAW264.7 cells cultured on Org- and ALA-gel. Scale bar = 50 μm. (B) Cell viability of RAW2647 cells on Org- and ALA-gel. n.s. indicates no significant difference ($p<0.05$). (C) The secreted concentration of TNF-α. ** indicates significant differences at each gelatin concentration. ($p<0.01$)

Org-gels **(Figure 5-7C)**. These results indicated that the immobilization of ALA molecules in ApGltn led to prominent anti-inflammatory effects and cell viability even after forming the hydrogel. Therefore, ALA-gel is a potential multifunctional biomaterial with tissue adhesive and anti-inflammatory properties to suppress severe inflammation and enhance wound healing. Although the radical scavenging activity of ApGltn was not exerted in cell experiments, it is thought to scavenge ROS in the ECM rather than inside the cell, leading to sustained antioxidant activity until the complete degradation of ALA-gel in vivo. However, different kinds of PUFA have different bioactivity, including anti-inflammatory and cytotoxic properties, therefore, the anti-inflammatory effects can be optimized through PUFA selection and modification ratio. On the other hand, since PUFAs are reported to have antimicrobial properties, ALA-gel is expected to prevent infection during surgery. Therefore, further evaluations of the antimicrobial activity of ALA-gel is required to assess its potential as a multifunctional device with not only anti-inflammatory and tissue adhesive properties but antimicrobial activities, which lead to prevent medical device-associated infections.

5.4. Conclusion

We developed an ALA-gel that exhibits anti-inflammatory and tissue adhesion properties. ALA-gel had energy dissipating properties owing to its high tan δ value. In addition, ALA-gel exhibited greater tissue adhesion compared with Org-gel. Furthermore, ALA-ApGltn supported greater cell viability and mitochondrial activity compared with non-conjugated ALA, while maintaining suppressed TNF-α secretion. Moreover, cells cultured on ALA-gel also showed retained cell viability and reduced TNF-α secretion. Therefore, ALA-gel has potential as a multifunctional biomaterial with tissue adhesion and anti-inflammatory properties, not only for wound sealing and burn injury treatment, but also for treating rheumatoid arthritis.

CHAPTER 6: Concluding Remarks

The aim of this study was the development of angiogenic materials and anti-inflammatory materials to promote soft tissue regeneration by promoting transplantation efficacy and inflammation resolving. Regenerative medicine is one of the most promising approaches to regenerate damaged/dysfunctional tissues and organs. Transplantation of healthy cells or stem cells to target organs/ tissues are mainly conducted; however, there are difficulties in survivability and retention of transplanted cell, resulting in low treatment efficacy. Although generating vascular bed to supply oxygen and nutrients to transplanted cells by delivering growth factors have been demonstrated to improve the cell survivability, the short half-life of growth factors limits their practical realization. To overcome those challenges, the angiogenic materials stimulating the inflammatory response and endogenous secretion of growth factors by mimicking LPS structure was proposed to achieve angiogenesis.

In chapter 2, hm-ApGltn with different alkyl chain length was synthesized to evaluate the effect of angiogenic responses. Hydrated C12-ApGltn formed self-assembled hydrogel, while Org-, C6- and C18-ApGltn solutions did not form hydrogel. In vitro experiments demonstrated that C12-ApGltn stimulated macrophages to secrete significantly higher amount of VEGF than Org-ApGltn and other hm-ApGltns. When TLR4 of macrophages is inhibited by blocking peptides, the VEGF secretion induced by C12-ApGltn was suppressed. Moreover, C12-ApGltn hydrogel promoted angiogenesis in mouse subcutaneous without using growth factors. Histological observations of the C12-ApGltn hydrogel implanted site showed the significantly

higher expression of VEGF, NF-κB and CD31, suggesting the angiogenic responses are induced through activation of TLR4 and NF-κB followed by VEGF secretion and capillary formations.

Although C12-ApGltn hydrogel induced angiogenesis, the degradation and dispersion of the hydrogel in mouse subcutaneous limited sustained angiogenesis. In order to improve the degradation resistance, C12-ApGltn was made into the microparticle to demonstrate the sustained angiogenesis in chapter 3. C12-ApGltn microparticle (C12-MP) was prepared by coacervation method followed by the thermal crosslinking. The spherical structure of C12-MP was confirmed by SEM observations. The rheological measurements of C12-MP suspensions showed that C12-MP and Org-MP suspensions formed hydrogel with thixotropic properties. Similar to the in vitro experiment in chapter 2, C12-MPs also promoted secretion of VEGF from macrophages through activation of TLR4. In vivo experiments using LDPI demonstrated that C12-MP3 hydrogel stimulated acute angiogenic responses by day 2, whereas C12-MP6 and MP9 hydrogels induced sustained angiogenesis for up to 22 days. Those results suggested the time course of angiogenesis was adjustable by changing the thermal crosslinking time.

In chapter 4, C16-ApGltn was synthesized by the modification of octadecyl groups, which also binds to TLR4 to induce inflammatory responses and angiogenesis. C16-ApGltn was made into fiber sheets (C16-FS) by electrospinning followed by the thermal crosslinking to increase the contact surface area to tissue and the degradation resistance. C16-FS demonstrated sustained angiogenesis in mouse subcutaneous for up to 14 days. Those growth factor-free angiogenic materials are potential therapeutic biomaterials to not only generate a vascular bed for cell/tissue transplantations but treatments for ischemic diseases.

From a different perspective, the anti-inflammatory biomaterial was proposed to resolve inflammatory responses and promote tissue regenerations upon injuries. In chapter 5, ALA-ApGltn was synthesized by reacting ApGltn and ALA, which exert anti-inflammatory and antioxidant properties. ALA-ApGltn was

crosslinked by 4S-PEG to form ALA hydrogel. The viscoelastic measurements of ALA hydrogel showed no significant difference in storage modulus with Org hydrogel; however, the loss modulus of ALA hydrogel was significantly higher than that of Org hydrogel, indicating ALA hydrogel had energy dispersing ability. The anti-inflammatory ability of ALA-ApGltn was evaluated using activated macrophages by LPS. ALA-ApGltn significantly suppressed the secretion of TNF-α when compared with control and Org-ApGltn. Moreover, the secretion of TNF-α was also inhibited when activated macrophages were cultured on the ALA hydrogel. Furthermore, mitochondrial toxicity of ALA-ApGltn was greatly lower than that of ALA molecules, which was advantageous over drug-loaded materials and potential application for biomedical use.

In summary, an angiogenic and anti-inflammatory biomaterials were developed to promote tissue regeneration from different perspectives. The induction of endogenous growth factor secretion and angiogenesis by C12-ApGltn is accompanied by pro-inflammatory secretions, which may lead to induce various complications such as pain and toxicity. Therefore, the combination of C12-ApGltn and ALA-ApGltn may not only mitigate the adverse effects of C12-ApGltn but also control inflammatory level after injury, leading to achieve faster soft tissue regenerations.

Appendix − Supplementary Figures

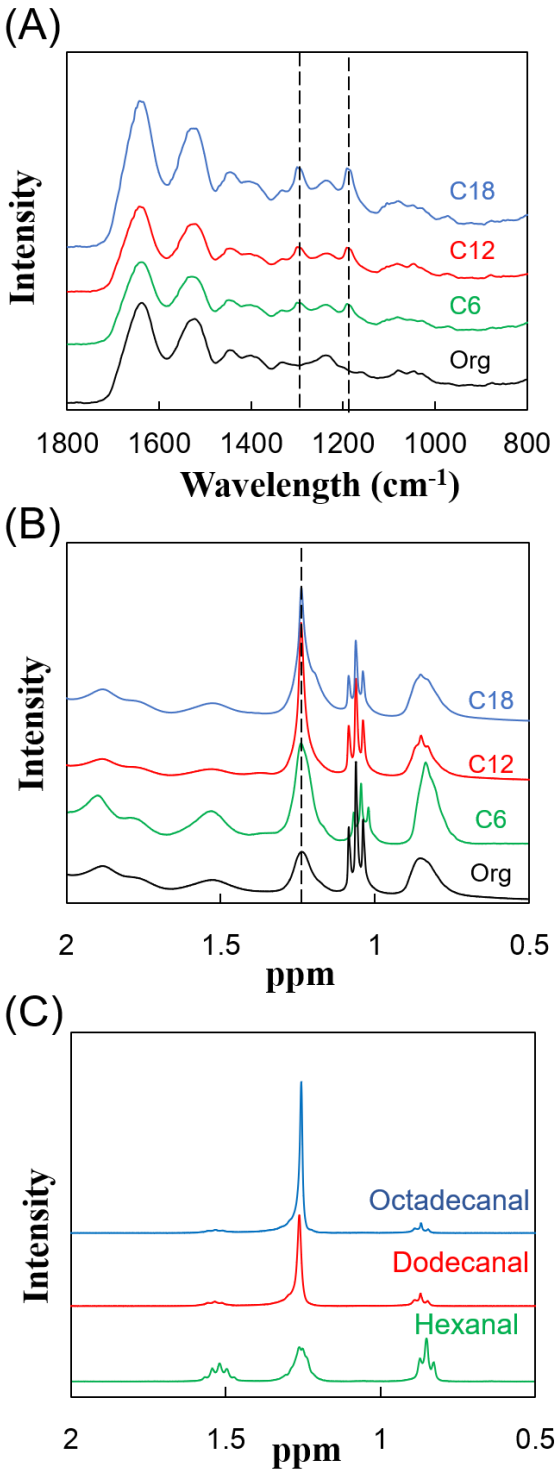

Figure A-1. Characterization of Org- and hm-ApGltn.
Fabricated hydrogels were characterized by (A) FT-IR and (B) 1H-NMR. (A) Broken lines at 1195 and 1300 cm^{-1} indicate C-H rock and C-H scissoring, respectively. (B) The strong peak at 1.25 ppm correlates to (C) the spectra of fatty aldehydes.

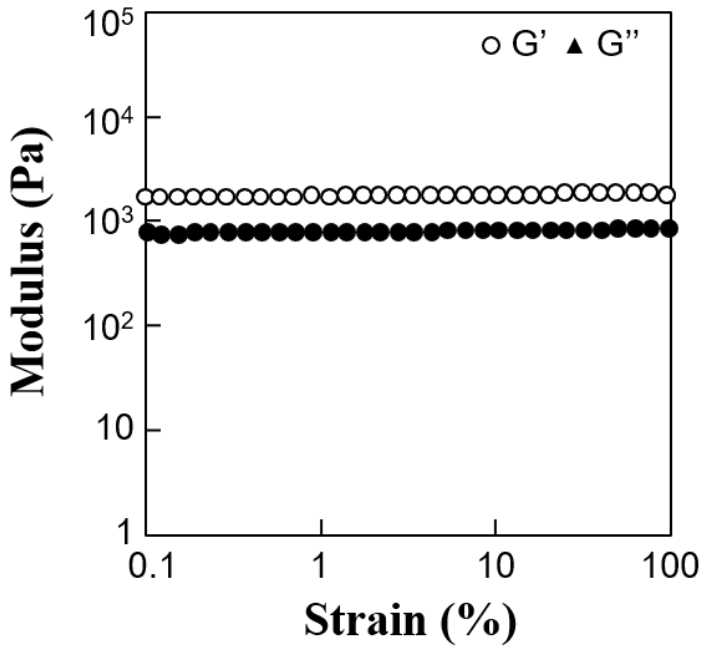

Figure A-2. Strain sweep measurement on C12-ApGltn hydrogel at 20 w/v% in PBS.

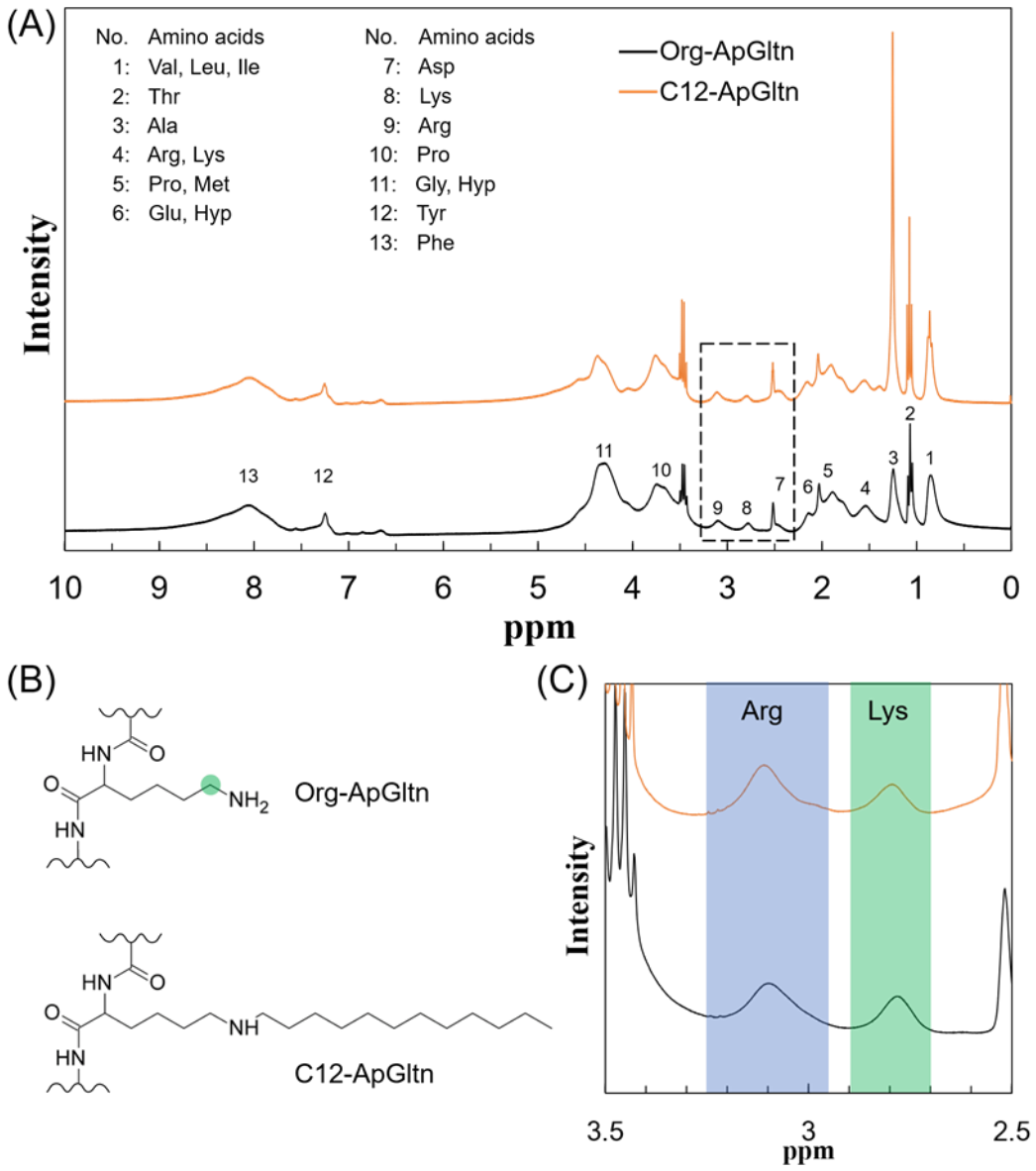

Figure A-3. Characterizations of Org- and C12-ApGltn
(A) ^{1}H-NMR spectra of Org- and C12-ApGltn with identification of amino acids. (B) The structural change before and after the synthesis. ε-methylene of lysine in gelatin was highlighted in green. (C) The magnified spectra of dashed box in (A). Blue area indicated Arg peak, which integration was utilized as normalized peak for each spectrum. The integra of ε-methylene of lysine in gelatin (Green highlighted) was decreased by the modification of dodecyl group.

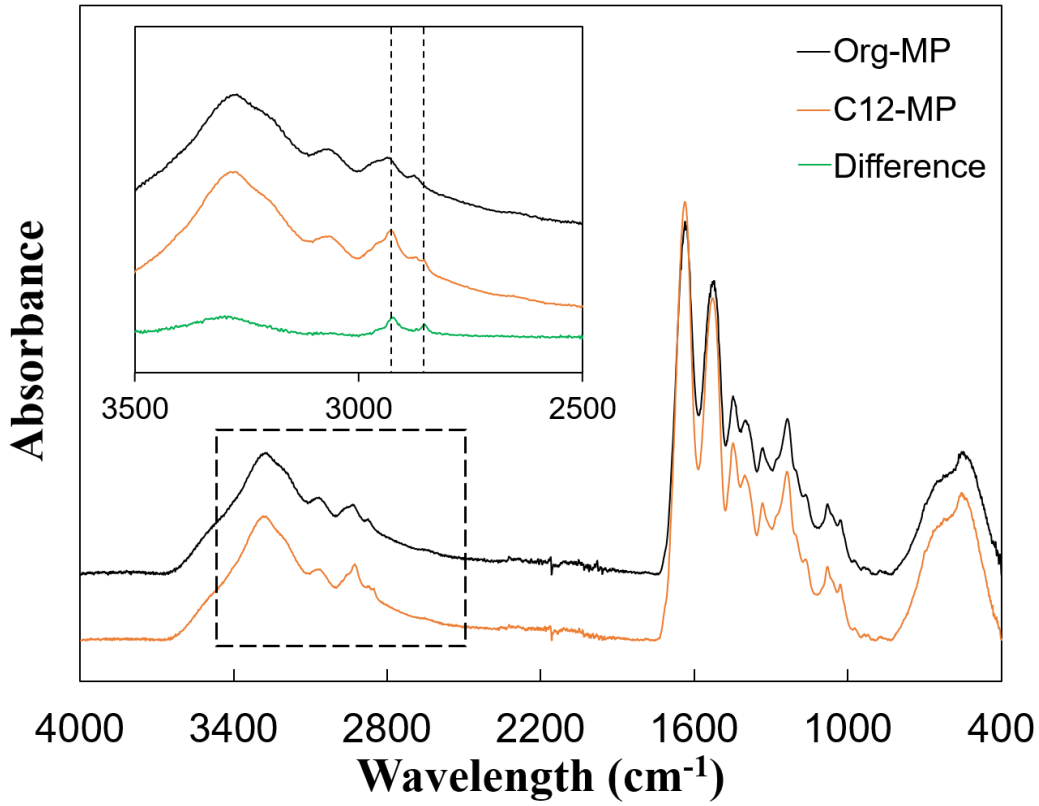

Figure A-4. FT-IR spectra of Org- and C12-MP.
Inset: magnified region in dotted line and the absorbance difference of Org- and C12-MP.

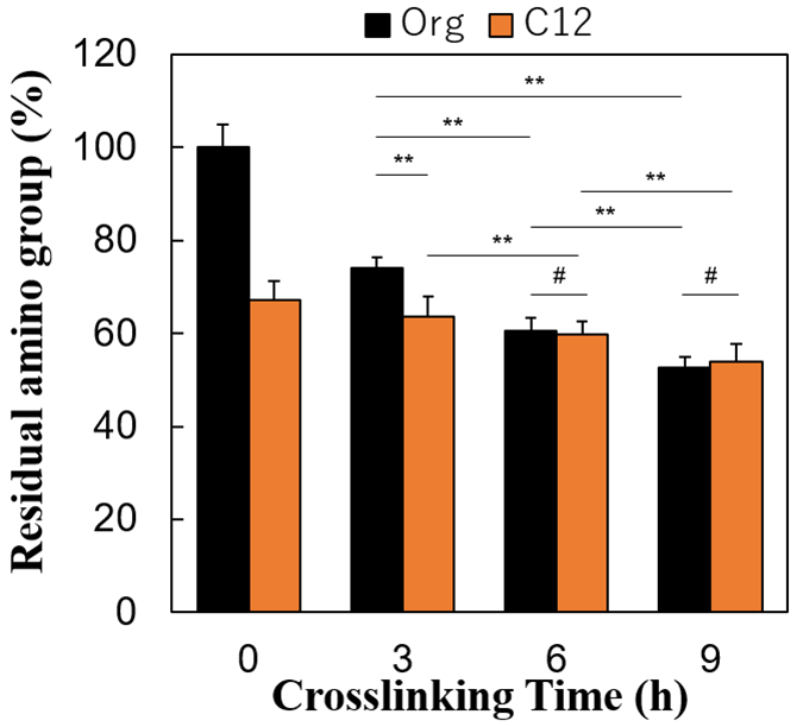

Figure A-5. Residual amino group in Org-MP and C12-MP after the thermal crosslinking.
The residual amino group of C12-MP without thermal crosslinking was correlated with C12-ApGltn (33 mol% modification ratio. *$p<0.05$, **$p<0.01$, $^{\#}p>0.05$

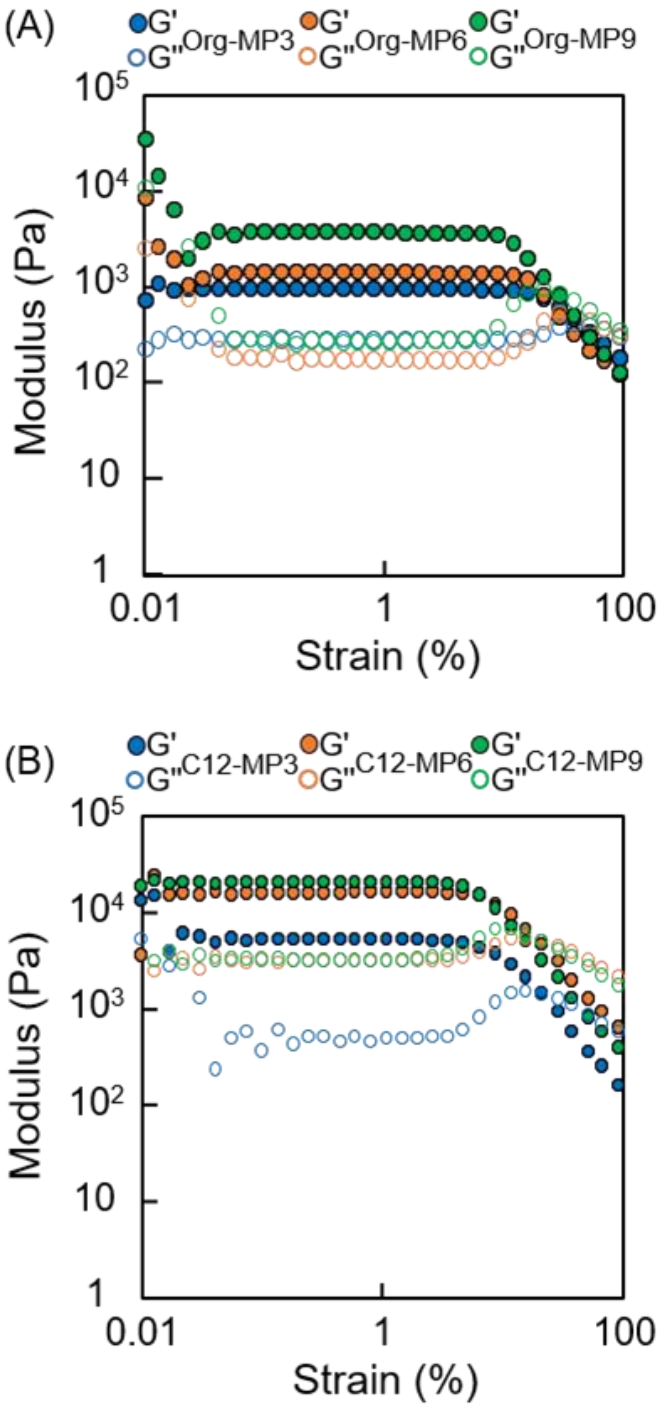

Figure A-6. Strain sweep measurements of (A) Org-MP hydrogels and (B) C12-MP hydrogels. Strain at 1 Hz was within the LVE region

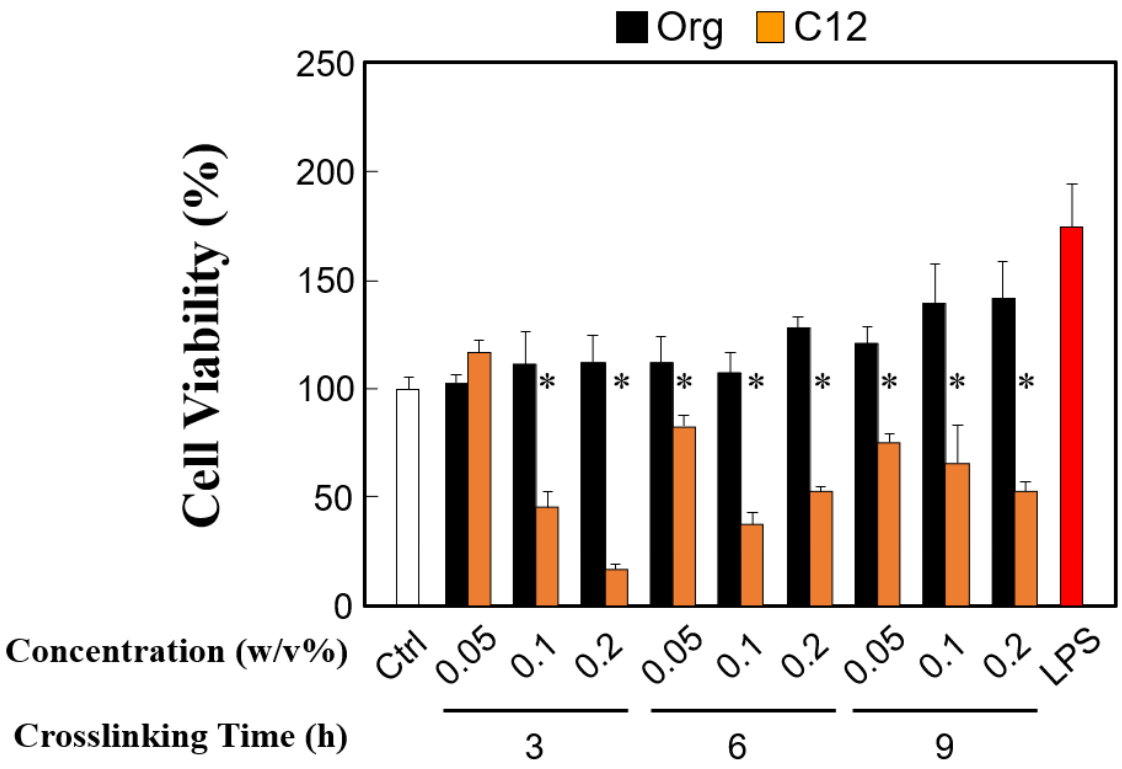

Figure A-7. The effect of Org- and C12-MP on cell viability with various crosslinking time.
The viability of TCPS control (Ctrl) was defined as 100 % viability. * indicates significant decrease in viability compared with Ctrl. *p<0.05.

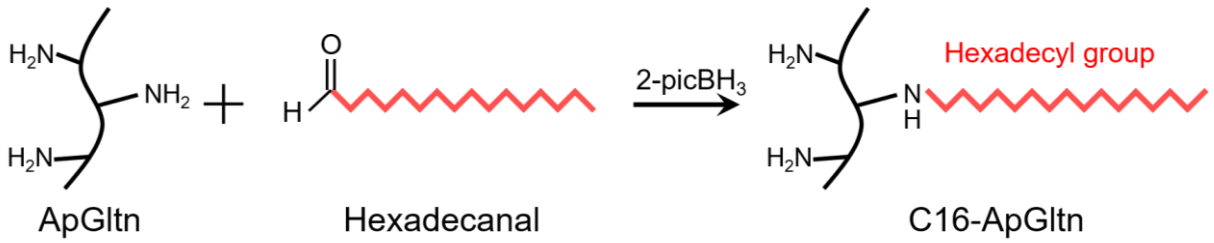

Figure A-8. Synthesis of C16-ApGltn by reductive amination.

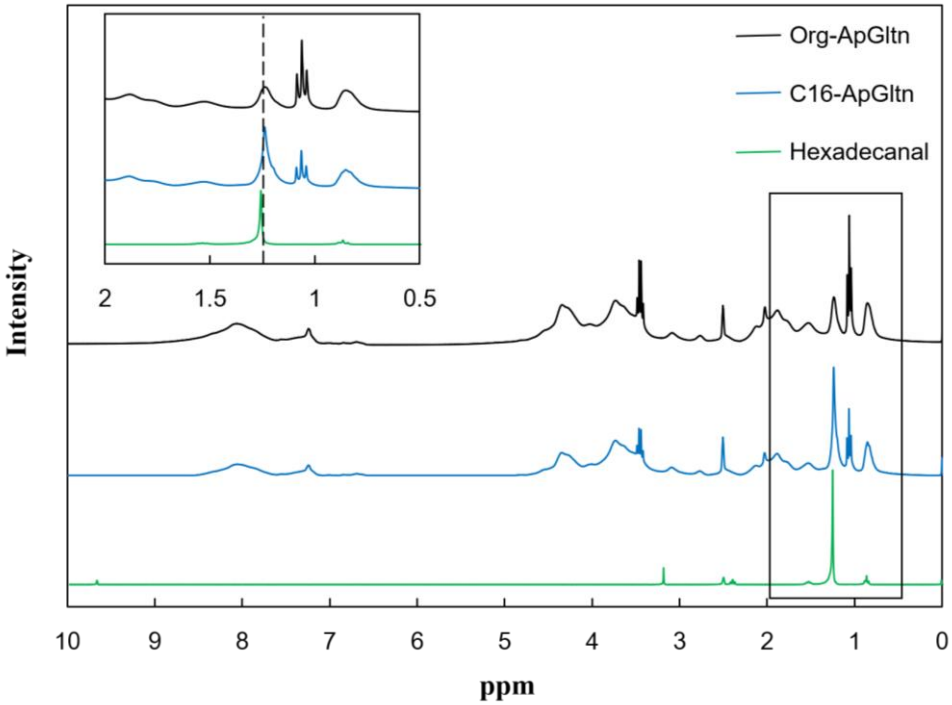

Figure A-9. ^{1}H-NMR spectra of Org- and C16-ApGltn.

The inset graph indicates the magnified spectra of the boxed region.

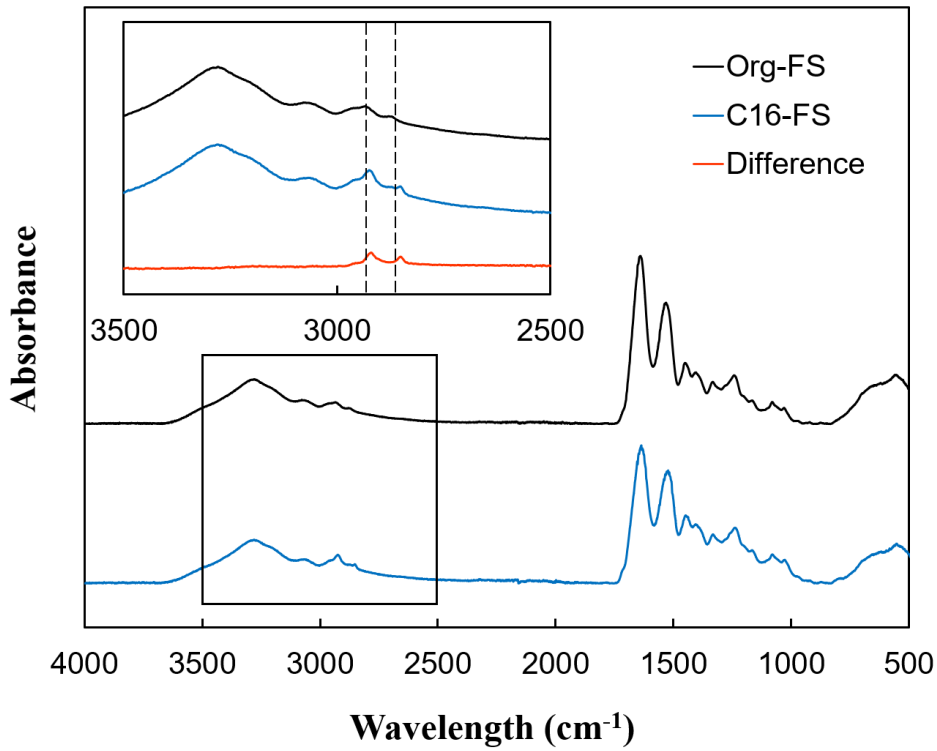

Figure A-10. FT-IR spectra of Org- and C16-FS.

(inset : magnified region in boxed area and the absorbance difference of Org- and C16-FS.)

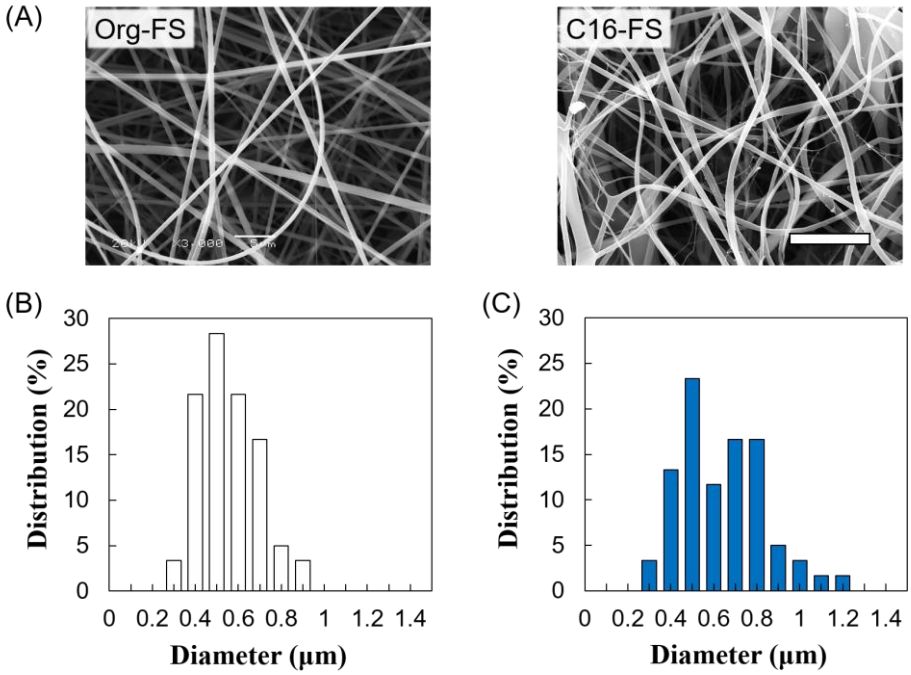

Figure A-11. The microstructure observation of FSs.

(A) SEM observation of Org- and C16-FS after the thermal crosslinking. (x3000) Scale bar = 5 μm. The fiber diameter histograms of (B) Org- and (C) C16-FS measured by Image J. (n=60).

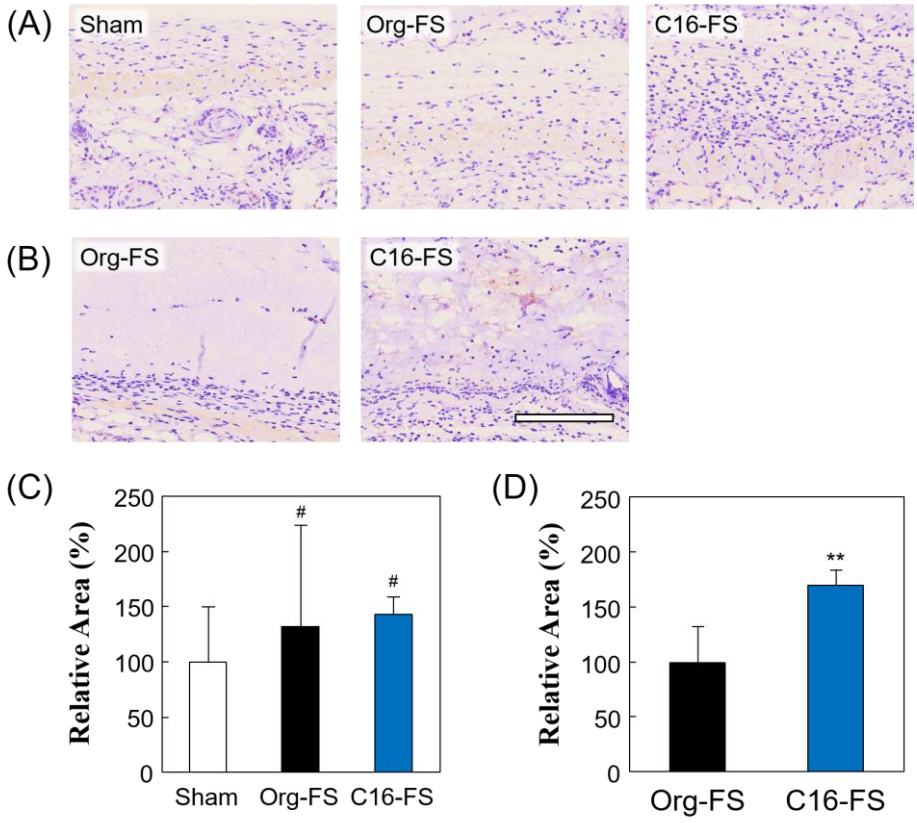

Figure A-12. Immunohistochemical observations after the in vivo experiments.

Evaluation of immunohistochemical expression of VEGF in (A) tissue and (B) FSs 3 days after the implantation of Org- and C16-FS. Scale bar = 200 μm. The VEGF expressed area in tissue and FSs was shown in (C) and (D), respectively. (n=10) $^{\#}p>0.05$, $^{**}p<0.01$.

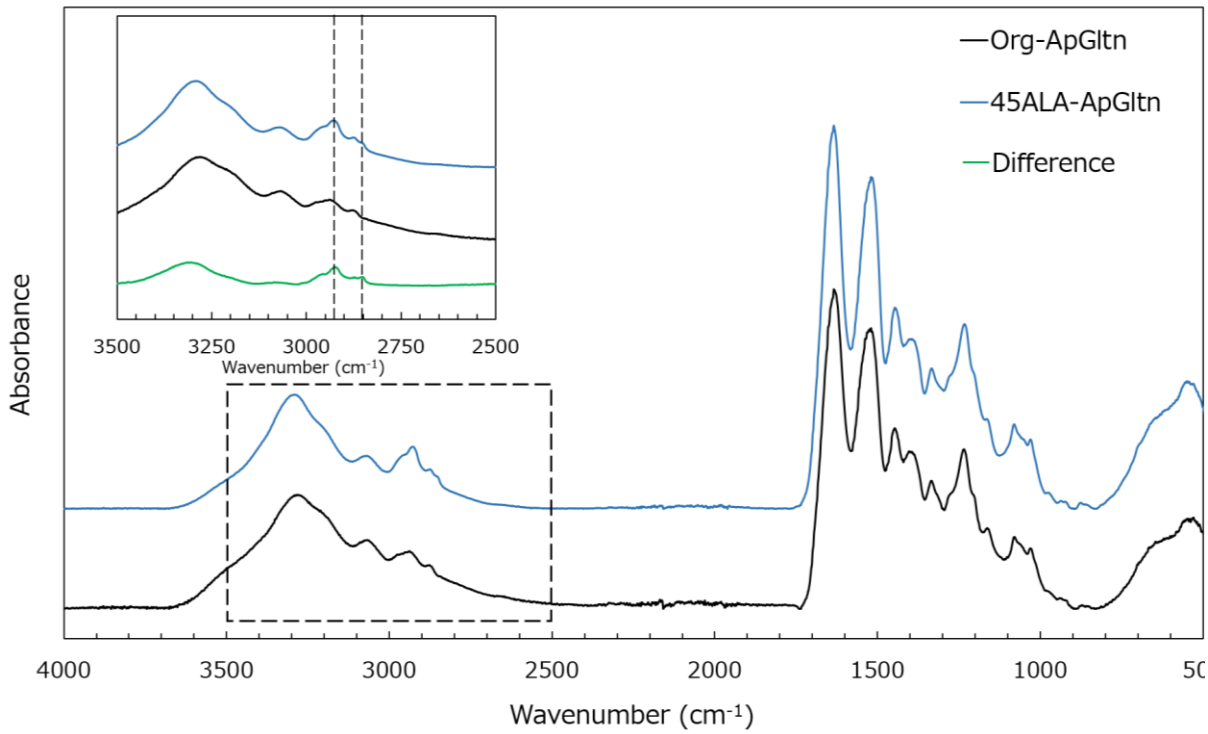

Figure A-13. FT-IR spectra of Org- and ALA-ApGltn.

The spectra inset indicates the magnified region of the dashed box.

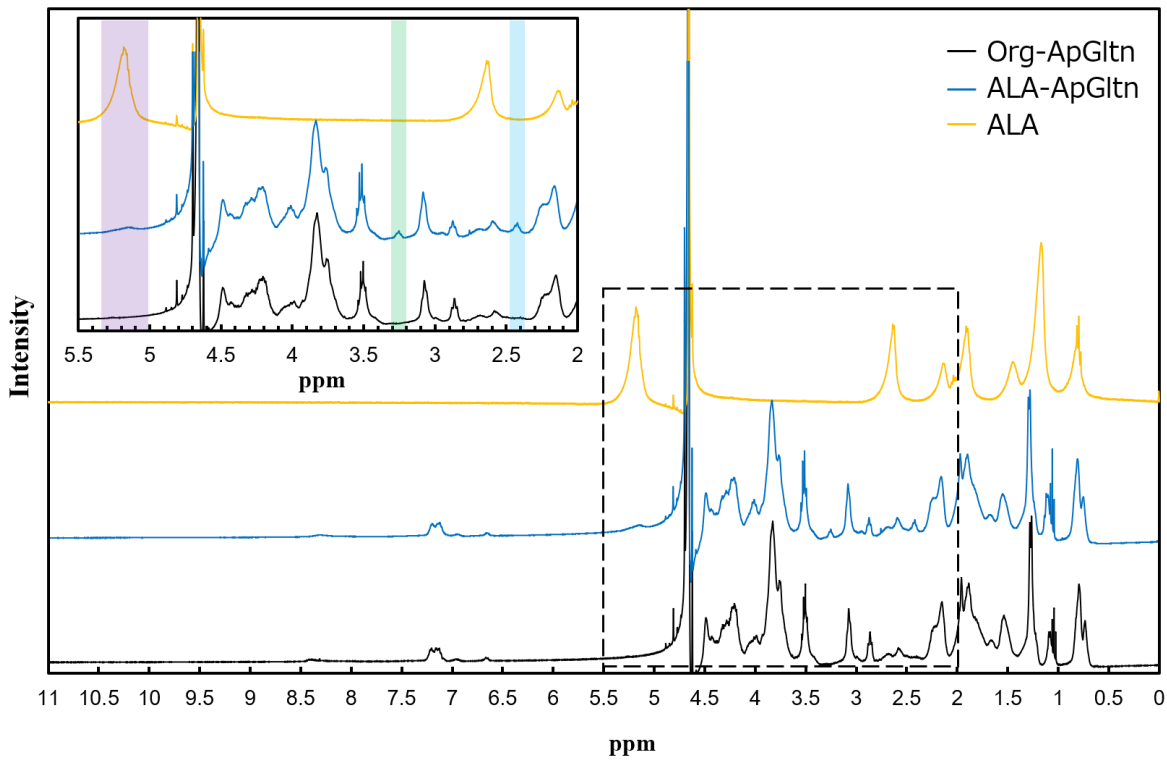

Figure A-14. ^{1}H-NMR spectra of ALA, Org- and ALA-ApGltn.

The inset shows the extended region of the dashed box.

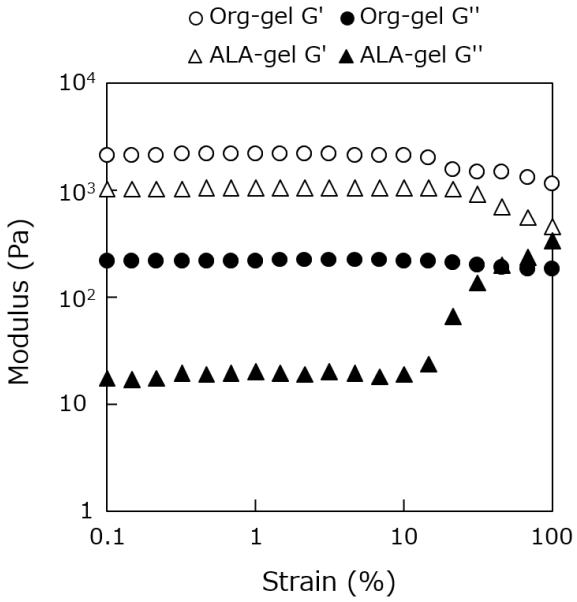

Figure A-15. Strain sweep measurement of Org- and ALA-gel.
Strain at 1% was within the LVE region and employed for the frequency sweep measurement.

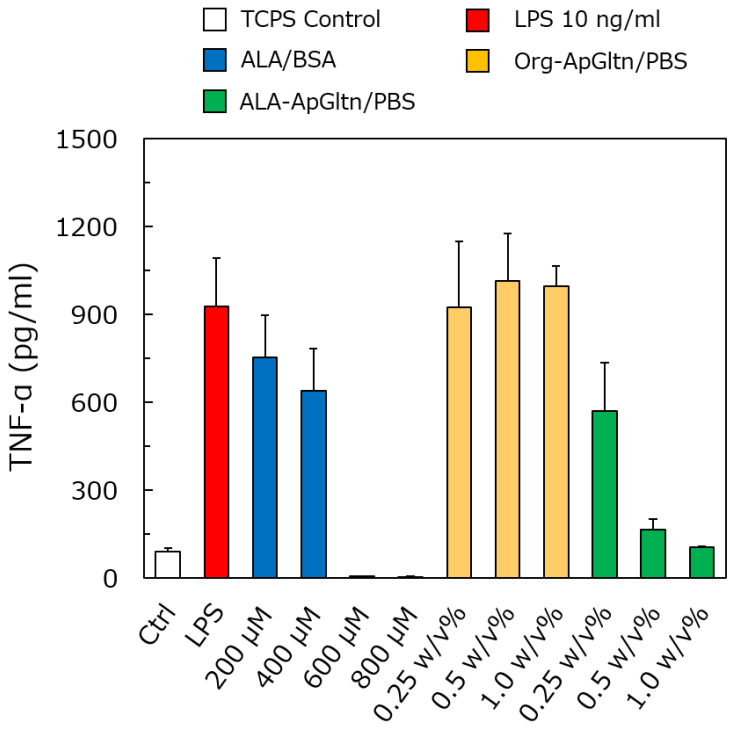

Figure A-16. The concentration of secreted TNF-α from RAW264.7.
The concentration of ALA/BSA complex and Org-/ALA-ApGltn indicated the molarity of ALA moieties and ApGltn concentration in PBS, respectively.

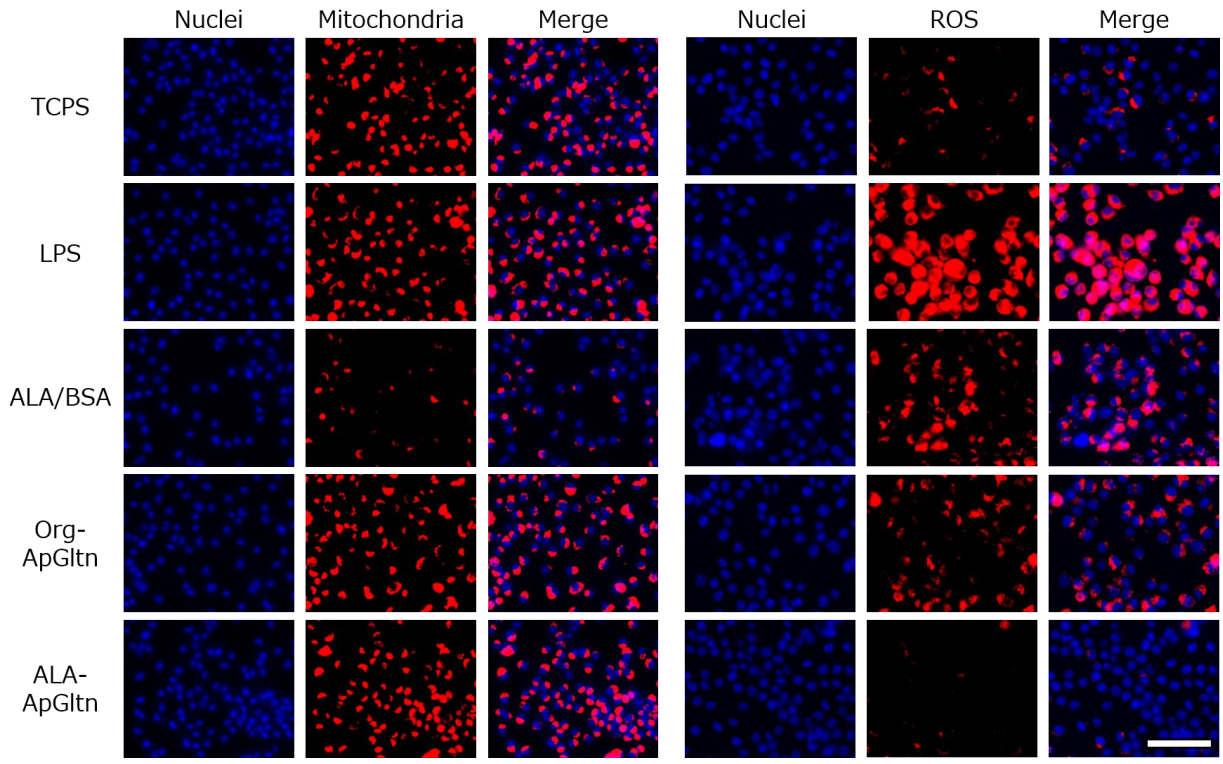

Figure A-17. Separated images of mitochondrial and ROS staining.

Scale bar = 100 μm.

References

1. Eming, S. A., Krieg, T. & Davidson, J. M. Inflammation in Wound Repair: Molecular and Cellular Mechanisms. *J. Invest. Dermatol.* **127**, 514–525 (2007).
2. Koh, T. J. & DiPietro, L. A. Inflammation and wound healing: the role of the macrophage. *Expert Rev. Mol. Med.* **13**, e23 (2011).
3. Ferrante, C. J. & Leibovich, S. J. Regulation of Macrophage Polarization and Wound Healing. *Adv. Wound Care* **1**, 10–16 (2012).
4. Wahl, S. M., Wong, H. & McCartney-Francis, N. Role of growth factors in inflammation and repair. *J. Cell. Biochem.* **40**, 193–199 (1989).
5. Shaw, T. J. & Martin, P. Wound repair at a glance. *J. Cell Sci.* **122**, 3209 LP – 3213 (2009).
6. Singer, A. J. & Clark, R. A. F. Cutaneous Wound Healing. *N. Engl. J. Med.* **341**, 738–746 (1999).
7. Deonarine, K. *et al.* Gene expression profiling of cutaneous wound healing. *J. Transl. Med.* **5**, 11 (2007).
8. Monteiro, S., Salgado, A. & Silva, N. Immunomodulation as a neuroprotective strategy after spinal cord injury. *Neural Regen. Res.* **13**, 423–424 (2018).
9. Tonnesen, M. G., Feng, X. & Clark, R. A. F. Angiogenesis in wound healing. *J. Investig. Dermatology Symp. Proc.* **5**, 40–46 (2000).
10. Castilla, D. M., Liu, Z.-J. & Velazquez, O. C. Oxygen: Implications for Wound Healing. *Adv. Wound Care* **1**, 225–230 (2012).
11. Hunt, T. K., Zederfeldt, B. & Goldstick, T. K. Oxygen and healing. *Am. J. Surg.* **118**, 521–525 (1969).
12. Kanno, E. *et al.* Wound healing in skin promoted by inoculation with Pseudomonas aeruginosa PAO1: The critical role of tumor necrosis factor-α secreted from infiltrating neutrophils. *Wound Repair Regen.* **19**, 608–621 (2011).
13. Matsumoto, S. *et al.* Insulin independence after living-donor distal pancreatectomy and islet allotransplantation. *Lancet* **365**, 1642–1644 (2005).
14. Iwanaga, Y. *et al.* Living Donor Islet Transplantation, the Alternative Approach to Overcome the Obstacles Limiting Transplant. *Ann. N. Y. Acad. Sci.* **1079**, 335–339 (2006).
15. Shapiro, A. M. J. *et al.* Islet Transplantation in Seven Patients with Type 1 Diabetes Mellitus Using a Glucocorticoid-Free Immunosuppressive Regimen. *N. Engl. J. Med.* **343**, 230–238 (2000).
16. Segers, V. F. M. & Lee, R. T. Stem-cell therapy for cardiac disease. *Nature* **451**, 937–942 (2008).
17. Abdel-Latif, A. *et al.* Adult Bone Marrow–Derived Cells for Cardiac Repair: A Systematic Review and Meta-analysis. *Arch. Intern. Med.* **167**, 989–997 (2007).
18. Sandra, E. *et al.* Restoration of Microvascular Function in the Infarct-Related Artery by Intracoronary Transplantation of Bone Marrow Progenitor Cells in Patients With Acute Myocardial Infarction. *Circulation* **116**, 366–374 (2007).
19. Miyahara, Y. *et al.* Monolayered mesenchymal stem cells repair scarred myocardium after myocardial infarction. *Nat. Med.* **12**, 459–465 (2006).
20. Nussbaum, J. *et al.* Transplantation of undifferentiated murine embryonic stem cells in the

heart: teratoma formation and immune response. *FASEB J.* **21**, 1345–1357 (2007).
21. Winter, E. M. *et al.* Preservation of left ventricular function and attenuation of remodeling after transplantation of human epicardium-derived cells into the infarcted mouse heart. *Circulation* **116**, 917–927 (2007).
22. Bearzi, C. *et al.* Human cardiac stem cells. *Proc. Natl. Acad. Sci. U. S. A.* **104**, 14068–14073 (2007).
23. Mattsson, G., Jansson, L. & Carlsson, P. O. Decreased vascular density in mouse pancreatic islets after transplantation. *Diabetes* **51**, 1362–1366 (2002).
24. Jansson, L. & Carlsson, P. O. Graft vascular function after transplantation of pancreatic islets. *Diabetologia* **45**, 749–763 (2002).
25. Menger, M. D. *et al.* Angiogenesis and Hemodynamics of Microvasculature of Transplanted Islets of Langerhans. *Diabetes* **38**, 199 LP – 201 (1989).
26. Laflamme, M. A. & Murry, C. E. Regenerating the heart. *Nat. Biotechnol.* **23**, 845–856 (2005).
27. Menasché, P. Skeletal Myoblasts as a Therapeutic Agent. *Prog. Cardiovasc. Dis.* **50**, 7–17 (2007).
28. C., W. K. & Helmut, D. Clinical Applications of Stem Cells for the Heart. *Circ. Res.* **96**, 151–163 (2005).
29. Selden, C., Gupta, S., Johnstone, R. & Hodgson, H. J. F. The pulmonary vascular bed as a site for implantation of isolated liver cells in inbred rats. *Transplantation* **38**, 81–83 (1984).
30. Dolmans, M. M. *et al.* Impact of the cryopreservation technique and vascular bed on ovarian tissue transplantation in cynomolgus monkeys. *J. Assist. Reprod. Genet.* **32**, 1251–1262 (2015).
31. Dvir, T. *et al.* Prevascularization of cardiac patch on the omentum improves its therapeutic outcome. *Proc. Natl. Acad. Sci.* **106**, 14990 LP – 14995 (2009).
32. Liu, W. *et al.* Microcryogels as injectable 3-D cellular microniches for site-directed and augmented cell delivery. *Acta Biomater.* **10**, 1864–1875 (2014).
33. Van Eyck, A. S. *et al.* Both host and graft vessels contribute to revascularization of xenografted human ovarian tissue in a murine model. *Fertil. Steril.* **93**, 1676–1685 (2010).
34. Malecki, M., Kolsut, P. & Proczka, R. Angiogenic and antiangiogenic gene therapy. *Gene Ther.* **12**, S159–S169 (2005).
35. Abhinand, C. S., Raju, R., Soumya, S. J., Arya, P. S. & Sudhakaran, P. R. VEGF-A/VEGFR2 signaling network in endothelial cells relevant to angiogenesis. *J. Cell Commun. Signal.* **10**, 347–354 (2016).
36. Carmeliet, P. & Jain, R. K. Molecular mechanisms and clinical applications of angiogenesis. *Nature* **473**, 298–307 (2011).
37. Klint, P., Kanda, S., Kloog, Y. & Claesson-Welsh, L. Contribution of Src and Ras pathways in FGF-2 induced endothelial cell differentiation. *Oncogene* **18**, 3354–3364 (1999).
38. Seghezzi, G. *et al.* Fibroblast growth factor-2 (FGF-2) induces vascular endothelial growth factor (VEGF) expression in the endothelial cells of forming capillaries: An autocrine mechanism contributing to angiogenesis. *J. Cell Biol.* **141**, 1659–1673 (1998).
39. T., S. G., C., Z. I., A., B. P., F., M. J. & D., E. J. Basic Fibroblast Growth Factor Upregulates the Expression of Vascular Endothelial Growth Factor in Vascular Smooth Muscle Cells .

Circulation **92**, 11–14 (1995).

40. Claffey, K. P. *et al.* Fibroblast Growth Factor 2 Activation of Stromal Cell Vascular Endothelial Growth Factor Expression and Angiogenesis. *Lab. Investig.* **81**, 61–75 (2001).
41. Schöllmann, C. *et al.* Basic fibroblast growth factor modulates the mitogenic potency of the platelet-derived growth factor (PDGF) isoforms by specific upregulation of the PDGF alpha receptor in vascular smooth muscle cells. *J. Biol. Chem.* **267**, 18032–18039 (1992).
42. Mitsuho, O. *et al.* Fibroblast Growth Factor-2 Gene Transfer Can Stimulate Hepatocyte Growth Factor Expression Irrespective of Hypoxia-Mediated Downregulation in Ischemic Limbs. *Circ. Res.* **91**, 923–930 (2002).
43. Smith, M. K., Peters, M. C., Richardson, T. P., Garbern, J. C. & Mooney, D. J. Locally Enhanced Angiogenesis Promotes Transplanted Cell Survival. *Tissue Eng.* **10**, 63–71 (2004).
44. Kawakami, Y. *et al.* Successful Subcutaneous Pancreatic Islet Transplantation Using an Angiogenic Growth Factor–Releasing Device. *Pancreas* **23**, (2001).
45. Fan, C. *et al.* Myocardial-Infarction-Responsive Smart Hydrogels Targeting Matrix Metalloproteinase for On-Demand Growth Factor Delivery. *Adv. Mater.* **31**, 1902900 (2019).
46. Nih, L. R., Gojgini, S., Carmichael, S. T. & Segura, T. Dual-function injectable angiogenic biomaterial for the repair of brain tissue following stroke. *Nat. Mater.* **17**, 642–651 (2018).
47. Jeffrey T. Lu, M. A. C. The Relationship of Cigarette Smoking to Peripheral Arterial Disease. *Reviews in Cardiovascular Medicine* vol. 5 189–193.
48. Qadura, M., Terenzi, D. C., Verma, S., Al-Omran, M. & Hess, D. A. Concise Review: Cell Therapy for Critical Limb Ischemia: An Integrated Review of Preclinical and Clinical Studies. *Stem Cells* **36**, 161–171 (2018).
49. Conte, M. S. *et al.* Society for Vascular Surgery practice guidelines for atherosclerotic occlusive disease of the lower extremities: Management of asymptomatic disease and claudication. *J. Vasc. Surg.* **61**, 2S-41S.e1 (2015).
50. Marui, A. *et al.* A novel approach to therapeutic angiogenesis for patients with critical limb ischemia by sustained release of basic fibroblast growth factor using biodegradable gelatin hydrogel - An initial report of the phase I-IIa study. *Circ. J.* **71**, 1181–1186 (2007).
51. M., I. J. *et al.* Arterial Gene Therapy for Therapeutic Angiogenesis in Patients With Peripheral Artery Disease. *Circulation* **91**, 2687–2692 (1995).
52. Amsden, B. Novel biodegradable polymers for local growth factor delivery. *Eur. J. Pharm. Biopharm.* **97**, 318–328 (2015).
53. Chen, G., Gulbranson, D. R., Yu, P., Hou, Z. & Thomson, J. A. Thermal Stability of Fibroblast Growth Factor Protein Is a Determinant Factor in Regulating Self-Renewal, Differentiation, and Reprogramming in Human Pluripotent Stem Cells. *Stem Cells* **30**, 623–630 (2012).
54. Lazarous, D. F. *et al.* Comparative effects of basic fibroblast growth factor and vascular endothelial growth factor on coronary collateral development and the arterial response to injury. *Circulation* **94**, 1074–1082 (1996).
55. Laham, R. J., Rezaee, M., Post, M., Xu, X. & Sellke, F. W. Intrapericardial administration of basic fibroblast growth factor: Myocardial and tissue distribution and comparison with intracoronary and intravenous administration. *Catheter. Cardiovasc. Interv.* **58**, 375–381 (2003).

56. Lundstrom, K. Viral Vectors in Gene Therapy. *Diseases* vol. 6 (2018).
57. Feng, Y. *et al.* A macrophage-activating, injectable hydrogel to sequester endogenous growth factors for in situ angiogenesis. *Biomaterials* **134**, 128–142 (2017).
58. Yang, C. *et al.* Stimulation of osteogenesis and angiogenesis by micro/nano hierarchical hydroxyapatite via macrophage immunomodulation. *Nanoscale* **11**, 17699–17708 (2019).
59. Hong, L. T. A. *et al.* An injectable hydrogel enhances tissue repair after spinal cord injury by promoting extracellular matrix remodeling. *Nat. Commun.* **8**, 533 (2017).
60. Zhang, J.-M. & An, J. Cytokines, Inflammation, and Pain. *Int. Anesthesiol. Clin.* **45**, 27–37 (2007).
61. Durant, S., Duval, D. & Homo-Delarche, F. Effect of exogenous prostaglandins and nonsteroidal anti-inflammatory agents on prostaglandin secretion and proliferation of mouse embryo fibroblasts in culture. *Prostaglandins, Leukot. Essent. Fat. Acids* **38**, 1–8 (1989).
62. Futagami, A., Ishizaki, M., Fukuda, Y., Kawana, S. & Yamanaka, N. Wound healing involves induction of cyclooxygenase-2 expression in rat skin. *Lab. Investig.* **82**, 1503–1513 (2002).
63. Jeschke, M. G. *et al.* Burn injury. *Nat. Rev. Dis. Prim.* **6**, 11 (2020).
64. Sun, L. T. *et al.* Reduction of burn progression with topical delivery of (antitumor necrosis factor-α)-hyaluronic acid conjugates. *Wound Repair Regen.* **20**, 563–572 (2012).
65. Parihar, A., Parihar, M. S., Milner, S. & Bhat, S. Oxidative stress and anti-oxidative mobilization in burn injury. *Burns* **34**, 6–17 (2008).
66. Haycock, J. W., Ralston, D. R., Morris, B., Freedlander, E. & MacNeil, S. Oxidative damage to protein and alterations to antioxidant levels in human cutaneous thermal injury. *Burns* **23**, 533–540 (1997).
67. Till, G. O., Hatherill, J. R., Tourtellotte, W. W., Lutz, M. J. & Ward, P. A. Lipid peroxidation and acute lung injury after thermal trauma to skin. Evidence of a role for hydroxyl radical. *Am. J. Pathol.* **119**, 376–384 (1985).
68. TILL, G. O. *et al.* Oxygen Radical Dependent Lung Damage following Thermal Injury of Rat Skin. *J. Trauma Acute Care Surg.* **23**, (1983).
69. Gürbüz, V., Corak, A., Yeğen, B. C., Kurtel, H. & Alican, I. Oxidative organ damage in a rat model of thermal injury: the effect of cyclosporin A. *Burns* **23**, 37–42 (1997).
70. Zheng, Y. *et al.* Injectable supramolecular gelatin hydrogel loading of resveratrol and histatin-1 for burn wound therapy. *Biomater. Sci.* **8**, 4810–4820 (2020).
71. Friedrich, E. E. *et al.* Effects of hyaluronic acid conjugation on anti-TNF-α inhibition of inflammation in burns. *J. Biomed. Mater. Res. - Part A* **102**, 1527–1536 (2014).
72. Ito, T. *et al.* Anti-inflammatory function of an in situ cross-linkable conjugate hydrogel of hyaluronic acid and dexamethasone. *Biomaterials* **28**, 1778–1786 (2007).
73. Chumsae, C., Gaza-Bulseco, G., Sun, J. & Liu, H. Comparison of methionine oxidation in thermal stability and chemically stressed samples of a fully human monoclonal antibody. *J. Chromatogr. B Anal. Technol. Biomed. Life Sci.* **850**, 285–294 (2007).
74. Correia, I. R. Stability of IgG isotypes in serum. *MAbs* **2**, 221–232 (2010).
75. Hermeling, S., Crommelin, D. J. A., Schellekens, H. & Jiskoot, W. Structure-immunogenicity relationships of therapeutic proteins. *Pharm. Res.* **21**, 897–903 (2004).
76. Liu, D. *et al.* Structure and stability changes of human IgG1 Fc as a consequence of

methionine oxidation. *Biochemistry* **47**, 5088–5100 (2008).
77. Deane, K. D. & Holers, V. M. The Natural History of Rheumatoid Arthritis. *Clin. Ther.* **41**, 1256–1269 (2019).
78. Aletaha, D. *et al.* 2010 Rheumatoid arthritis classification criteria: An American College of Rheumatology/European League Against Rheumatism collaborative initiative. *Arthritis Rheum.* **62**, 2569–2581 (2010).
79. Maini, R. N. & Taylor, P. C. Anti-Cytokine Therapy for Rheumatoid Arthritis. *Annu. Rev. Med.* **51**, 207–229 (2000).
80. Feldmann, M. & Maini, R. N. Anti-TNFα Therapy of Rheumatoid Arthritis: What Have We Learned? *Annu. Rev. Immunol.* **19**, 163–196 (2001).
81. Ishihara, K. & Hirano, T. IL-6 in autoimmune disease and chronic inflammatory proliferative disease. *Cytokine Growth Factor Rev.* **13**, 357–368 (2002).
82. Ghosh, P. & Guidolin, D. Potential mechanism of action of intra-articular hyaluronan therapy in osteoarthritis: Are the effects molecular weight dependent? *Semin. Arthritis Rheum.* **32**, 10–37 (2002).
83. Zhang, Z., Barman, S. & Christopher, G. F. The role of protein content on the steady and oscillatory shear rheology of model synovial fluids. *Soft Matter* **10**, 5965–5973 (2014).
84. Smolen, J. S. & Steiner, G. Therapeutic strategies for rheumatoid arthritis. *Nat. Rev. Drug Discov.* **2**, 473–488 (2003).
85. Bang, J. S. *et al.* Anti-inflammatory and antiarthritic effects of piperine in human interleukin 1β-stimulated fibroblast-like synoviocytes and in rat arthritis models. *Arthritis Res. Ther.* **11**, R49 (2009).
86. Barnes, P. J., Adcock, I., Spedding, M. & Vanhoutte, P. M. Anti-inflammatory actions of steroids: molecular mechanisms. *Trends Pharmacol. Sci.* **14**, 436–441 (1993).
87. Kim, K. S. *et al.* Injectable hyaluronic acid–tyramine hydrogels for the treatment of rheumatoid arthritis. *Acta Biomater.* **7**, 666–674 (2011).
88. Lo, G. H., LaValley, M., McAlindon, T. & Felson, D. T. Intra-articular Hyaluronic Acid in Treatment of Knee OsteoarthritisA Meta-analysis. *JAMA* **290**, 3115–3121 (2003).
89. Cai, Z., Zhang, H., Wei, Y., Wu, M. & Fu, A. Shear-thinning hyaluronan-based fluid hydrogels to modulate viscoelastic properties of osteoarthritis synovial fluids. *Biomater. Sci.* **7**, 3143–3157 (2019).
90. Heo, J. *et al.* Riboflavin-induced photo-crosslinking of collagen hydrogel and its application in meniscus tissue engineering. *Drug Deliv. Transl. Res.* **6**, 148–158 (2016).
91. Lee, H.-R., Park, K. M., Joung, Y. K., Park, K. D. & Do, S. H. Platelet-rich plasma loaded hydrogel scaffold enhances chondrogenic differentiation and maturation with up-regulation of CB1 and CB2. *J. Control. Release* **159**, 332–337 (2012).
92. Lin, H., Cheng, A. W.-M., Alexander, P. G., Beck, A. M. & Tuan, R. S. Cartilage Tissue Engineering Application of Injectable Gelatin Hydrogel with In Situ Visible-Light-Activated Gelation Capability in Both Air and Aqueous Solution. *Tissue Eng. Part A* **20**, 2402–2411 (2014).
93. Nagase, K. *et al.* Local Release of VEGF Using Fiber Mats Enables Effective Transplantation of Layered Cardiomyocyte Sheets. *Macromol. Biosci.* **17**, 1700073 (2017).
94. Tabata, Y., Miyao, M., Ozeki, M. & Ikada, Y. Controlled release of vascular endothelial

growth factor by use of collagen hydrogels. *J. Biomater. Sci. Polym. Ed.* **11**, 915–930 (2000).
95. Uematsu, S. S. *et al.* The Optimization of the Prevascularization Procedures for Improving Subcutaneous Islet Engraftment. *Transplantation* **102**, 387–395 (2018).
96. Peattie, R. A. *et al.* Dual growth factor-induced angiogenesis in vivo using hyaluronan hydrogel implants. *Biomaterials* **27**, 1868–1875 (2006).
97. Yoshizawa, K., Mizuta, R. & Taguchi, T. Enhanced angiogenesis of growth factor-free porous biodegradable adhesive made with hexanoyl group-modified gelatin. *Biomaterials* **63**, 14–23 (2015).
98. Raetz, C. R. H. & Whitfield, C. Lipopolysaccharide Endotoxins. *Annu. Rev. Biochem.* **71**, 635–700 (2002).
99. Alexander, C. & Zähringer, U. Chemical structure of lipid A - The primary immunomodulatory center of bacterial lipopolysaccharides. *Trends Glycosci. Glycotechnol.* **14**, 69–86 (2002).
100. Li, X. & Qin, J. Modulation of Toll-interleukin 1 receptor mediated signaling. *J. Mol. Med.* **83**, 258–266 (2005).
101. Itaya, H. *et al.* Expression of vascular endothelial growth factor in human monocyte/macrophages stimulated with lipopolysaccharide. *Thromb. Haemost.* **85**, 171–176 (2001).
102. Kiriakidis, S. *et al.* VEGF expression in human macrophages is NF-κB-dependent: Studies using adenoviruses expressing the endogenous NF-κB inhibitor IκBα and a kinase-defective form of the IκB kinase 2. *J. Cell Sci.* **116**, 665–674 (2003).
103. Raetz, C. R. H. Biochemistry of Endotoxins. *Annu. Rev. Biochem.* **59**, 129–170 (1990).
104. Lee, J. Y. *et al.* Reciprocal modulation of toll-like receptor-4 signaling pathways involving MyD88 and phosphatidylinositol 3-kinase/AKT by saturated and polyunsaturated fatty acids. *J. Biol. Chem.* **278**, 37041–37051 (2003).
105. Wong, S. W. *et al.* Fatty acids modulate toll-like receptor 4 activation through regulation of receptor dimerization and recruitment into lipid rafts in a reactive oxygen species-dependent manner. *J. Biol. Chem.* **284**, 27384–27392 (2009).
106. Milanski, M. *et al.* Saturated fatty acids produce an inflammatory response predominantly through the activation of TLR4 signaling in hypothalamus: Implications for the pathogenesis of obesity. *J. Neurosci.* **29**, 359–370 (2009).
107. Huang, S. *et al.* Saturated fatty acids activate TLR-mediated proinflammatory signaling pathways. *J. Lipid Res.* **53**, 2002–2013 (2012).
108. Rocha, D. M., Caldas, A. P., Oliveira, L. L., Bressan, J. & Hermsdorff, H. H. Saturated fatty acids trigger TLR4-mediated inflammatory response. *Atherosclerosis* **244**, 211–215 (2016).
109. Wang, Y. *et al.* Saturated palmitic acid induces myocardial inflammatory injuries through direct binding to TLR4 accessory protein MD2. *Nat. Commun.* **8**, 13997 (2017).
110. Karim, A. A. & Bhat, R. Fish gelatin: properties, challenges, and prospects as an alternative to mammalian gelatins. *Food Hydrocoll.* **23**, 563–576 (2009).
111. Zhou, P., Mulvaney, S. J. & Regenstein, J. M. Properties of Alaska pollock skin gelatin: A comparison with tilapia and pork skin gelatins. *J. Food Sci.* **71**, C313–C321 (2006).
112. Mizuno, Y., Mizuta, R., Hashizume, M. & Taguchi, T. Enhanced sealing strength of a hydrophobically-modified Alaska pollock gelatin-based sealant. *Biomater. Sci.* **5**, 982–989

(2017).
113. Adler-Nissen, J. Determination of the Degree of Hydrolysis of Food Protein Hydrolysates by Trinitrobenzenesulfonic Acid. *J. Agric. Food Chem.* **27**, 1256–1262 (1979).
114. Satake, K., Okuyama, T., Ohashi, M. & Shinoda, T. * The TNBS , following abbreviations are used in this paper : *J. Biochem.* **47**, 654–660 (1960).
115. Habeeb, A. F. S. A. Determination of free amino groups in proteins by trinitrobenzenesulfonic acid. *Anal. Biochem.* **14**, 328–336 (1966).
116. Abdel-Magid, A. F., Carson, K. G., Harris, B. D., Maryanoff, C. A. & Shah, R. D. Reductive amination of aldehydes and ketones with sodium triacetoxyborohydride. Studies on direct and indirect reductive amination procedures. *J. Org. Chem.* **61**, 3849–3862 (1996).
117. Sato, S., Sakamoto, T., Miyazawa, E. & Kikugawa, Y. One-pot reductive amination of aldehydes and ketones with α-picoline-borane in methanol, in water, and in neat conditions. *Tetrahedron* **60**, 7899–7906 (2004).
118. Browning, M. B. & Cosgriff-Hernandez, E. Development of a biostable replacement for PEGDA hydrogels. *Biomacromolecules* **13**, 779–786 (2012).
119. Mizuno, Y. & Taguchi, T. Growth factor-free, angiogenic hydrogel based on hydrophobically modified Alaska pollock gelatin. *J. Tissue Eng. Regen. Med.* **13**, 2291–2299 (2019).
120. Himmelein, S., Lewe, V., Stuart, M. C. A. & Ravoo, B. J. A carbohydrate-based hydrogel containing vesicles as responsive non-covalent cross-linkers. *Chem. Sci.* **5**, 1054–1058 (2014).
121. Fields, G. B., Van Wart, H. E. & Birkedal-Hansen, H. Sequence specificity of human skin fibroblast collagenase. Evidence for the role of collagen structure in determining the collagenase cleavage site. *J. Biol. Chem.* **262**, 6221–6226 (1987).
122. Park, B. S. & Lee, J. O. Recognition of lipopolysaccharide pattern by TLR4 complexes. *Exp. Mol. Med.* **45**, e66 (2013).
123. Tondera, C. *et al.* Gelatin-based hydrogel degradation and tissue interaction in vivo: Insights from multimodal preclinical imaging in immunocompetent nude mice. *Theranostics* **6**, 2114–2128 (2016).
124. Ferrara, N., Gerber, H. P. & LeCouter, J. The biology of VEGF and its receptors. *Nat. Med.* **9**, 669–676 (2003).
125. Nishiguchi, A., Kurihara, Y. & Taguchi, T. Underwater-adhesive microparticle dressing composed of hydrophobically-modified Alaska pollock gelatin for gastrointestinal tract wound healing. *Acta Biomater.* **99**, 387–396 (2019).
126. Mizuno, Y. & Taguchi, T. Self-assembled dodecyl group-modified gelatin microparticle-based hydrogels with angiogenic properties. *NPG Asia Mater.* **12**, 48 (2020).
127. Okuyama, T. & Satake, K. On the preparation and properties of 2,4,6-trinitrophenyl-amino acids and -peptides. *J. Biochem.* **47**, 454–466 (1960).
128. Borch, R. F., Bernstein, M. D. & Durst, H. D. The Cyanohydridoborate Anion as a Selective Reducing Agent. *J. Am. Chem. Soc.* **93**, 2897–2904 (1971).
129. Borch, R. F. & Hassid, A. I. A New Method for the Methylation of Amines. *J. Org. Chem.* **37**, 1673–1674 (1972).
130. Mizuno, Y. & Taguchi, T. Promotion of Cell Migration into a Hydrophobically modified

Alaska Pollock Gelatin-Based Hydrogel. *Macromol. Biosci.* **19**, 1900083 (2019).
131. Patra, S., Basak, P. & Tibarewala, D. N. Synthesis of gelatin nano/submicron particles by binary nonsolvent aided coacervation (BNAC) method. *Mater. Sci. Eng. C* **59**, 310–318 (2016).
132. Qin, Z., Joo, J., Gu, L. & Sailor, M. J. Size control of porous silicon nanoparticles by electrochemical perforation etching. *Part. Part. Syst. Charact.* **31**, 252–256 (2014).
133. Kozlov, N. K. *et al.* Recycling of silicon: From industrial waste to biocompatible nanoparticles for nanomedicine. *Mater. Res. Express* **4**, 95026 (2017).
134. Zuidema, J. M., Rivet, C. J., Gilbert, R. J. & Morrison, F. A. A protocol for rheological characterization of hydrogels for tissue engineering strategies. *J. Biomed. Mater. Res. - Part B Appl. Biomater.* **102**, 1063–1073 (2014).
135. Browning, M. B., Cereceres, S. N., Luong, P. T. & Cosgriff-Hernandez, E. M. Determination of the in vivo degradation mechanism of PEGDA hydrogels. *J. Biomed. Mater. Res. - Part A* **102**, 4244–4251 (2014).
136. Lysakova-Devine, T. *et al.* Viral Inhibitory Peptide of TLR4, a Peptide Derived from Vaccinia Protein A46, Specifically Inhibits TLR4 by Directly Targeting MyD88 Adaptor-Like and TRIF-Related Adaptor Molecule. *J. Immunol.* **185**, 4261–4271 (2010).
137. Bernert, D. B., Isenbügel, K. & Ritter, H. Synthesis of a novel glycopeptide by polymeranalogous reaction of gelatin with mono-6-para-toluenesulfonyl-β-cyclodextrin and its supramolecular properties. *Macromol. Rapid Commun.* **32**, 397–403 (2011).
138. Rodin, V. V. & Izmailova, V. N. NMR method in the study of the interfacial adsorption layer of gelatin. *Colloids Surfaces A Physicochem. Eng. Asp.* **106**, 95–102 (1996).
139. Nakamura, H. & Ishii, M. Rheological behavior of concentrated monodispersed colloidal suspensions. *Nihon Reoroji Gakkaishi* **47**, 1–7 (2019).
140. Gelse, K., Pöschl, E. & Aigner, T. Collagens - Structure, function, and biosynthesis. *Adv. Drug Deliv. Rev.* **55**, 1531–1546 (2003).
141. Davidenko, N. *et al.* Evaluation of cell binding to collagen and gelatin: a study of the effect of 2D and 3D architecture and surface chemistry. *J. Mater. Sci. Mater. Med.* **27**, 148 (2016).
142. Nishiguchi, A. & Taguchi, T. Designing an anti-inflammatory and tissue-adhesive colloidal dressing for wound treatment. *Colloids Surfaces B Biointerfaces* **188**, 110737 (2020).
143. Pacheco, P., White, D. & Sulchek, T. Effects of Microparticle Size and Fc Density on Macrophage Phagocytosis. *PLoS One* **8**, e60989 (2013).
144. Aoki, S. *et al.* The efficacy of basic fibroblast growth factor-loaded poly(lactic-co-glycolic acid) nanosheet for mouse wound healing. *Wound Repair Regen.* **25**, 1008–1016 (2017).
145. Ueha, S., Shand, F. H. W. & Matsushima, K. Cellular and molecular mechanisms of chronic inflammation-associated organ fibrosis. *Front. Immunol.* **3**, 1–6 (2012).
146. Dulmovits, B. M. & Herman, I. M. Microvascular remodeling and wound healing: A role for pericytes. *Int. J. Biochem. Cell Biol.* **44**, 1800–1812 (2012).
147. Zhang, M. *et al.* Cardiomyocyte grafting for cardiac repair: Graft cell death and anti-death strategies. *J. Mol. Cell. Cardiol.* **33**, 907–921 (2001).
148. Kimura, Y. & Tabata, Y. Controlled release of stromal-cell-derived factor-1 from gelatin hydrogels enhances angiogenesis. *J. Biomater. Sci. Polym. Ed.* **21**, 37–51 (2010).
149. Pike, D. B. *et al.* Heparin-regulated release of growth factors in vitro and angiogenic

response in vivo to implanted hyaluronan hydrogels containing VEGF and bFGF. *Biomaterials* **27**, 5242–5251 (2006).

150. Brudno, Y., Ennett-Shepard, A. B., Chen, R. R., Aizenberg, M. & Mooney, D. J. Enhancing microvascular formation and vessel maturation through temporal control over multiple pro-angiogenic and pro-maturation factors. *Biomaterials* **34**, 9201–9209 (2013).
151. Elçin, Y. M., Dixit, V. & Gitnick, G. Extensive in vivo angiogenesis following controlled release of human vascular endothelial cell growth factor: Implications for tissue engineering and wound healing. *Artif. Organs* **25**, 558–565 (2001).
152. Nillesen, S. T. M. *et al.* Increased angiogenesis and blood vessel maturation in acellular collagen-heparin scaffolds containing both FGF2 and VEGF. *Biomaterials* **28**, 1123–1131 (2007).
153. Singh, S., Wu, B. M. & Dunn, J. C. Y. The enhancement of VEGF-mediated angiogenesis by polycaprolactone scaffolds with surface cross-linked heparin. *Biomaterials* **32**, 2059–2069 (2011).
154. Gainza, G., Villullas, S., Pedraz, J. L., Hernandez, R. M. & Igartua, M. Advances in drug delivery systems (DDSs) to release growth factors for wound healing and skin regeneration. *Nanomedicine Nanotechnology, Biol. Med.* **11**, 1551–1573 (2015).
155. Obara, K. *et al.* Acceleration of wound healing in healing-impaired db/db mice with a photocrosslinkable chitosan hydrogel containing fibroblast growth factor-2. *Wound Repair Regen.* **13**, 390–397 (2005).
156. Yu, A. *et al.* Wound dressing composed of hyaluronic acid and collagen containing EGF or bFGF: Comparative culture study. *J. Biomater. Sci. Polym. Ed.* **24**, 1015–1026 (2013).
157. Yuan, Z. *et al.* Injectable Citrate-Based Hydrogel as an Angiogenic Biomaterial Improves Cardiac Repair after Myocardial Infarction. *ACS Appl. Mater. Interfaces* **11**, 38429–38439 (2019).
158. Simons, M. *et al.* Clinical Trials in Coronary Angiogenesis: Issues, Problems, Consensus. *Circulation* **102**, e73–e86 (2000).
159. Kuijpers, A. J. *et al.* Cross-linking and characterisation of gelatin matrices for biomedical applications. *J. Biomater. Sci. Polym. Ed.* **11**, 225–243 (2000).
160. Kirchmajer, D. M., Watson, C. A., Ranson, M. & Panhuis, in het M. Gelapin, a degradable genipin cross-linked gelatin hydrogel. *RSC Adv.* **3**, 1073–1081 (2013).
161. Yung, C. W. *et al.* Transglutaminase crosslinked gelatin as a tissue engineering scaffold. *J. Biomed. Mater. Res. Part A* **83A**, 1039–1046 (2007).
162. Wisotzki, E. I. *et al.* Tailoring the material properties of gelatin hydrogels by high energy electron irradiation. *J. Mater. Chem. B* **2**, 4297–4309 (2014).
163. Hussain, A., Takahashi, K., Sonobe, J., Tabata, Y. & Bessho, K. Bone Regeneration of Rat Calvarial Defect by Magnesium Calcium Phosphate Gelatin Scaffolds with or without Bone Morphogenetic Protein-2. *J. Maxillofac. Oral Surg.* **13**, 29–35 (2014).
164. Campiglio, C. E., Negrini, N. C., Farè, S. & Draghi, L. Cross-linking strategies for electrospun gelatin scaffolds. *Materials (Basel).* **12**, 2476 (2019).
165. Prasertsung, I., Mongkolnavin, R., Kanokpanont, S. & Damrongsakkul, S. The effects of pulsed inductively coupled plasma (PICP) on physical properties and biocompatibility of crosslinked gelatin films. *Int. J. Biol. Macromol.* **46**, 72–78 (2010).

166. Gomes, S. R., Rodrigues, G., Martins, G. G., Henriques, C. M. R. & Silva, J. C. In vitro evaluation of crosslinked electrospun fish gelatin scaffolds. *Mater. Sci. Eng. C* **33**, 1219–1227 (2013).
167. Weiss, D. J. *et al.* Stem Cells and Cell Therapies in Lung Biology and Diseases: Conference Report. *Ann. Am. Thorac. Soc.* **10**, S25–S44 (2013).
168. Cosenza, V. A., Navarro, D. A. & Stortz, C. A. Usage of α-picoline borane for the reductive amination of carbohydrates. *Arkivoc* **2011**, 182–194 (2011).
169. Mizuno, Y. & Taguchi, T. A hydrophobic gelatin fiber sheet promotes secretion of endogenous vascular endothelial growth factor and stimulates angiogenesis. *RSC Adv.* **10**, 24800–24807 (2020).
170. Chiou, B. Sen *et al.* Fish Gelatin: Material Properties and Applications. in *Renewable Resources and Renewable Energy* (eds. Fornasiero, P. & Graziani, M.) 143 (Taylor & Francis, 2011). doi:10.1201/b16003.
171. Nagura, M., Yokota, H., Ikeura, M., Gotoh, Y. & Ohkoshi, Y. Structures and physical properties of cross-linked gelatin fibers. *Polym. J.* **34**, 761–766 (2002).
172. Valsaraj, K. T. Adsorption of polycyclic aromatic hydrocarbons at the air-water interface and its role in atmospheric deposition by fog droplets. *Environ. Toxicol. Chem.* **23**, 2318–2323 (2004).
173. Wang, S. *et al.* Controlled delivery of a protein tyrosine phosphatase inhibitor, SHP099, using cyclodextrin-mediated host-guest interactions in polyelectrolyte multilayer films for cancer therapy. *RSC Adv.* **10**, 20073–20082 (2020).
174. Matsuno, H. *et al.* The role of TNF-α in the pathogenesis of inflammation and joint destruction in rheumatoid arthritis (RA): A study using a human RA/SCID mouse chimera. *Rheumatology* **41**, 329–337 (2002).
175. Farrugia, M. & Baron, B. The role of TNF-α in rheumatoid arthritis: a focus on regulatory T cells. *J. Clin. Transl. Res.* **2**, 84–90 (2016).
176. Kohane, D. S. *et al.* Biodegradable polymeric microspheres and nanospheres for drug delivery in the peritoneum. *J. Biomed. Mater. Res. - Part A* **77**, 351–361 (2006).
177. Yeo, Y. *et al.* In situ cross-linkable hyaluronic acid hydrogels prevent post-operative abdominal adhesions in a rabbit model. *Biomaterials* **27**, 4698–4705 (2006).
178. Su, J., Hu, B. H., Lowe, W. L., Kaufman, D. B. & Messersmith, P. B. Anti-inflammatory peptide-functionalized hydrogels for insulin-secreting cell encapsulation. *Biomaterials* **31**, 308–314 (2010).
179. Im, D. S. Functions of omega-3 fatty acids and FFA4 (GPR120) in macrophages. *Eur. J. Pharmacol.* **785**, 36–43 (2016).
180. Kawano, A. *et al.* Docosahexaenoic acid enhances M2 macrophage polarization via the p38 signaling pathway and autophagy. *J. Cell. Biochem.* **120**, 12604–12617 (2019).
181. Ohue-Kitano, R. *et al.* A-Linolenic acid–derived metabolites from gut lactic acid bacteria induce differentiation of anti-inflammatory M2 macrophages through G protein-coupled receptor 40. *FASEB J.* **32**, 304–318 (2018).
182. Klein, E. & Weber, N. In vitro test for the effectiveness of antioxidants as inhibitors of thiyl radical-induced reactions with unsaturated fatty acids. *J. Agric. Food Chem.* **49**, 1224–1227 (2001).

183. Richard, D., Kefi, K., Barbe, U., Bausero, P. & Visioli, F. Polyunsaturated fatty acids as antioxidants. *Pharmacol. Res.* **57**, 451–455 (2008).
184. Mobraten, K., Haug, T. M., Kleiveland, C. R. & Lea, T. Omega-3 and omega-6 PUFAs induce the same GPR120-mediated signalling events, but with different kinetics and intensity in Caco-2 cells. *Lipids Health Dis.* **12**, 1–7 (2013).
185. Innes, J. K. & Calder, P. C. Omega-6 fatty acids and inflammation. *Prostaglandins Leukot. Essent. Fat. Acids* **132**, 41–48 (2018).
186. Iuchi, K., Ema, M., Suzuki, M., Yokoyama, C. & Hisatomi, H. Oxidized unsaturated fatty acids induce apoptotic cell death in cultured cells. *Mol. Med. Rep.* **19**, 2767–2773 (2019).
187. Kang, K. S. *et al.* Docosahexaenoic acid induces apoptosis in MCF-7 cells In Vitro and In Vivo via reactive oxygen species formation and caspase 8 activation. *PLoS One* **5**, e10296 (2010).
188. Begin, M. E., Ells, G. & Horrobin, D. F. Polyunsaturated fatty acid-induced cytotoxicity against tumor cells and its relationship to lipid peroxidation. *J. Natl. Cancer Inst.* **80**, 188–194 (1988).
189. Taguchi, T., Mizuta, R., Ito, T., Yoshizawa, K. & Kajiyama, M. Robust sealing of blood vessels with cholesteryl group-modified, alaska pollock-derived gelatin-based biodegradable sealant under wet conditions. *J. Biomed. Nanotechnol.* **12**, 128–134 (2016).
190. Mizuta, R., Ito, T. & Taguchi, T. Effect of alkyl chain length on the interfacial strength of surgical sealants composed of hydrophobically-modified Alaska-pollock-derived gelatins and poly(ethylene)glycol-based four-armed crosslinker. *Colloids Surfaces B Biointerfaces* **146**, 212–220 (2016).
191. Mizuta, R. & Taguchi, T. Enhanced Sealing by Hydrophobic Modification of Alaska Pollock-Derived Gelatin-Based Surgical Sealants for the Treatment of Pulmonary Air Leaks. *Macromol. Biosci.* **17**, 1600349 (2017).
192. Staros, J. V., Wright, R. W. & Swingle, D. M. Enhancement by N-hydroxysulfosuccinimide of water-soluble carbodiimide-mediated coupling reactions. *Anal. Biochem.* **156**, 220–222 (1986).
193. Lei, Q. P. *et al.* Kinetic studies on the rate of hydrolysis of N-ethyl-N'-(dimethylaminopropyl)carbodiimide in aqueous solutions using mass spectrometry and capillary electrophoresis. *Anal. Biochem.* **310**, 122–124 (2002).
194. Mizuno, Y. & Taguchi, T. Anti-Inflammatory and Tissue Adhesion Properties of an α-Linolenic Acid-Modified Gelatin-Based In Situ Hydrogel. *ACS Appl. Bio Mater.* **3**, 6204–6213 (2020).
195. ASTM, F.-04(2015). Standard Test Method for Burst Strength of Surgical Sealants. (2015) doi:10.1520/F2392-04R15.
196. Stämpfli, R., Brühwiler, P., Mourad, S., Verdejo, R. & Shaffer, M. Development and characterisation of carbon nanotube-reinforced polyurethane foams. *EMPA Act.* **26**, 51 (2007).
197. Erdinest, N., Shmueli, O., Grossman, Y., Ovadia, H. & Solomon, A. Anti-Inflammatory Effects of Alpha Linolenic Acid on Human Corneal Epithelial Cells. *Investig. Ophthalmol. Vis. Sci.* **53**, 4396–4406 (2012).
198. Pound, E. M., Kang, J. X. & Leaf, A. Partitioning of polyunsaturated fatty acids, which

prevent cardiac arrhythmias, into phospholipid cell membranes. *J. Lipid Res.* **42**, 346–351 (2001).

199. Wedgwood, J., Freemont, A. J. & Tirelli, N. Rheological and turbidity study of fibrin hydrogels. *Macromol. Symp.* **334**, 117–125 (2013).
200. Tamm, A. *et al.* Hydrophobic domains affect the collagen-binding specificity and surface polymerization as well as the virulence potential of the YadA protein of Yersinia enterocolitica. *Mol. Microbiol.* **10**, 995–1011 (1993).
201. Mancia, G. *et al.* 2007 Guidelines for the Management of Arterial Hypertension: The Task Force for the Management of Arterial Hypertension of the European Society of Hypertension (ESH) and of the European Society of Cardiology (ESC). *J. Hypertens.* **25**, 1105–1187 (2007).
202. Sun, L., Chang, W., Ma, Q. & Zhuang, Y. Purification of antioxidant peptides by high resolution mass spectrometry from simulated gastrointestinal digestion hydrolysates of Alaska pollock (Theragra chalcogramma) skin collagen. *Mar. Drugs* **14**, 1–14 (2016).
203. Savva, A. & Roger, T. Targeting Toll-like receptors: Promising therapeutic strategies for the management of sepsis-associated pathology and infectious diseases. *Front. Immunol.* **4**, 387 (2013).
204. Xu, Y. *et al.* Toll-like Receptor 4 Is a Sensor for Autophagy Associated with Innate Immunity. *Immunity* **27**, 135–144 (2007).
205. Kim, E. J., Lee, M. Y. & Jeon, Y. J. Silymarin inhibits morphological changes in LPS-stimulated macrophages by blocking NF-κB pathway. *Korean J. Physiol. Pharmacol.* **19**, 211–218 (2015).

Research Achievements

List of Publications

Journal Articles

1. **Mizuno, Y.**, Watanabe, S. & Taguchi, T. Tissue-sealing and anti-adhesion properties of an *in situ* hydrogel of hydrophobically-modified Alaska pollock-derived gelatin. *Int. J. Biol. Macromol.* **163**, 2365–2373 (2020).
2. **Mizuno, Y.** & Taguchi, T. A hydrophobic gelatin fiber sheet promotes secretion of endogenous vascular endothelial growth factor and stimulates angiogenesis. *RSC Adv.* **10**, 24800–24807 (2020).
3. **Mizuno, Y.** & Taguchi, T. Self-assembled dodecyl group-modified gelatin microparticle-based hydrogels with angiogenic properties. *NPG Asia Mater.* **12**, 48 (2020).
4. **Mizuno, Y.** & Taguchi, T. Anti-Inflammatory and Tissue Adhesion Properties of an α-Linolenic Acid-Modified Gelatin-Based In Situ Hydrogel. *ACS Appl. Bio Mater.* **3**, 6204–6213 (2020).
5. **Mizuno, Y.** & Taguchi, T. Growth factor-free, angiogenic hydrogel based on hydrophobically modified Alaska pollock gelatin. *J. Tissue Eng. Regen. Med.* **13**, 2291–2299 (2019).
6. **Mizuno, Y.** & Taguchi, T. Promotion of Cell Migration into a Hydrophobically modified Alaska Pollock Gelatin-Based Hydrogel. *Macromol. Biosci.* **19**, 1900083 (2019).
7. **Mizuno, Y.**, Mizuta, R., Hashizume, M. & Taguchi, T. Enhanced sealing strength of a hydrophobically-modified Alaska pollock gelatin-based sealant. *Biomater. Sci.* **5**, 982–989 (2017).
8. Ichimaru, H., **Mizuno, Y.**, Chen, X., Nishiguchi, A., Taguchi, T. Prevention of pulmonary air leaks using a biodegradable tissue-adhesive fiber sheet based on Alaska pollock gelatin modified with decanyl groups. *Biomat. Sci.*, **9**, 861-873 (2021).
9. Mizuta, R., **Mizuno, Y.**, Chen, X., Kurihara, Y. & Taguchi, T. Evaluation of an octyl group-modified Alaska pollock gelatin-based surgical sealant for prevention of postoperative adhesion. *Acta Biomater.,* **121**, 328–338 (2021).
10. Masuda, S., Suzuki, T., Shibata, S., Abe, Y., Chen, X., **Mizuno, Y.**, Nishiguchi, A., Kimura, H., Matsumura, N., Iwamoto, T., Taguchi, T., Matsumoto, M. & Nakamura, M. A novel Alaska pollock gelatin sealant shows higher bonding strength and equal recovery of the resected nerve compared to the fibrin sealant in a cadaveric model and a rat model. *Plast. Reconstr. Surg.*, accepted. (2020).

Other Articles

1. **水野 陽介**、田口 哲志,「生体接着材料研究の最前線~湿潤環境で作用する生体接着材料開発の現状と将来展望~」,『Materials Stage 2020 年 1 月号』, 技術情報協会, 第 19 巻 第 10 号, 2020 年
2. **水野 陽介**、田口 哲志,「生体組織接着剤の化学 糸で縫わない臓器・組織の術部閉鎖に 向けて」,『現代化学 2019 年 12 月号』, 東京化学同人, No.585, 2019 年
3. **水野 陽介**、田口 哲志「湿潤臓器・組織表面へ接着する生体吸収性接着剤の設計と機能」,『生体吸収性材料の開発と安全性評価』,技術情報協会, 第 5 章 2 節, 2017 年

List of Awards

1. **水野 陽介** “学長表彰（内定）” 筑波大学 2021 年
2. **水野 陽介** “研究奨励賞”, つくば医工連携フォーラム 2020, 2020 年
3. **水野 陽介** “優秀研究ポスター賞”, 第 41 回 日本バイオマテリアル学会大会, 2019 年
4. **水野 陽介** “優秀賞”, 第三十四回高分子学会関東支部 茨城地区若手の会交流会, 2019 年
5. **水野 陽介** “萌芽研究ポスターセッション優秀賞”, 第 57 回日本人工臓器学会大会, 2019 年
6. **水野 陽介** “数理物質科学研究科長賞” 筑波大学 2018 年
7. **水野 陽介** “萌芽研究ポスターセッション優秀賞”, 第 55 回日本人工臓器学会大会, 2017 年
8. **水野 陽介** “優秀賞”, 高分子学会関東支部 茨城地区若手の会交流会, 2017 年
9. **水野 陽介** “優秀研究ポスター賞”, 第 39 回 日本バイオマテリアル学会大会, 2017 年
10. **水野 陽介** “研究奨励賞” Tsukuba Global Science Week 2016, 2016 年
11. **Y. Mizuno** “NIMS Student Seminar Excellent Presentation Award”, NIMS Student seminar, 2016 年